Award Number: W81XWH-10-1-0736

TITLE: Objective Methods to Test Visual Dysfunction in the Presence of Cognitive Impairment

PRINCIPAL INVESTIGATOR: Randy Kardon M.D. Ph.D., Pieter Poolman
Ph.D.

CONTRACTING ORGANIZATION: University of Iowa
Iowa City IA 52242-1316

REPORT DATE: December 2015

TYPE OF REPORT: FINAL

PREPARED FOR: U.S. Army Medical Research and Materiel Command
Fort Detrick, Maryland 21702-5012

DISTRIBUTION STATEMENT:

x Approved for public release; distribution unlimited

REPORT DOCUMENTATION PAGE

Form Approved
OMB No. 0704-0188

1. REPORT DATE *(DD-MM-YYYY)* December 2015	**2. REPORT TYPE** Final	**3. DATES COVERED** *(From - To)* Sept 15, 2010 to Sept 14, 2015
4. **Objective Methods to Test Visual Dysfunction in the Presence of Cognitive Impairment**		**5a. CONTRACT NUMBER** W81XWH-10-1-0736 **5b. GRANT NUMBER** #11125001 **5c. PROGRAM ELEMENT NUMBER**
6. AUTHOR(S) Randy Kardon M.D. Ph.D., Pieter Poolman Ph.D. email: randy-kardon@uiowa.edu		**5d. PROJECT NUMBER** **5e. TASK NUMBER** **5f. WORK UNIT NUMBER**
7. PERFORMING ORGANIZATION NAME(S) AND ADDRESS University of Iowa 105 Jessup Hall Iowa City, IA 52242-1316		**8. PERFORMING ORGANIZATION REPORT NUMBER**
9. SPONSORING / MONITORING AGENCY NAME(S) AND ADDRESS(ES) U.S. Army Medical Research and Materiel Command Fort Detrick, Maryland 21702-5012		**10. SPONSOR/MONITOR'S ACRONYM(S)** **11. SPONSOR/MONITOR'S REPORT NUMBER(S)**

12. DISTRIBUTION / AVAILABILITY STATEMENT
Approved for Public Release; distribution unlimited

13. SUPPLEMENTARY NOTES

14. ABSTRACT (200 Words) Summary of most significant finding (s)
Purpose: To develop and validate objective tests to diagnose vision deficits in patients with cognitive impairment and ensure effective monitoring of their treatment.
Scope: Objective methods to monitor visual function include 1) the pupil light reflex (PLR), 2) light evoked potentials (VEP) from the brain and from the eye and 3) purposeful eye movements to track targets that are resolved.
Major Findings: Three major objective tests of vision were successfully developed and optimized to detect disease. These were 1) the pupil light reflex (either comparing the two eyes or independently evaluating each eye separately for retina or optic nerve damage, 2) eye movement based analysis of target acquisition, fixation, and eccentric viewing as a means of detecting central visual field damage and central nervous system disturbances (i.e. multiple sclerosis, traumatic brain injury, dementia), and 3) wireless recording of evoked visual potentials for assessing regional damage to different locations of the visual field within a very short testing time (under 60 seconds).
Significance: Objective tests of vision will greatly improve eye care by providing faster, lower cost testing that can be performed in remote settings and will provide a new tool for assessing innovative treatments being developed to save or restore vision.

15. SUBJECT TERMS
Traumatic brain injury, cognitive dysfunction, pupil light reflex, eye movements, evoked potentials, visual function

16. SECURITY CLASSIFICATION OF:			**17. LIMITATION OF ABSTRACT**	**18. NUMBER OF PAGES**	**19a. NAME OF RESPONSIBLE PERSON**
a. REPORT U	**b. ABSTRACT** U	**c. THIS PAGE** U	UU	91	USAMRMC **19b. TELEPHONE NUMBER** *(include area code)*

Standard Form 298 (Rev. 8-98)
Prescribed by ANSI Std. Z39.18

TABLE OF CONTENTS

INTRODUCTION

Our project's research goal focused on providing objective and military relevant means for diagnosing and localizing the site of visual dysfunction in cognitively impaired patients. The successful attainment of this goal hinged on the development of a suite of objective tests designed to free the TBI patients from the cognitive demands placed on them during standard visual testing. As a necessary step for testing of cognitively impaired patients with suspected visual dysfunction, we optimized various objective tests of visual function: a) pupil contractions to light stimuli, b) evoked potentials elicited from the visual cortex in response to visual stimuli in the central and peripheral visual field locations, and c) eye position correlated with moving visual targets varying in spatial properties as a means of verifying that the patient was able to perceive the targets. Next, we validated these objective tests against gold standard behavioral tests of visual field sensitivity in cognitively intact participants who were capable of performing these tests accurately. For the validation phase, participants were selected who have either normal visual function or who have known dysfunction at different sites along their visual pathway. Using this strategy, normal eyes and eyes with well-defined damage to the retina, optic nerve, visual radiations or visual cortex were used to study the sensitivity and specificity of the different modalities of objective tests that were evaluated during this project. These validated, objective tests can now be rapidly implemented for use in cognitively impaired patients, specifically those who have suffered traumatic brain injury.

BODY

The following personnel received pay from the project:

- Randy Kardon, MD PhD
- Pieter Poolman, PhD
- Robert Mallery, MD
- Johannes Ledolter, PhD
- Cole Starkey
- Anna Ketcham

Injury to the visual system may be difficult to detect in patients with cognitive impairment who cannot reliably perform standard tests of vision, such as perimetry (visual field testing). This project focused on the development, optimization, and validation of a battery of objective tests based on neurological reflexes to enable accurate assessment of vision over the spectrum of a patient's condition from unconsciousness to awake, but cognitively impaired, both at the time of injury and in the follow-up period of evaluation and treatment. Patients with cognitive impairment resulting from traumatic brain injury (TBI) and other disorders such as psychiatric illness and dementia will benefit from new approaches to objectively assess vision.

For the purposes of the project, we hypothesized that natural reflexes of the brain, such as the pupil light reflex, light evoked potentials from the eye and brain, and the ability of a patient's eyes to track a visual target are powerful, underutilized approaches for diagnosing and monitoring dysfunction at specific locations along the visual pathway from the eye to the brain. To enable testing of cognitively impaired patients in the future, we developed and optimized novel objective tests of visual function and validated them against standard behavioral tests of visual field sensitivity performed by cognitively intact patients. Optimization of signal to noise was accomplished through informed selection of visual stimuli and innovative analysis approaches. Our development effort was guided by the need to provide new low cost and ubiquitous solutions for objective assessment of visual function in patients over a wide range of cognition in both telemedicine and clinical settings.

We investigated three objective modalities of visual testing: a) pupil contractions to focal, regional, and diffuse light stimuli, b) evoked potentials to focal and diffuse light elicited from the retina and visual cortex, and c) eye position correlated with visual targets varying in spatial properties. Normal eyes and eyes with well-defined damage to the retina, optic nerve, or visual cortex were used to compare the different modalities of testing to standard visual field testing. During the course of the project, we integrated novel product-ready hardware solutions to implement several test platforms capable of recording and analyzing multiple modalities of physiological measurements. We also optimized the hardware systems and vision testing protocols to reduce testing time, maximize the signal/noise, and minimize cognitive demands placed on the patient, as described in this report.

Task 1. Implementation of novel product-ready hardware solutions that allow objective testing of the visual system

1a. Hand-held portable pupillometer (Neuroptics, Inc., Irvine, CA)

At the start of the project, we acquired a hand-held pupillometer from Neuroptics, Inc. (see Figure 1). Based on our evaluation of the hardware and software, we made recommendations to the company to modify the pupillometer so that it could provide chromatic (red, blue and white) stimuli, since our pilot data for the grant submission and published data at the time indicated that we were able to isolate the rod, cone and intrinsic melanopsin retinal ganglion cell response using red and blue stimuli at low and high intensities under conditions of light and dark adaptation. This enables one to determine of vision loss is due to inner retina/optic nerve causes or to outer retina (rod and cone) loss, and would be important for localizing the site of damage.

Figure 1. Hand-held portable pupillometer (Neuroptics, Inc., Irvine, CA), which is able to deliver white light stimuli and record pupil movements from one eye at a time in response to light stimuli for diagnosing retinal and optic nerve disorders.

Based on our recommendations to the company, the hand-held pupillometer was replaced by the company with the DP-2000 system, a small desktop unit from Neuroptics, Inc. that is binocular, delivers stimuli over a wide range of intensities to each eye (white, red, blue or green LED source), and collects pupil responses from both eyes simultaneously (see Figure 2). We continued to use the desktop system for the remainder of the project. This system allows afferent visual abnormalities to be differentiated from efferent disorders of the output pupil pathway, and can be detached for use at bedside exam. This unit also delivers chromatic light stimuli (blue, red, green or white) so that rod, cone and intrinsic melanopsin retinal ganglion cell activation can be derived for differentiating visual loss from photoreceptor disease from that of optic nerve/anterior visual pathway diseases. We redesigned our testing protocols to take advantage of this incorporated feature and to reduce testing time to a minimum.

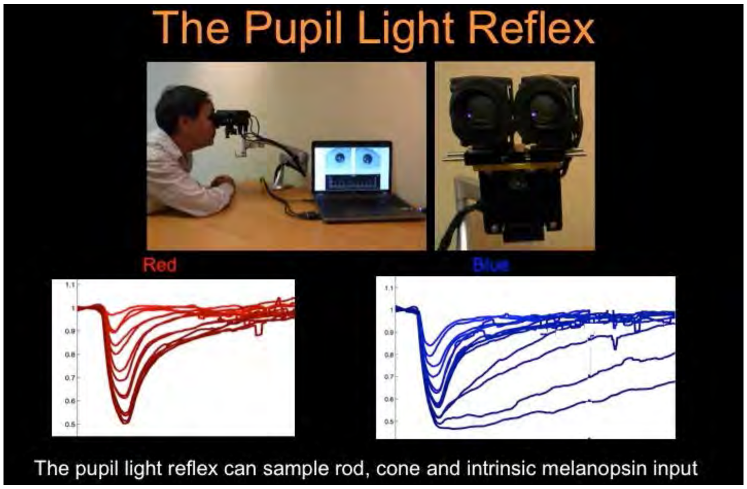

Figure 2. Results from binocular chromatic (red and blue light stimuli) tests show rod, cone and melanopsin mediated pupil responses. Top is the Neuroptics, Inc. (Irvine, CA) DP-2000 desktop unit that can record both pupils and stimulate either the right eye, left eye or both eyes with red, blue, green or white light. At bottom are a series of pupil light reflex waveforms with increasing intensity of red light for cone responses (red tracings) and blue light responses (blue tracings) for rod mediated responses at low intensity and sustained pupil contractions from melanopsin mediated responses to blue light at the highest intensities.

We continued to collaborate with Neuroptics, Inc. to develop fully portable, battery powered and self contained pupillometers that could be used in a variety of environments. In response to our request to develop a more portable unit, Neuroptics, Inc. developed a binocular pupillometer that was hand held. Another prototype design was even smaller, lighter and could be worn by a patient similar to a pair of virtual reality glasses (see Figure 3).

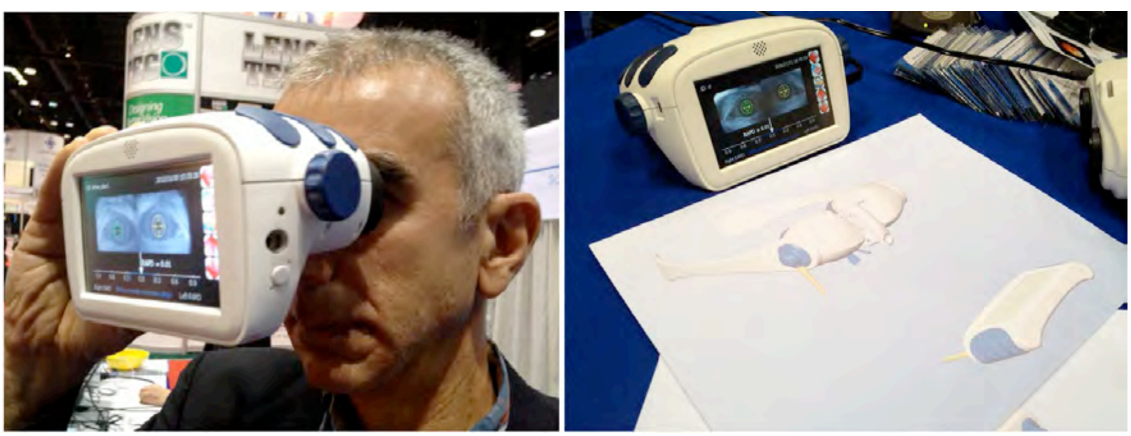

Figure 3. <u>Left</u>: Portable hand-held binocular pupillometer prototype instrument developed by Neuroptics, Inc., Irvine, CA, based on our suggestions. This pupillometer can deliver red, blue, green or white light stimuli to either eye and record both pupil responses simultaneously to assess both afferent and efferent pupil disorders. <u>Right</u>: The drawings show another prototype conception, which would be a 9-oz. lightweight pair of glasses. It would contain miniature infrared video cameras and the LED stimulus source for red, blue, green, and white stimuli that could be comfortably worn by the subject during testing. The rectangular module shown below it would be worn around the patient's neck and contained the LCD monitor screen for viewing the pupils during the test as well as the self contained battery operated processor and data storage device.

Recently, Neuroptics, Inc. developed a binocular portable and desktop pupillometer for commercial sale and distribution ("RAPiDo"). Its unique design allows it to reside on a desktop for outpatient testing or after removal from its support, it can be hand held to test inpatients, including those in the supine, lying flat position (see Figure 4). This will be particularly useful for pupil testing of

patients near battlefield arenas at triage points. Our contribution to this commercial device has been the development of rapid pupil testing protocols for assessing the relative afferent pupil defect (log unit RAPD) that only takes 30 seconds of testing. A detailed description of this continuous RAPD test protocol (log unit RAPD as a function of stimulus light intensity) is provided elsewhere in the report. Neuroptics Inc. is very interested in licensing the test protocol from us (the University of Iowa Research Foundation), and steps are underway to include it as part of their new RAPiDo device. In addition, we developed and tested a novel, short testing protocols to assess the status of the retina and optic nerve in each eye independent of the other eye, using red and blue light stimuli (as discussed later in the report). This will allow a quantification of retina and optic nerve function in patients that have bilateral damage.

Figure 4. Prototype binocular portable and desktop pupillometer (Neuroptics Inc, Irvine, CA) for fast, efficient clinical testing of the pupil light reflex. The pupillometer is battery powered and transmits video and pupil information by blue tooth to the portable processor or also to a nearby computer. The optical head can be easily removed and mounted on a handle for testing of patients that cannot sit up at a desktop area and for inpatients in a hospital bed.

1b. TrueField Analyzer visual field testing device (Seeing Machines Limited)

The TrueField Analyzer, developed by Dr. Ted Maddess at Canberra University in Australia for Seeming Machines Limited, was not released for patient testing during the duration of the project. The company was unable to provide us with a date when the instrument would be available for use and purchase. To further evaluate the multifocal pupil perimetry device and to further understand the nature of the problems that they were experiencing with the instrument at the time, the PI traveled to Dr. Maddess' laboratory in September 2011. The main problem was that the LCD light source that they were using to provide the focal light stimuli has proven to be unstable over time and they were developing an automated light calibration routine that would adjust the brightness of the stimulus as it changes over time to ensure that the light intensity delivered would be what is specified. In addition, they were still working out which wavelength of light, stimulus size, and timing of stimulus provide the optimal ability to differentiate diseased from normal eyes. Because

of the uncertainty surrounding the deliverability of the TrueField Analyzer, we developed our owns flexible visual stimulation software platform (see 1d) below) that enabled measurement of pupil responses to focal stimuli in different locations of the visual field.

1c. “Dry electrode” wireless EEG system (Sigmed, Inc.)

We received our dry-electrode wireless system during the last half of Year 2 (see Figure 5). At our request, Sigmed redesigned their current 16-channel EEG system to accommodate our requirements to measure from 8 channels placed around the eyes to measure EOG, orbicularis-corrugator EMG, ERG, and another 8 channels placed over occipital-parietal-temporal scalp locations to measure evoked potentials from visual cortex. The Sigmed system, called Mindo, has the advantage of being wireless, no skin preparation or gel is needed at the point of contact with skin, there is a large dynamic range of potential that can be recorded (24 bits, +/- 2.5 volts). Based on personal communication with Sigmed and researchers at the Army Research Laboratories, ongoing development of the Mindo system is focused on better electrode materials and designs, as well as reducing data packet loss resulting from the use of Bluetooth as the wireless communication protocol between the headset and attached computerized storage device.

Figure 5. Wireless “dry” electrodes for facial/brow/lower eyelid muscle EMG and ERG recording which are squares and are sponge-like (left). Rounded, spring-loaded dull prong electrodes for the scalp are shown to the upper right, that can penetrate around hair follicles for recording EEG/visual evoked potentials.

During Year 3, we designed a comfortable head band and face appliance to mount the wireless electrodes so that they can be easily worn and make contact with the skin on the scalp and face without the need for any skin preparation or solutions. As a starting point, we used the head gear design from Emotiv who had manufactured a head mount with EEG electrodes for video gaming. The design of the headset included mounts to position the dry electrodes at scalp locations over the visual area of the brain (occipital cortex) for wireless recording of the visual evoked potentials (VEP) for regional visual stimuli, as well as on the skin overlying the orbicularis and procerus muscles for recording EMG responses to light (our other DOD grant). This work has been done in conjunction with Mark Ginsberg, owner of Ginsberg Jewelry in Iowa City and Bounnak Thammavong, his design assistant, to develop a molding which can be adjusted to change the tension between the electrodes and the skin and which can be rendered using a 3D printer. The 3D printing specifications included the use of a flexible and soft polymer resin that can be autoclaved for sterilization. An example of the CAD design of the prototype is shown in Figure 6.

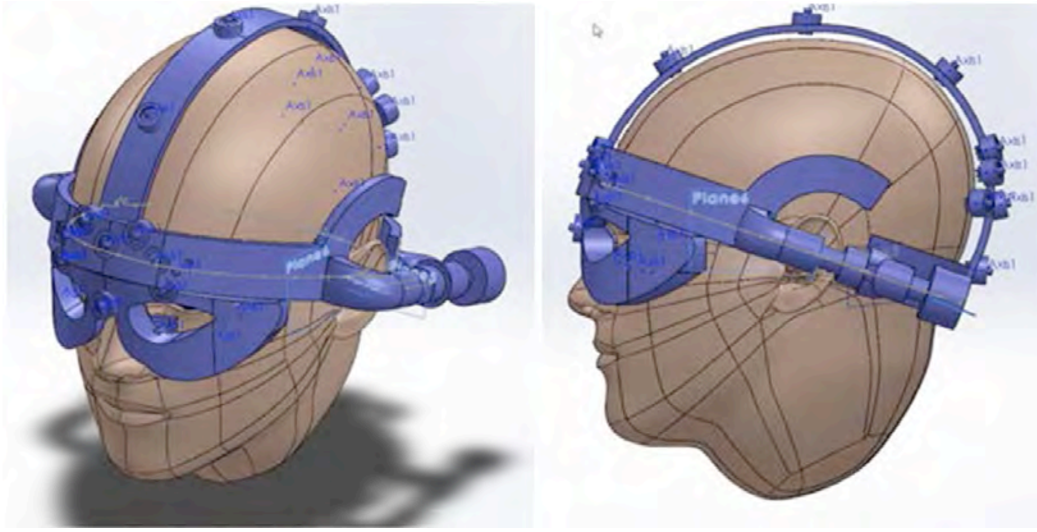
Figure 6. 3D CAD rendering of head/face mount for VEP and EMG wireless electrodes.

1d. Multi-camera eye movement monitor (Smart Eye AB)

During Year 1, we evaluated the measuring accuracy and integration capabilities of the 4-vantage point cameras of the Smart Eye remote head/eye tracker. In order to maximize the unobtrusiveness of the system, as well as patient comfort, the cameras and infrared illuminators are located six feet away from the patient (see Figure 7), which poses a major challenge for any existing eye tracking system to obtain sufficient resolution and accuracy of eye tracking. From initial results, the infrared illumination was found to be insufficient at six feet, leading to faint retinal reflections, and hampering tracking performance. To increase the illumination levels, we purchased brighter infrared illuminators from Smart Eye, modified the system, and subsequently verified the improved illumination levels and sufficient tracking. In order to expand interoperability with stimulus presentation and other physiological measurement systems, we modified and upgraded the Smart Eye system to accept transistor-transistor-logic TTL signals. The ability to log TTL signals together with the eye tracking data, enabled us to synchronize data across multiple modalities, such as evoked potentials recorded simultaneously with the eye tracking.


Figure 7. Demonstration of Smart Eye head and eye movement tracking system fitted to a Samsung LN52B750 52" TV, located six feet away from the patient.

As part of this subtask, we developed and tested an integrated multi-modal experimental control and analysis platform. With this system, we can control, import, synchronize, and integrate data collected from our Biopac system (for EKG, EOG, EMG, GSR, etc.), Arrington head-mounted eye and pupil tracker, Smart Eye system, Diagnosys stimulus presentation system, Mindo wireless EEG system, as well as the OptoViewer stimulus presentation system especially developed for this project. We also developed numerous Matlab signal processing scripts which link directly to the analysis software to retrieve and pass back data in real time, as well as to visualize results, as discussed in more detail elsewhere in the report. Our analysis architecture allows us to monitor different diagnostic metrics simultaneously in case more than one stimulus type are presented at the same time, e.g., we can compute pupil responses to color patches flickering at different frequencies, relating the measurements to the patch being fixated from eye tracking data, while also calculating VEP amplitudes from the EEG data.

Pupil light reflex test bed

A significant effort was spent to consolidate the pupil light reflex test on the multi-modal test platform into a single workflow of operational steps. The workflow architecture allows us to launch, pause, and monitor the stimulus presentation and data collection processes, as well as data analysis – both real time (on-the-fly), and in post-processing (after-action review) mode – from a set of interacting Matlab graphical user interfaces (GUIs). The real-time (on-the-fly) analysis provides us with the ability to decide whether to delay or repeat a stimulus based on the subject's responses. The workflow architecture is specifically designed to be easily extendible to the other modalities of tests, physiological responses, and analysis requirements.

Apart from selecting, launching and controlling experiments, the user can also set parameters and select rules to govern when the next stimulus is to be presented to the subject. For example, in the case of pupil light reflex recordings, the Experiment Manager can be instructed to use time duration after a stimulus and/or recent pupil size to automatically advance to the next stimulus. For example, with this flexible system, the user can specify to give the next light stimulus when the pupil recovers to a specified diameter. The user is also allowed to interrupt (pause) this automatic process, or to force the presentation of any stimulus if needed. In the Pupil Analysis GUI, the user can select and set numerous parameters to control the analysis and visualization of stimulus-response metrics. The analysis is agnostic as to whether data are streaming to the GUI (real-time mode) or are loaded from a static data source of previously recorded data from video (post-processing mode). Both GUIs are also agnostic as to the origin of the pupil and eye tracking data, and can deal with data from both our Arrington and Smart Eye eye movement/pupil movement systems. The same is true for EEG and EMG data, which can originate from either the Biopac or the Mindo dry electrode system. Screenshots of the Experiment Manager GUI (see Figure 8) and Pupil Analysis GUI (see Figure 9) are shown below.

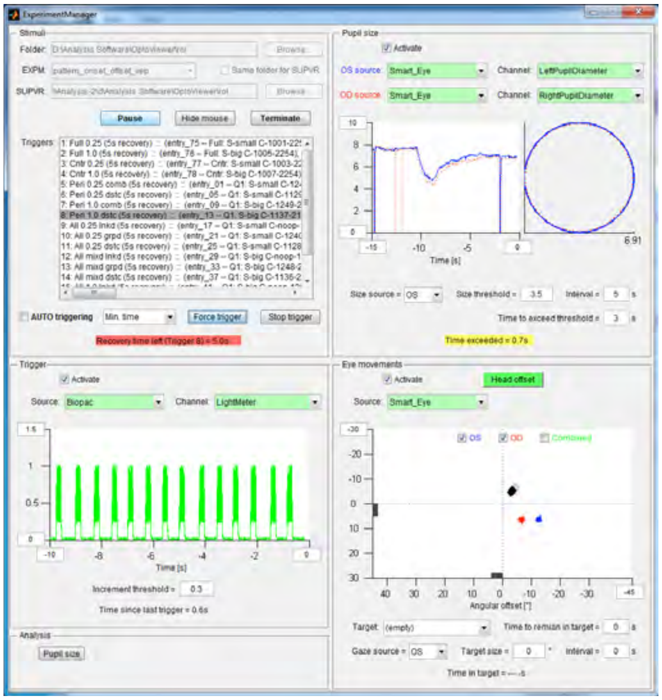

Figure 8. Layout of the Experiment Manager GUI. In the upper right portion of the window is the real-time pupil data display from the right and left eye recording in relation to a light stimulus. The red and blue circles are a graphical display of the instantaneous right and left pupil size, superimposed, which change in real time as the data is streaming onto the display. The Pupil Analysis GUI can be launched at any time with the "Pupil size" button in the "Analysis" panel (lower left portion of window). The lower right portion of window is used to display real-time head and eye tracking measurements, as well as a user-specified fixation target. The most recent few seconds of the orientation of the left, right, and/or combined gaze vectors, as well as the orientation of the current stimulus (black diamond) are depicted in the graph to assist the experimenter in visualizing the subject's viewing behavior with respect to the stimulus. Furthermore, based on whether the subject is fixating a pre-specified target, the experimenter can control the onset of stimuli, either manually, or in an automated way based on a set of rules.

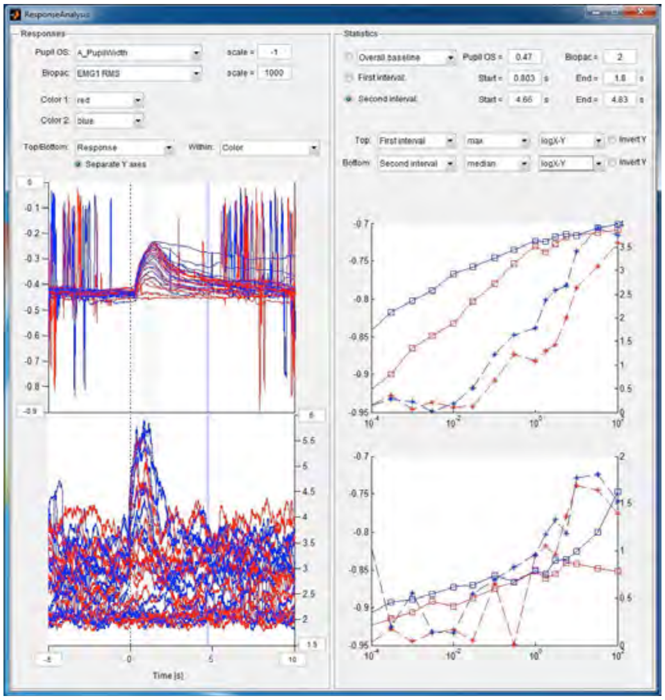

Figure 9. Layout of the Response Analysis GUI. The GUI can be used to analyze responses from either a single data modality or from two different data modalities. For the example shown in the figure, the GUI is used for analyzing pupil light reflex and procerus/corrugator EMG data. This interface allows the user to define how the raw signal (in this case left pupil size time series as a function of light intensity, shown in upper left panel, and the EMG time series, shown in the lower left panel) should be analyzed and displayed in real time or after the experiment is over, playing back the data stream. The pupil movements and EMG responses are respectively superimposed for red and blue light stimuli of increasing intensity. For example, shown in the upper right panel is the maximum change in pupil size (solid lines) and EMG responses (dashed lines) recorded as a function of log light intensity of light stimuli. As the light intensity increases, so does the amplitude of the pupil movement and EMG response. In real time, points would appear on the graph as the data is collected to allow the user to evaluate the results in real time and repeat any portion of the experiment while the subject is still present. The lower right panel shows the sustained pupil contraction and EMG responses present at about 5 seconds after the one second stimulus onset. This shows that for the blue light stimuli at brighter intensities, the pupil response is more sustained (blue squares and solid line) compared to the responses to red light stimuli (red squares and solid line).

<u>Development of optical-visual stimuli</u>

With the help of our software provider, we developed OptoViewer – a system designed to present a wide variety of visual stimuli. The program allows stimuli to be easily arranged into multiple experiment sequences. It is also possible to trigger the onset of stimuli from 3rd party software packages, like Matlab, which allows us to delay the onset of stimuli based on any custom criteria. For example, the onset of a wide-field chromatic stimulus – used to monitor a subject's pupil light reflex – can be delayed until the subject's pupils have dilated to a specified level. Or, in terms of eye movement tests, a vanishing optotype target can be delayed from starting to move across the monitor until the subject has fixated it for a specified minimum time interval to ensure that the subject is in fact aware of the presence of the target. The experimenter can also control what type of image stabilization should be applied to the stimulus canvas based on the subject's head and/or eye location and orientation. Having access to a wide variety of customizable stimuli was an important aspect of the study design because they could be used to elicit responses that are objective measures of visual function. These responses include 1) pupil responses to the visual stimuli in the

center and periphery of the visual field, 2) eye movements in response to tracking a visual target, and 3) evoked responses from the eye and brain in response to the visual stimuli.

The implementation of the software architecture allows us to control the graphics hardware on a low-level software to hardware control, to maximize timing precision of the stimuli, while at the same time it offers cross-platform compatibility to run on desktop, laptop, and handheld devices. Visual stimuli include static or moving visual stimuli, which can be filled with solid colors, static or moving gratings of various configurations (verniers, checkerboard, stripes etc.), images, and vanishing optotypes. The colors and transparency of these stimuli can be independently varied over time. Based on algorithm to adjust pixel colors in real time, we have generalized the vanishing optotype design to enable us to display these optotypes on any background. The stimulus presentation system includes all the stimulus types required for the purposes of this project in order to study the pupil light reflex with colored light, acuity and eye movements with vanishing optotypes and vernier patterns, opto-kinetic reflexes with moving gratings, and visually evoked potentials (VEPs) with flickering color patches. We have included various methods to synchronize the physiological data with stimulus onset times. These methods include sending TTL-type signals via the parallel and/or serial ports on the stimulus PC to the data recorder (Biopac or Smart Eye hardware). We have also developed and tested an analog light meter that is facing the stimulus monitor. This light meter allows us to monitor the actual sequencing of the presented stimuli very accurately, and helps us record and monitor screen refreshes on modern LCD monitors. Knowing the precise stimulus history during the testing allows us to more accurately assess the frequency dependent Fourier analysis of evoked responses.

1) Vanishing optotypes

With the expert help of Dr. Lars Frisen, University of Gothenburg, Sweden, we have developed examples of computerized vanishing optotype stimuli. Vanishing optotypes are uniquely suited for someone with limited cognition because they are either visible against a diffuse background or they will blend into the background and "vanish" if the person cannot resolve their border (see Figure 10). Changing the thickness of the lines used to define their shape varies the acuity of each target, without having to change the target size.

Figure 10. Example of vanishing optotype rings that change in spatial frequency (left to right) and contrast (top to bottom).

We have evaluated the trade-off amongst line thickness, line orientation, and screen resolution. Line thickness is constrained by the monitor resolution (thinnest component of a horizontal or vertical line segment, and cannot be less than a single pixel wide). In the case of slanted line segments, it is necessary to apply anti-aliasing filtering to suppress display artifacts, which reduces the high-frequency content of the vanishing optotype target, and complicates the interpretation of the displayed grayscale values versus the intended light levels. After reaching a certain lower limit in line thickness, we have found that it might be better to alter the grayscale values to obtain even lower contrast ratios which will allow us to reach the visual threshold for spatial frequency using wider (thicker) borders for the optotypes.

We also developed a software tool to quickly create vanishing optotypes from various pre-existing images of an object of interest. The process starts with turning the image of the object into a line drawing. The user then sets the line widths and contrast levels to define the appearance of the vanishing optotype. An example of a vanishing optotype from our collection is shown in Figure 11, which was made from a picture of an armed enemy soldier.

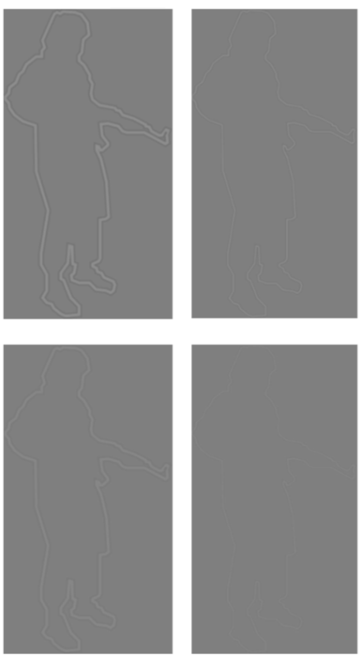

Figure 11. Vanishing optotypes of an armed person based on different line widths (left vs. right), and contrast levels (top vs. bottom). In the top section the original image is rendered into a thick lined optotype (left) and a thin lined optotype (right). In the bottom panel each of the images are rendered as a lower contrast line drawing with the features of the vanishing optotype. At this lower contrast the thinner lined drawing starts to disappear in the lower right panel.

2) Alternating checkerboard patterns for recording evoked potentials

During Year 1, we built a complete workflow for VEP testing, consisting of stimulus configuration, stimulus presentation, evoked potential recording, data synchronization, and analysis (see Figure 12). For stimuli, customizable alternating checkerboard patterns are generated by OptoViewer. The experimenter can manually trigger the onset of each checkerboard pattern when the patient is fixating on the fixation target based on data from the Smart Eye head and eye tracking system. An analog light meter mounted in the upper corner of the monitor is used to record the actual

presentation timing and luminance of the stimuli appearing on the patient display. Given that the Mindo dry electrode EEG system was not yet delivered to us at that time, VEP data was collected with a customized 4-channel wireless Biopac BioNomadix system (see Figure 13). Afterwards, the recorded data is analyzed in Matlab (see Figure 14).

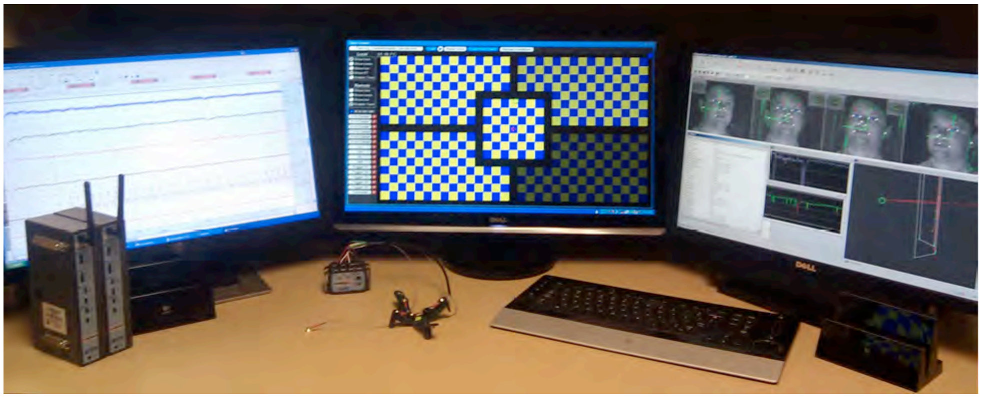

Figure 12. Experimenter's workstation to control stimulus sequencing with OptoViewer's supervisor screen (center display), as well as monitor the patient's EEG (left monitor) and head and eye movements in real time (right monitor).

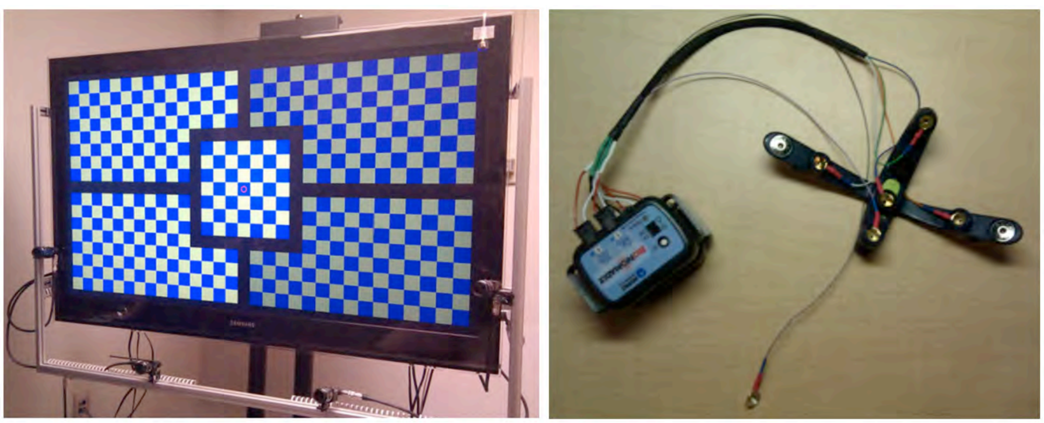

Figure 13. <u>Left</u>: Example of one type of VEP stimulus in OptoViewer on a Samsung TV. Sinusoidally alternating checkerboard patterns and a fixation target are presented on the subject monitor. Mounted on the monitor stand are 4 video cameras and infrared illuminators (Smart Eye System) for tracking the eyes and head in real time during the visual testing. An analog light meter is mounted to the upper right hand corner of the monitor and is directed at the monitor to transmit the light level in real time to the computer. In the stimulus shown, each box containing a checkerboard pattern in the center and peripheral visual field locations can be made to alternate at distinct frequencies independently for extracting visual field information from the VEP signals recorded. <u>Right</u>: Custom wireless Biopac BioNomadix 4-channel VEP system with a shared reference electrode (unipolar setup). The four electrodes are supported on a flexible cross that is applied to the scalp and the small box to the left is the wireless transmitter to relay the VEP signals continuously to the Biopac receiver/digitizer.

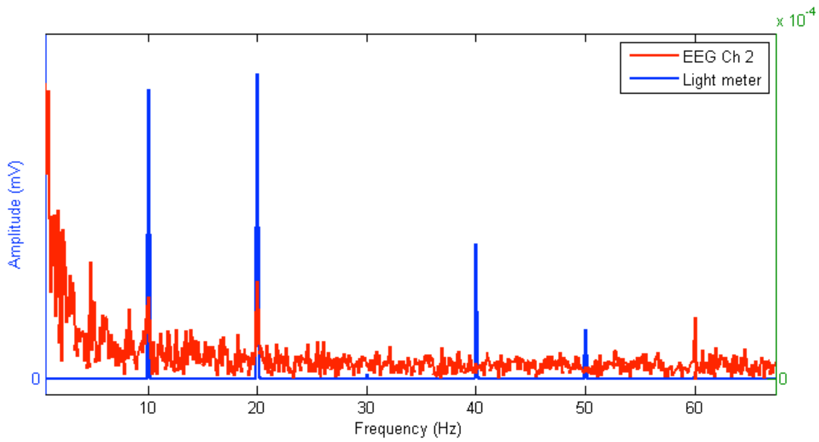

Figure 14. Expected spectrogram of VEP (red tracing) and light meter (blue peaks) signals for sinusoidally changing checkerboard stimulus of blue and yellow squares at 10 Hz (base frequency). Note that it is expected that the frequency analysis picks up a 10 Hz VEP response (yellow visual pattern to yellow and blue visual pattern to blue) and a 20 Hz VEP response from a state change (on-off signal due to yellow to black or blue to black) reflecting the potential to detect visual evoked responses using Fourier transform power analysis of temporal frequencies in the EEG recording. We can also extract phase (latency) information using this type of analysis.

During Year 2, we implemented a temporally modulated stimulus for the visually-evoked potential (VEP) portion of this project, with the objective to measure regional visual field responses from evoked responses elicited from the eye and brain. The advantage of using such a stimulus is that it allows us to interrogate the visual system's ability to conduct impulses in the central visual field, but also simultaneously in other locations in the peripheral vision within a very short time period of testing (less then a minute). This is accomplished by using a matrix stimulus paradigm that correlates responses with specific temporal frequencies of visual stimuli occurring independently in each region of the visual field being tested. The test can be potentially performed on multiple platforms, such as tablets and smartphones, which could be used to evaluate traumatic brain injury patients in the field.

To complement the existing frequency modulated checkerboard stimuli developed in Year 1, we also added a set of flash and pattern onset/offset stimuli based on the International Society for Clinical Electrophysiology of Vision (ISCEV) 2009 standard. For pattern onset/offset, the checkerboard pattern is abruptly exchanged with a diffuse gray background. Pattern onset duration is set at 200ms, as specified by the ISCEV standard. Onsets are separated by at least 400ms of diffuse background. This paradigm differs from our earlier VEP stimulus paradigm in an important way: for the frequency modulated stimuli, each stimulus location is assigned a different distinct temporal frequency to facilitate differentiation of the responses amongst the central and peripheral visual areas, while we rely on the exact stimulus onset times in case of the ISCEV-type stimuli to separate out the responses from the different visual areas, as explained later on. Two pattern element sizes – checks of 0.25° or 1° per side – can be used in a mix-and-match approach to populate the different stimulus locations based on the patient's acuity level (see Figure 15).

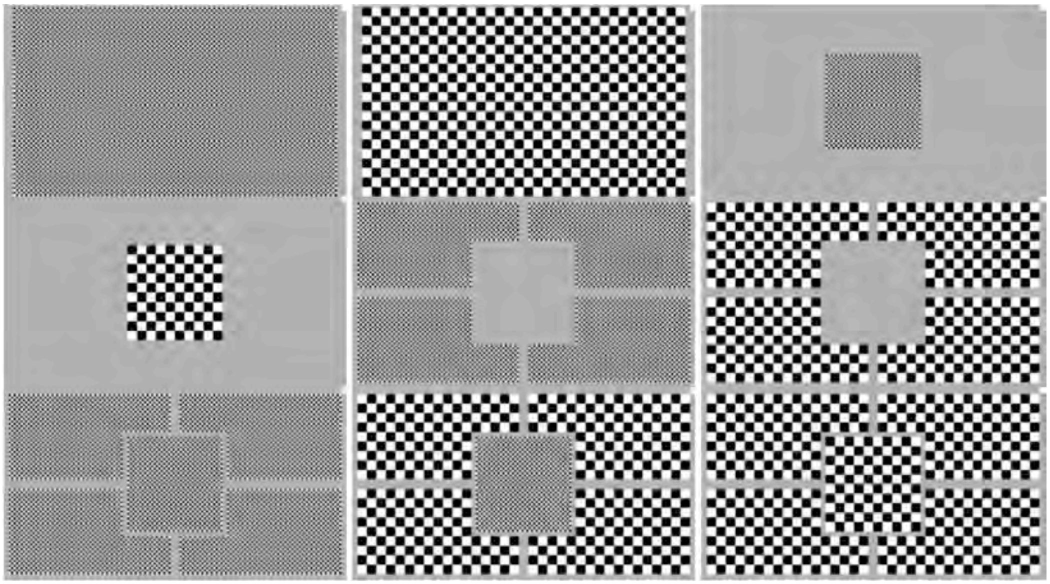

Figure 15. Examples of nine (9) different checkerboard layouts using 0.25° and 1° check sizes to create full--field, center-only, peripheral-only, and combined center-peripheral stimuli. A red circle is provided in the center of the screen to serve as a fixation target for the subject during the stimulation sequence.

Ideally, the mean luminance of the diffuse background and the checkerboard is set to be identical with no change of luminance during the transition from pattern to diffuse blank screen. This is difficult to achieve on a LCD type monitor as the gray-to-white time interval is inherently different from the gray-to-black time interval (similarly, white-to-gray and black-to-gray time intervals) giving rise to faint millisecond-long flashes every time the stimulus changes from a diffuse background to a checkerboard pattern and vice versa. Nonetheless, through the use of a diffuser, care is taken to ensure that the steady-state mean luminance of the diffuse background matches the steady-state mean luminance of the checkerboard pattern. It is important to note that the ISCEV standard is solely geared towards a single full-field stimulus, while it was our stated goal to develop and test a VEP paradigm that will enable us to interrogate multiple broad locations of a subject's field of view within a short time period, which will be especially useful when testing cognitively-impaired patients in future studies. Although multi-focal techniques exist, they are too fine-grained for our purposes, and take an enormous amount of time to allow for the presentation of enough stimulus repetitions for data analytic purposes.

1e. Literature study

We continually updated our information with recently published articles that were relevant to our proposed research as part of the literature study. The literature search for papers focused on objective testing of visual function revealed the following relevant publications:

Ciocler Froiman P, Dantas PE. Assessment of visual acuity in patients with dementia using teller acuity cards. Strabismus. 2013 Jun;21(2):93-7.

Wood JS, Firbank MJ, Mosimann UP, Watson R, Barber R, Blamire AM, O'Brien JT. Testing visual perception in dementia with Lewy bodies and Alzheimer disease. Am J Geriatr Psychiatry. 2013 Jun;21(6):501-8.

Gundogan FC, Tas A, Altun S, Oz O, Erdem U, Sobaci G. Color vision versus pattern visual evoked potentials in the assessment of subclinical optic pathway involvement in multiple sclerosis. Indian J Ophthalmol. 2013 Mar;61(3):100-3.

Bedell HE, Stevenson SB. Eye movement testing in clinical examination. Vision Res. 2013 Sep 20;90:32-7.

Dong W, Yan B, Johnson BP, Millist L, Davis S, Fielding J, White OB. Ischaemic stroke: the ocular motor system as a sensitive marker for motor and cognitive recovery. J Neurol Neurosurg Psychiatry. 2013 Mar;84(3):337-41.

Young B, Eggenberger E, Kaufman D. Current electrophysiology in ophthalmology: a review. Curr Opin Ophthalmol. 2012 Nov;23(6):497-505.

Tasks 2-4. In normal eyes, eyes with damage to the retina, optic nerve, and primary visual cortex (V1), collect, correlate, and define normative range of values for both objective and standardized tests

In Year 2 we submitted the forms and protocol to our local IRB3 Human Use Committee and received IRB approval. This was followed by final approval by Brigit Ciccarello after submission to ORP HRPO after their second-level review and approval was received. The approval process took longer than anticipated. During Year 3, while waiting to secure a clinical testing suite in the Ophthalmology Department at the University of Iowa, we took advantage of this time to further refine our software and hardware capabilities for testing the pupil light reflex, visual evoked potentials from the eye and visual cortex, and eye movement tracking to vanishing optotypes. We subsequently submitted a two year, no cost extension of the grant in order to continue with the planned testing.

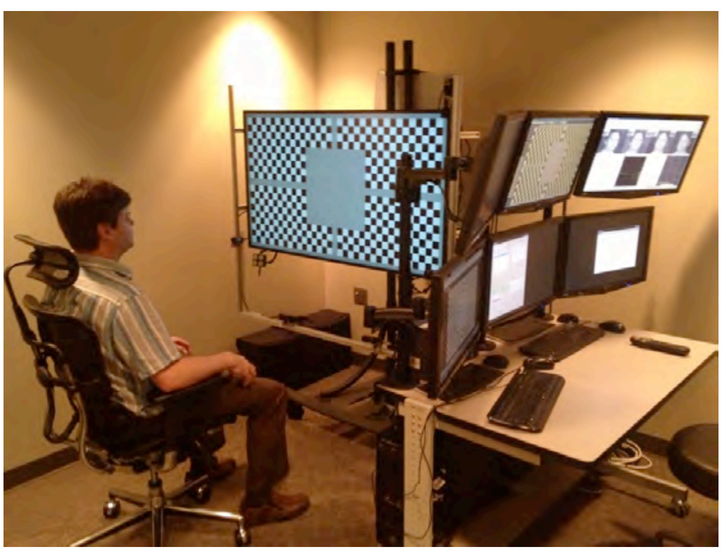

Figure 16. Clinical testing space acquired within the confines of the Ophthalmology Clinic. The test subject sits comfortably in front of a large screen, which can present a large range of light stimuli, varying in color, intensity and size which are used to elicit objective responses such as EMG of the orbicularis and procerus muscles, skin conductance and heart rate.

During Year 4, we started testing normal subjects and patients to further optimize our stimulus protocol for reducing inter-subject variability and maximizing the detection of disease (see Figure 16). We collected data from normal subjects, as well as from patients with unilateral optic nerve damage caused in one case by a pituitary tumor compressing one side of the chiasm and in one case from anterior ischemic optic neuropathy (AION). Subjects were tested using the same protocols and data was collected for 1) pupil light reflexes, 2) evoked potentials, 3) eye movements to targets changing in resolution, and 4) standard light threshold perimetry.

During the analysis process, we adapted the software tools we have developed as part of our other DOD/TATRC research project, titled "Use of the Photo-Electromyogram to Objectively Diagnose and Monitor Treatment of Post-TBI Light Sensitivity" to expedite data analysis and interpretation of results. We have reported elsewhere that we had implemented a Matlab GUI-enabled tool for reviewing and visualizing video and time series data within a unified and user-specified framework, simply by specifying the relevant input data sources and GUI layout parameters for each type of data recording session. Video and time series data are synchronized based on timestamps. The GUI enables the user to play back, rewind, etc. recorded data, and easily navigate to any time slice by clicking in any of the linked graphs, as well as jump to any specific stimulus epoch. The video frame that is displayed for each video stream is calculated on the fly and based on the current timestamp. The user has the ability to specify the number of graphs, as well as how each time series is to be assigned to any Y axis (both left and right for each graph), and can use the mouse-controlled crosshair to read off the x, y1 (left), and y2 (right) coordinates on any graph. The user can also record the GUI window in order to create movie clips for presentations, etc.

For the purposes of this report, we would like to describe the results for two tests, namely the red-blue pupil light reflex test, as well as the evoked potential test. Based on the Matlab GUI-enabled tool described above, Figure 17 and Figure 18 show examples of video and pupil data collected during the red-blue pupil light reflex test from the patient with AION with the Neuroptics DP-2000 system and our custom DynaScan-Smart Eye system. During this test, a series of 1s red and blue stimuli of varying intensities are presented to each eye separately or to both eyes simultaneously. As mentioned earlier in this report, we have developed a novel method to objectively diagnose the presence and severity of optic neuropathy within an individual eye independently, without having to reference it to the other eye as an asymmetry index. For this method, the % pupil contraction to a bright red stimulus is compared to the % pupil contraction to a bright blue stimulus as sustained 6s after stimulus onset. Comparison of the red vs. blue pupil response within each eye minimizes the impact of central nervous system influences on measurements of visual function and pupil response that are unrelated to the condition affecting vision. Such central nervous system influences having to do with state of excitement or sleepiness can cause fluctuations in the response of the pupil unrelated to the eye's function and can confound the diagnosis of ocular disorders. Results for the patient with AION are tabulated in Table 1 for both the Neuroptics DP-2000 system and our custom DynaScan-Smart Eye system.

Normal Left Eye Stimulated with Blue Light

Abnormal AION Right Eye Stimulated with Blue Light

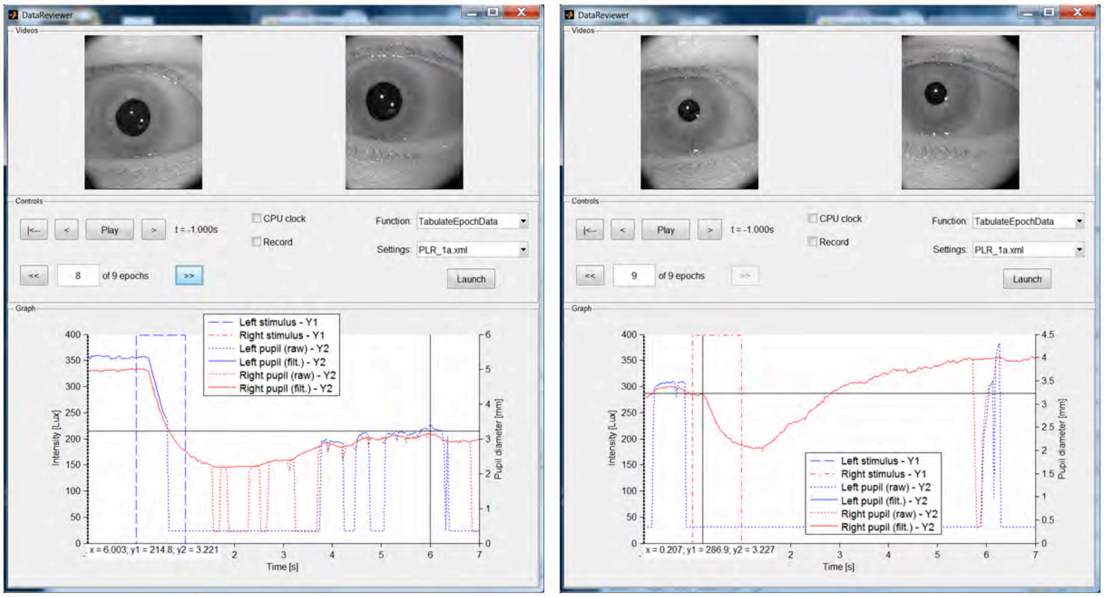

Figure 17. Screenshots of the Matlab GUI tool populated with data collected from the Neuroptics DP-2000 system for the patient with AION in the right eye in response to two stimuli. On the left hand side, pupil responses for a 1s bright blue stimulus delivered to the left (healthy) eye are shown. Pupil responses for a 1s bright blue stimulus delivered to the right (diseased) eye are shown on the right hand side. In this example, data are displayed for t=-1s before stimulus onset (as indicated by the vertical black dotted line in each graph), while each pair of video frames is showing the eyes at this time instance (right eye with AION stimulated; right panel showing right and left pupils, and left normal eye stimulated; left panel showing right and left pupils). Note that the blue stimulus for the right eye is delivered only 15s after the blue stimulus has been delivered to the left eye. This short inter-stimulus interval doesn't allow the pupils to recover sufficiently to dark-adaptation levels, which leads to reduced % contraction values for the right eye stimulus if not corrected, and can confound interpretation of the results given the fact that the right eye is also the diseased eye (AION). Possible solutions are either lengthening of the inter-stimulus interval between the bright blue stimuli, correcting for the significant pupil baseline discrepancy or instead using the % dilation from the minimum pupil size. Also note that the pupil tracking algorithm failed to locate the pupil border of the left eye (blue tracing) for most of the time when the right eye was stimulated (right panel in this figure).

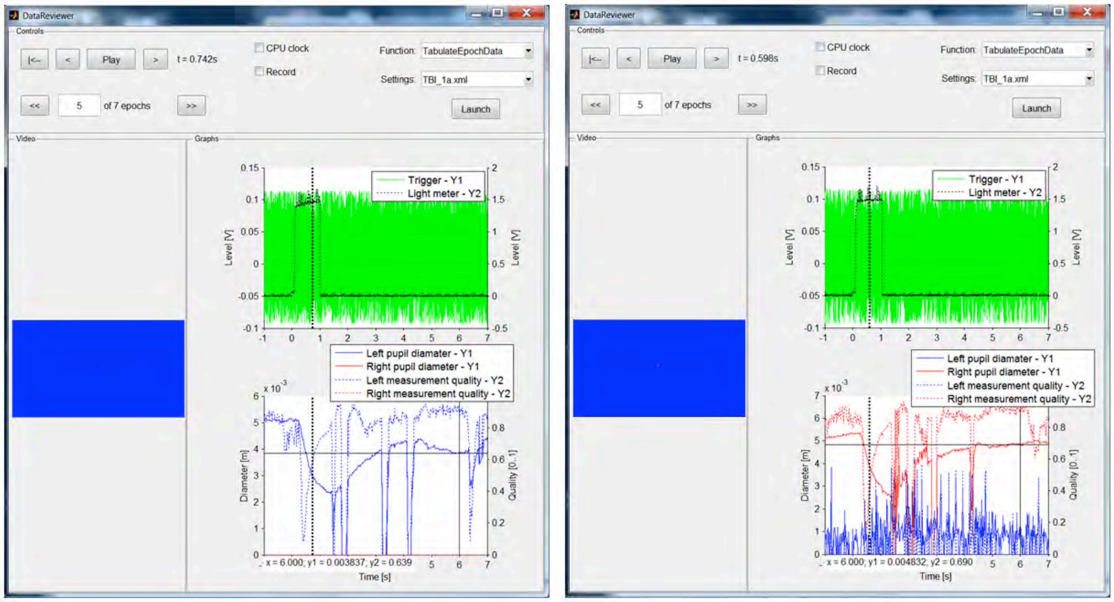

Figure 18. Screenshots of the Matlab GUI tool populated with data collected from our custom built DynaScan-Smart Eye system for the patient with AION in the right eye in response to two stimuli. On the left hand side, pupil responses for a 1s bright blue stimulus delivered to the left (healthy) eye are shown. Pupil responses for a 1s bright blue stimulus delivered to the right (diseased) eye are shown on the right hand side. In this example, data are displayed for instances of time during the 1s stimuli (as indicated by the vertical black dotted line in each graph), while the video frames show the screen contents displayed to the subject (in this case, a blue screen). Note that stimuli are not alternated between eyes in case of the DynaScan-Smart Eye system because the subject has to wear a filter in front of the eye not being tested to block light from the TV, as described in the previous progress report. Each eye is therefore tested independently. Also note that the sustained response to a bright blue stimulus delivered by the DynaScan TV is reduced compared to the response observed with the Neuroptics DP-2000 system probably because of the broad spectrum of the blue light emitted by the TV (as measured and described in the previous progress report), as well as the fact that we have not been able to keep the testing environment with the TV as dark as is possible during testing with the Neuroptics DP-2000 system.

Table 1. Results for the red-blue pupil light reflex test from the patient with AION with the Neuroptics DP-2000 system and our custom DynaScan-Smart Eye system. For both test platforms, the % pupil contraction value sustained at 6s after a bright blue stimulus is reduced for the diseased right eye (OD) in comparison to the healthy left eye (OS), while the pupil response to the bright red stimulus has dissipated by 6s. Note that the baseline pupil size for the right eye (OD) blue stimulus from the Neuroptics DP-2000 system has been adjusted to match the dark adaptation baseline for the right eye (OD) red stimulus, and the derived contraction values are marked with an asterisk.

Stimulus	Neuroptics DP-2000						DynaScan-Smart Eye					
	baseline (mm)	min. (mm)	@ 6s (mm)	% max. contraction	% contraction @ 6s	% dilation @ 6s	baseline (mm)	min. (mm)	@ 6s (mm)	% max. contraction	% contraction @ 6s	% dilation @ 6s
OS - red	4.8	2.5	4.6	48%	**4%**	**84%**	4.9	2.3	4.8	53%	**2%**	**109%**
OS - blue	5.2	2.2	3.2	58%	**38%**	**45%**	5.1	2.3	3.8	55%	**25%**	**65%**
OD - red	5.0	2.6	4.8	48%	**4%**	**85%**	5.2	3.0	5.2	42%	**0%**	**73%**
OD - blue	5.0* (3.4)	2.1	4.0	58%*	**20%***	**90%**	5.3	2.4	4.8	55%	**9%**	**100%**
OU - red	4.9	2.4	4.7	51%	4%	96%	4.9	2.3	4.7	54%	3%	109%
OU - blue	4.9	2.1	2.8	57%	43%	33%	5.1	2.3	4.3	55%	16%	89%

In addition to the red-blue pupil light reflex test, we have also collected evoked potential data for the AION patient with the DynaScan-Smart Eye system. Overall, VEP responses are significantly

attenuated when the diseased right eye is stimulated when compared against the VEP responses from stimulation of the healthy left eye or of both eyes simultaneously. Results are shown in Figure 19. The observation that the patient had greater difficulty to stay fixated on the fixation target during stimulation of the (diseased) right eye (OD condition) paved the way towards the conceptualization and development of the "**Novel clinical eye fixation/movement test during routine OCT tests**", described in more detail later in the report.

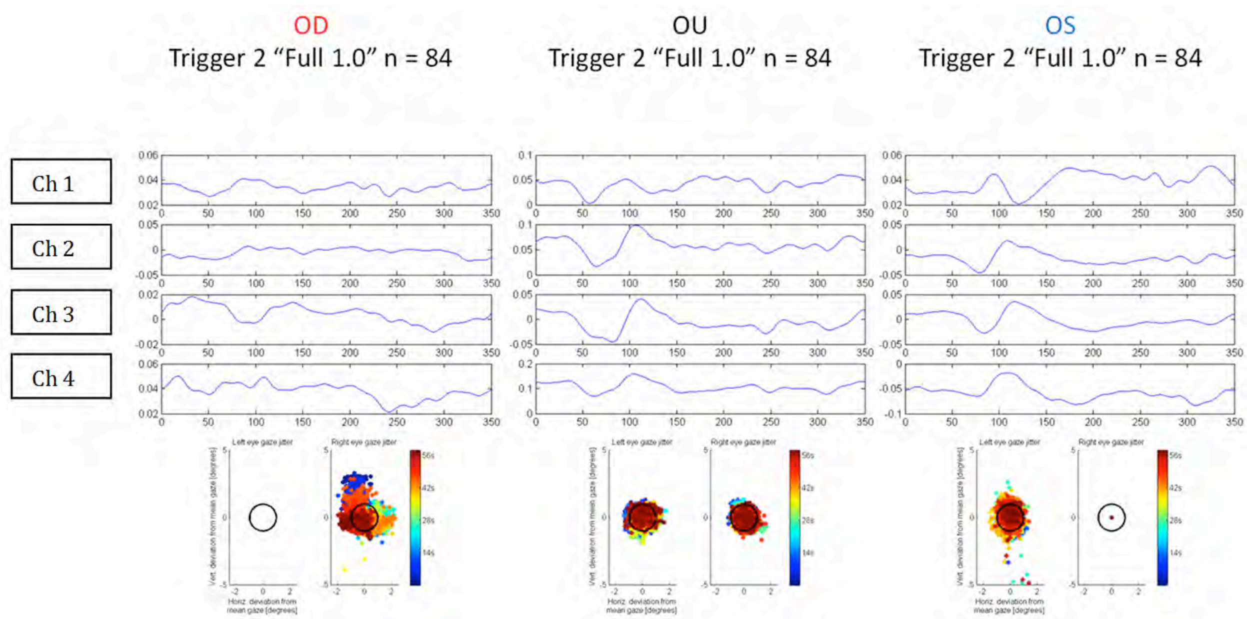

Figure 19. VEP response functions for 4 EEG channels in response to full-field 1° checkerboard pattern onset/pattern offset stimulation for 3 testing conditions: right eye (OD) stimulation on the left hand side, both eye (OU) in the center, and left eye stimulation (OS) on the right hand side. The C1 (@80ms) and C2 (@110ms) peaks are clearly visible in channels 2 and 3 for the OU and OS test conditions, but attenuated for the OD condition. Gaze offsets are shown below each set of VEP graphs, colored coded according to the time offset of each gaze point with respect to the beginning of the test, which lasts for about 60s. The black circle on each gaze jitter graph represents 1° offset with respect to the mean gaze vector during the test. Note that the patient has greater difficulty to stay fixated on the fixation target during stimulation of the (diseased) right eye (OD condition).

We described earlier the finding that the melanopsin mediated pupil response, derived from the differential sustained pupil response to blue light vs. red light, correlates highly with retinal ganglion cell layer thickness derived from optical coherence tomography (OCT) in eyes with optic neuropathy due to multiple sclerosis. At the time, we hypothesized that it would pave the way for determination of afferent input of each eye independent of the other and will be especially useful in patients with bilateral disorders of visual function, in which there may not be a relative afferent pupil defect. During Year 4, we set out to evaluate the diagnostic implications of such a simple pupil light reflex test. The following test case paved the way towards the conceptualization and development of the "**Test for detecting optic neuropathy independent of the fellow eye which highly correlates to visual field volume**", described in more detail later in the report. The example is from a patient with right eye visual loss and optic nerve damage from an optic nerve sheath meningioma compressing the right optic nerve. The left eye was normal. In Figure 20, pupil tracings for red and blue stimuli, matched for photopic intensity, are shown for right and left eye stimuli, while recording both pupils. A deficit in both the initial pupil contraction to red and blue stimuli is seen with the right eye stimulus. In addition, the sustained pupil contraction, normally

seen after a 1-second bright blue light stimulus, was not present, indicating damage to the retinal ganglion cells containing melanopsin. The patient was treated with radiation therapy and 4 months later returned with much improved vision and visual field. The patient's pupil contractions were also significantly greater, for both the initial contraction to red and blue light and she also showed an increase in the sustained pupil contraction to the blue stimulus. This example shows the utility of the initial pupil contraction to red and blue light stimulus for detecting disease in each eye and the utility of assessing the sustained pupil contraction to the blue light stimulus with respect to the red light stimulus. In addition we show here the utility of the pupil responses to red and blue light for monitoring treatment, which will have a significant clinical application.

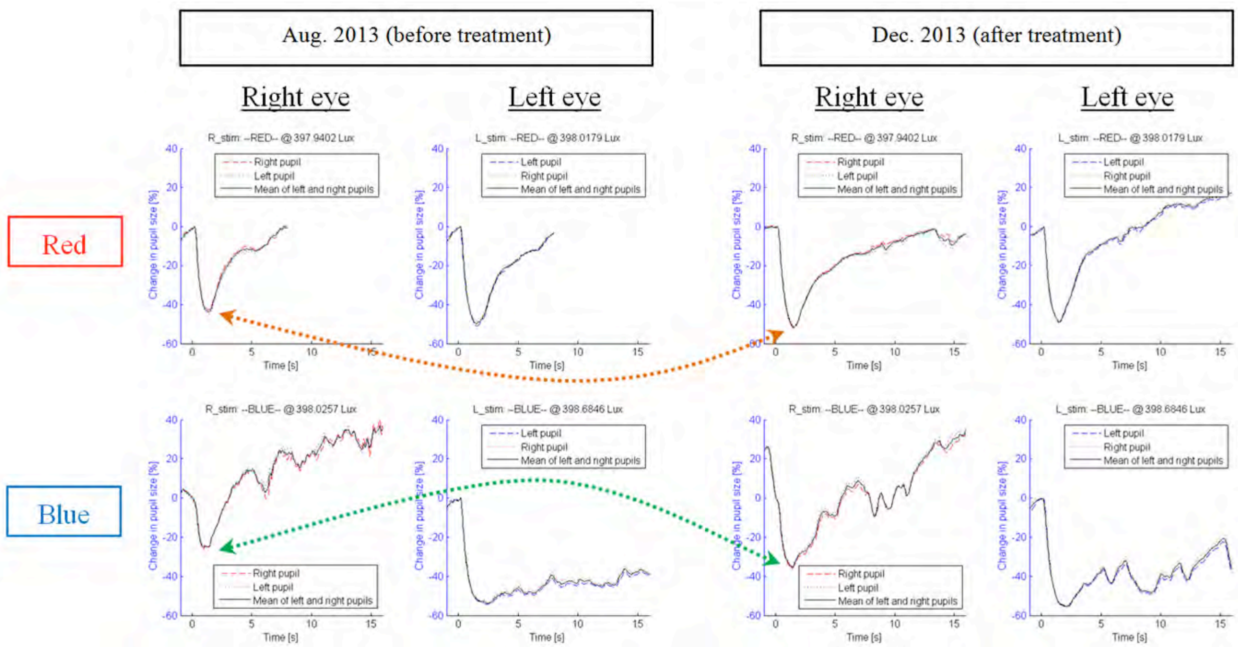

Figure 20. Raw pupil size tracings in response to individual stimulation of each eye with red and blue 1 second duration bright light stimuli before and after treatment. Each graph includes the tracings of the left pupil, right pupil, and the mean of the left and right pupil for the different eye and stimulus color combinations. Note the increase in the initial pupil response to both red light (orange arrow), as well as blue light (green arrow) following treatment.

Task 5. Optimize hardware systems and vision testing protocols to reduce testing time, maximize the signal/noise, and minimize cognitive demands placed on the patient for proposed objective tests

Overall, a significant effort was spent to optimize hardware systems and to design, implement, and evaluate numerous vision testing protocols to reduce testing time, maximize the signal/noise, and minimize cognitive demands placed on a patient being tested. We developed various discriminators of visual pathway dysfunction and location by testing normal participants and those with well-defined visual field defects from damage to specific sites in their visual pathway (e.g. retina, optic nerve, etc.). We carefully selected visual stimuli and developed innovative analysis approaches to optimize signal-to-noise ratios. As needed, we applied receiver-operator-characteristics (ROC analysis) and statistical analysis to validate discriminators and to determine sensitivity and

specificity for detecting visual dysfunction. As part of the final report, various presentations and publications, we synthesized research findings and specified the design parameters and testing protocols of a suite of objective tests capable of freeing TBI patients from the cognitive demands placed on them during standard visual testing. A detailed description of the efforts and the development and validation of novel, objective tests under this task follows below.

a) <u>Upgrade to multi-camera eye movement monitor (Smart Eye AB)</u>
During Year 4, Smart Eye delivered an upgraded 120 Hz digital 4-camera head and eye tracking system to us. One of Smart Eye's image analysis experts visited our lab for a 2-day on-site visit to install and provide training for the new system, as well as assisted us to optimize the positioning of the 4 IR cameras around the DynaScan TV. Given that the Smart Eye system allows one to arrange the IR cameras in different configurations, we wanted to ensure that the system is optimized to track large rotations of a subject's head (not just sideways head movements) while still tracking both eyes and pupils robustly. The new system contained the following upgrades:

- At a 120 Hz, the sampling rate is double the sampling rate of the previous generation head and eye tracking system, which enables denser sampling of saccadic eye movements as well as eyelid dynamics.
- The system is able to record the raw, uncompressed video streams from the 4 cameras to disk at 120 Hz, while simultaneously tracking head and eye movements at 120 Hz. This capability enabled us to both make use of the head/eye tracking data for experiment control and monitor the quality of the tracking data in real time while the raw video data are also saved at the same time to allow additional image analysis afterwards.
- The time consuming task of building and registering a head model for each subject has been fully automated. The experimenter simply has to press a button to activate the system's tracking mode, which instructs the software to start the process of constructing a head model automatically, and fine-tuning the model over time. This capability is especially useful in case of young and/or uncooperative patients. Knowing both the head and eye position simultaneously in real time will allow unprecedented control of visual stimuli and analysis of responses.
- Previously, in order to estimate the optical axis of an eye, the software algorithm required that the eye had to be visible in at least two camera images. However, the latest version of the software makes better use of head and facial features to locate the head and eyes in 3D, which relaxes the requirement for any eye to be visible only in a single camera view, allowing us to increase the distance between neighboring cameras and therefore enabling us to track an even bigger range of head and eye orientations than possible with our existing system.

b) <u>Upgrade of stimulus monitor</u>
In Year 2, we replaced the existing LN52B750 52" LCD TV in our multi-modal test platform with a prototype super bright large-screen display system (based on a 55” 1920 x 1080 LED TV platform) from DynaScan Technology, Inc. in Irvine, CA. This monitor is unique to other visual displays because it can deliver a maximum white level brightness of 5,000 cd/m^2, compared to 300-700 cd/m^2 for standard TVs and monitors. This monitor enabled us to use the same display unit to present both bright chromatic stimuli for pupil light reflex measurements, as well as present moving targets for eye movement and pattern stimuli for evoked response (VEP) tests. A combined

stimulus presentation system allows for a reduction in testing times through leveraging the same infrastructure for all three testing paradigms (pupil, eye movements and electrical responses to visual stimuli), and reduce the footprint of the test equipment.

In Year 4, we collected calibration data for our super-bright DynaScan TV to enable us to accurately relate and compare ocular response measurements from different clinical stimulus presentation platforms – such as the Neuroptics DP-2000 desktop pupillometer and the Diagnosys Ganzfeld bowl stimulator – with response measurements collected from our integrated TV-based system (i.e., DynaScan TV). Dr. Chris Johnson assisted us in taking radiometric readings with three different types of light meters; a Photo Research PR-655 SpectraScan® Spectroradiometer (radiometric), and photopic light level readings with a PR-1980A Pritchard® Photometer and Extech Foot Candle Light Meter. The different readings are shown in Table 2 with illustrations and plotted in color space in Figure 21 below. Apart from chromaticity values, we were also interested in calibration data for the range of brightness levels for the DynaScan TV, given that we have to turn off the light source of the TV – by setting the brightness level to 0% – during inter-stimulus intervals of pupil light reflex experiments in order to maintain a sufficiently dark environment for light off conditions of testing. We have also updated the experiment control software to dynamically alter the brightness levels of the TV in addition to setting RGB values for optimizing the spectral distribution of both low and high intensity red and blue 1-second flashes that we are using to elicit pupil light reflexes.

Table 2. Radiometric data collected from DynaScan monitor using the Photo Research PR-655 SpectraScan® Spectroradiometer.

<table>
<tr><th>Color</th><th>Chromaticity Values</th><th>Spectral Distribution</th></tr>
<tr><td>Black
sRGB = [0;0;0]
@ 50% brightness</td><td>
</td><td>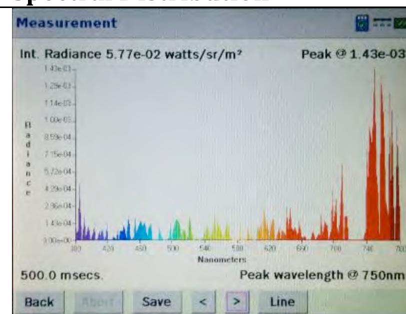
</td></tr>
<tr><td>Red
sRGB = [255;0;0]
@ 50% brightness</td><td>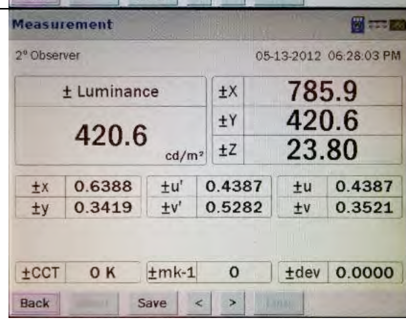
</td><td>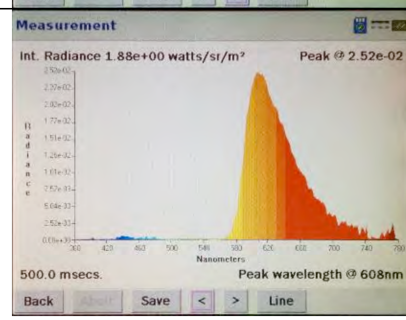
</td></tr>
<tr><td>Green
sRGB = [0;255;0]
@ 50% brightness</td><td>
</td><td>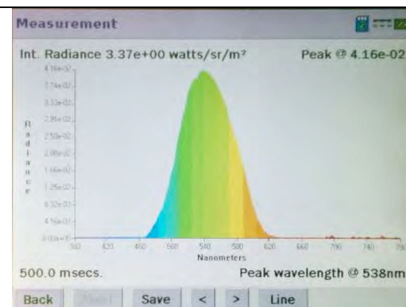
</td></tr>
<tr><td>Blue
sRGB = [0;0;255]
@ 50% brightness</td><td>
</td><td>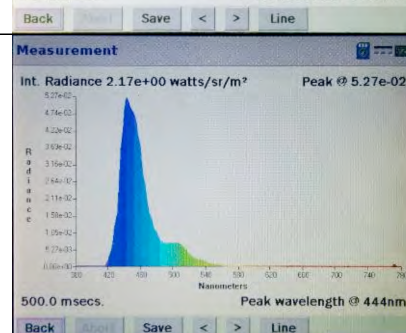
</td></tr>
<tr><td>White
sRGB = [255;255;255]
@ 50% brightness</td><td>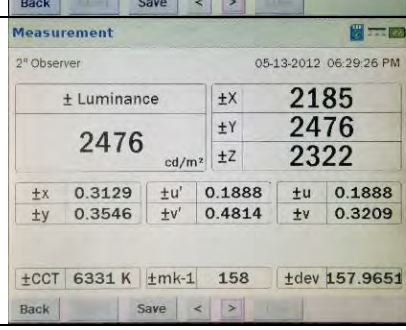
</td><td>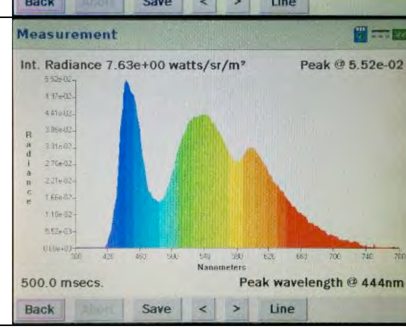
</td></tr>
</table>

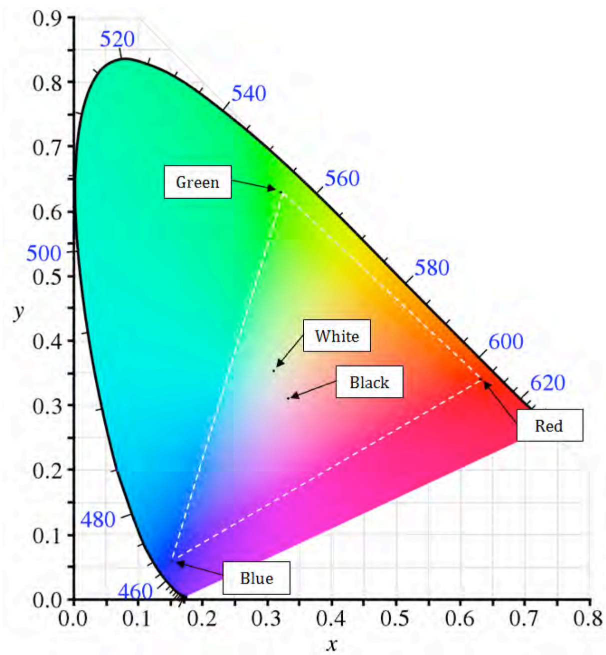

Figure 21. CIE chromaticity values for the DynaScan TV monitor which will be used for combined testing of the pupil light reflex, eye movements to visual stimuli and visual evoked responses from the eye and visual cortex.

Figure 22 and Table 3 demonstrate that the light intensity response (luminance) of the DynaScan monitor is highly linear with the software luminance settings for each of the spectral stimuli (red, green, blue and white).

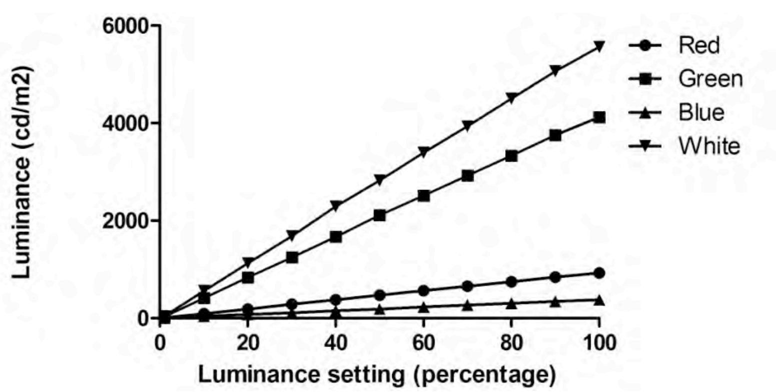

Figure 22. Brightness level (luminance) settings (x-axis) and the corresponding photopic luminance readings recorded by the PR-1980A Pritchard® Photometer. The linear regression goodness-of-fit r^2-values are better than 0.999 for all colors.

Table 3. Illuminance readings in lux recorded with the Extech Foot Candle Light Meter at 7 feet in front of the DynaScan TV.

Brightness level	Red	Green	Blue	White
1%	-	6.5	-	7.5
2%	0.2	17.2	-	22.6
3%	5.4	24.8	1.1	32.3
5%	7.5	43.1	2.2	56.0
20%	37.7	183.0	10.8	236.8
50%	95.8	466.1	29.1	602.8

80%	152.8	742.7	46.3	963.4
100%	190.5	920.3	58.1	1197.0

In order to measure a subject's monocular input for eliciting pupil light reflexes, eye movements and VEP responses, we have assembled two pairs of comfortable, disposable, over sized ocular frames, commonly used as eye shields in the operating room. The goal is to occlude the visible light stimulus to either the right or left eye while still being able to track eye and pupil movement by infrared light and our infrared sensitive video cameras. One pair is fitted with an infrared (IR) filter covering the left eye, and the other pair with an IR filter covering the right eye (see Figure 23). The IR filters were initially cut from Kodak Wratten 87C sheets. The 87C filter attenuates slightly too much IR illumination of the covered eye while blocking visible light, resulting in suboptimal tracking of the covered pupil by the Smart Eye head and eye tracking system. Subsequently, we fitted type 87 IR filters to maximize the IR illumination of the covered eye while minimizing leakage of long wavelength red light from the TV through the filter (see Figure 24).

Figure 23. IR filters fitted to two pairs of glasses for covering either the left (red pair) or the right eye (green pair) to block visible light from the DynaScan TV during monocular testing conditions, yet transmit infrared light emitted from directional infrared emitting diodes (LEDs). The other eye sees through a wide window cut in the clear plastic film.

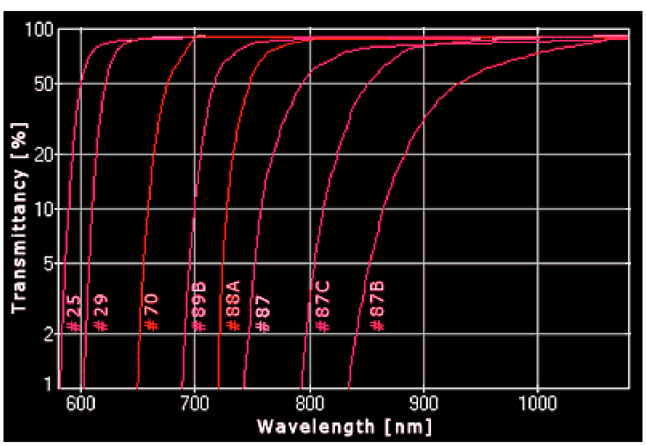

Figure 24. Transmission spectral distributions of different Kodak IR filters. Initially, we used type 87C, but settled on type 87 in order to maximize the IR illumination of the covered eye needed by the Smart Eye head and eye tracking system to track the covered pupil. This also minimized transmission of visible long wavelength red light from stimuli provided by the TV.

c) <u>Pupil light reflex - Fast, automated log unit relative afferent pupillary defect (RAPD) test</u>

In Year 3, we developed a test protocol and associated data analysis routines to derive metrics that correlate with clinical diagnoses of afferent and efferent pathway pathologies based on the pupil light reflex. The test protocol consists of white light impulses across a range of intensities (1-400 lux) presented sequentially to each eye individually, while the pupil diameter of both eyes are recorded continuously. In order to minimize subject's testing time fatigue, the protocol is approximately 22 seconds in duration, but during this time period, each eye is stimulated 8 times (which includes the binocular stimulus at the start of the protocol to drive the pupil size down from its dark adaptation level closer to its steady-state size during the test). We have implemented the protocol on the Neuroptics DP-2000 system and have tested both normal subjects and patients in order to build up a database of pupil responses.

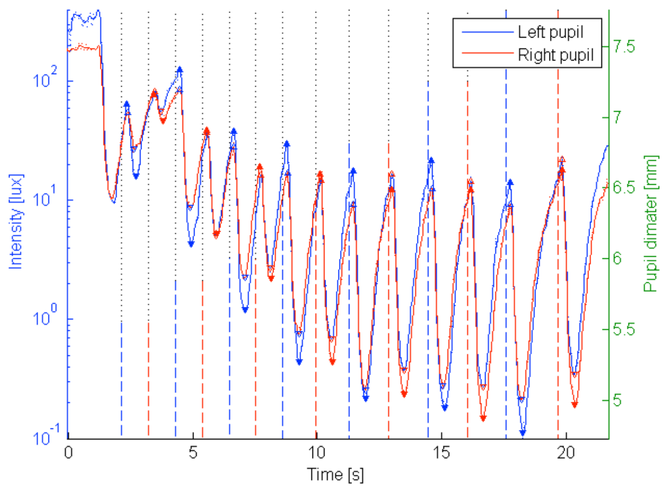

Figure 25. Example data record of filtered pupil size tracings (Left pupil size in solid Blue line, and Right pupil size in solid Red line) and the onset time and intensity of the monocular stimuli (Left eye stimulus in dotted Blue line, and Right eye stimulus in dotted Red line). The intensity of the white light stimuli is indicated in lux on the y-axis on the left hand side, and the y-axis on the right hand side indicates pupil size in millimeter.

Subsequent to data collection, each subject's pupil data is pre-processed before it can be committed to the database of pupil responses. Pre-processing includes low-pass filtering of each eye's pupil size time series to smooth out high frequency noise components inherent to the frame-by-frame image analysis to find the best-fit circle matching the pupil border in the video frames, as well as locating and estimating the pre-response peak dilation pupil size and the minimum contracted pupil size for both eyes for calculating the maximum contraction amplitude in response to each stimulus. In the DP-2000 system, stimulus onset timing is not synchronized to video frame shutter timing, and neither is the shutter timing of the left eye camera synchronized with the shutter timing of the right eye camera. However, the system timestamps every stimulus onset event, as well as each video frame collected by the left and right eye cameras. To work around the lack of synchronization, the next pre-processing step involves isolating (i.e., cutting out) and resampling of the pupil time series for each stimulus-pupil response waveform based on the timestamp value of each stimulus and cubic spline interpolation. This step allows us to overlay and inspect the pupil response tracings by setting the stimulus onset time to zero for each stimulus-pupil response pairing as shown in Figure 26.

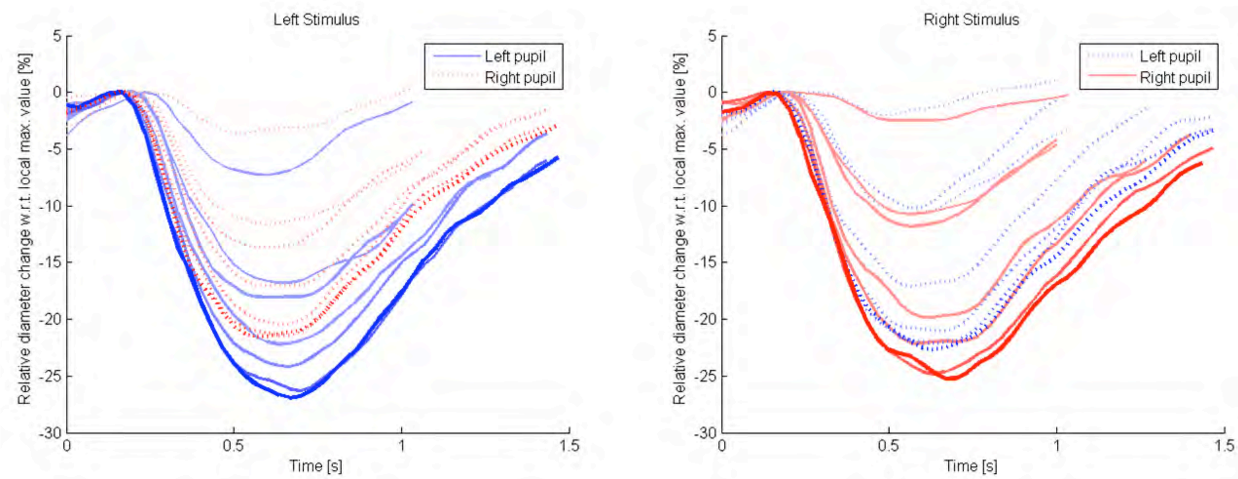

Figure 26. Example left and right pupil tracings for each of the left and right monocular stimuli. Color saturation of the different line series is determined by stimulus intensity, i.e., darkest Blue and Red colors correspond to the brightest stimulus conditions (which, in this case, is ~400 lux).

The short duration of the test protocol means that the pupil size at the start of each stimulus is not the same. Based on results published by the PI previously, translation of each pupil response tracing into time series of percentage contraction values helps to alleviate the impact of varying pupil start sizes on subsequent statistical analysis. The next processing step therefore consists of normalizing the values of each stimulus-pupil waveform to represent the percentage change from the pre-response peak dilation pupil size, as calculated in an earlier step, for each individual stimulus. At this point, a subject's pupil data has reached a sufficient level of processing for comparison with data from other age-matched subjects. In future, a subject's data can be committed to a database (e.g., MySQL) at this stage for data warehousing purposes. A well-designed database will support many types of statistical analyses within specialized statistical packages (e.g., R, SPSS, etc.) by leveraging the ability to easily obtain data for analysis purposes via database queries.

In order to compare pupil responses within a subject (i.e., one-to-one), or to compare a subject's left and/or right eye stimulus-pupil response with a matched population averaged response for diagnostic purposes (i.e., one-to-many), we have derived a novel computational method to support such data comparisons. The method is based on estimating a field of pupil responses across a range of stimulus intensities through a series of curves fitted to the normalized pupil responses for the discreetly sampled stimulus intensities at pre-determined time offsets from stimulus onset. A pupil response field can be used to describe the responses of a single pupil recorded at a finite number of stimulus intensities, or be used to summarize the pupil responses from multiple sources (e.g., for all aged matched normal subjects in a database). The method also enables data comparisons in the face of missing or mismatched stimulus intensities. Missing stimulus intensities would include the case for which a recorded response is rejected due to noise or artifact contamination. Several types of curves can be fitted, each having its own benefits and drawbacks. The available curves include the generalized hyperbolic, power, generalized logistic, and Naka-Rushton functions. Figure 27 shows an example of curves fitted at different time offsets. The method is also capable of computing the best-fitting response within any pupil response field (e.g., from a database) given a test pupil response waveform, and to report the matching stimulus intensity, as shown in Figure 28. We have extended this idea to calculate the “continuous” RAPD, which is how the RAPD (in log units) is

affected over a range of stimulus intensities as shown in Figure 29. In this particular case, the RAPD becomes maximal at about 10 lux and then becomes less at greater stimulus intensities.

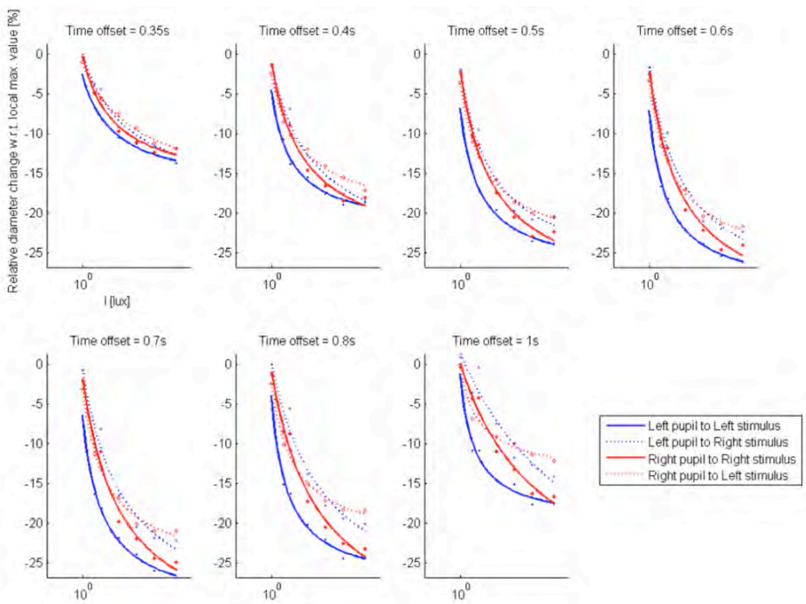

Figure 27. Example of a generalized hyperbolic function fitted to normalized pupil responses across several stimulus intensities at different time slices from stimulus onset. At each time point, the graph represents the pupil size at that time point during the pupil waveform for seven different intensities. By fitting the function at each time point, the pupil size at that time point in the waveform can be interpolated for small increments of intensity. This allows us to reconstruct the waveform pupil response for an entire intensity series for a stimulus to each eye (see reconstructed waveforms for the contraction part of the pupil reaction shown in Figure 28).

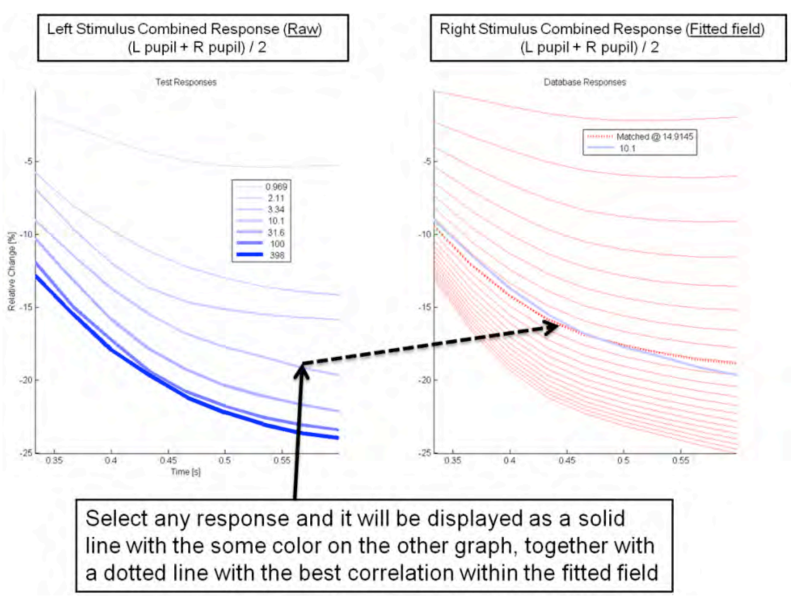

Figure 28. Comparison of waveforms from the left and right eye stimuli. Graph of waveforms is shown close up during the contraction time window of the pupil light reflex. Example of the best-fitting waveform response resulting from every 0.1 log unit increment of intensity within a pupil response field (graph on the right) given any test pupil response waveform selected from a set of measured responses shown in the graph on the left. The blue waveform resulting from a 10 lux stimulus to the left eye is superimposed on the different waveforms resulting from different stimulus intensities given to the right eye and the most correlated one is found (in this case, the right eye had to be stimulated about .25 log units brighter to give the same waveform). In this example, the response field was computed from the combined left and right pupil responses recorded for the right

stimulus, while the mean left and right pupil responses recorded for the left stimulus were used as the test responses. In this particular case, the response at 10.1 lux was selected from the left graph, while the matching stimulus intensity from the response field on the right was computed to be 14.9 lux, which represents about a 0.25 log unit relative afferent pupil defect in the right eye.

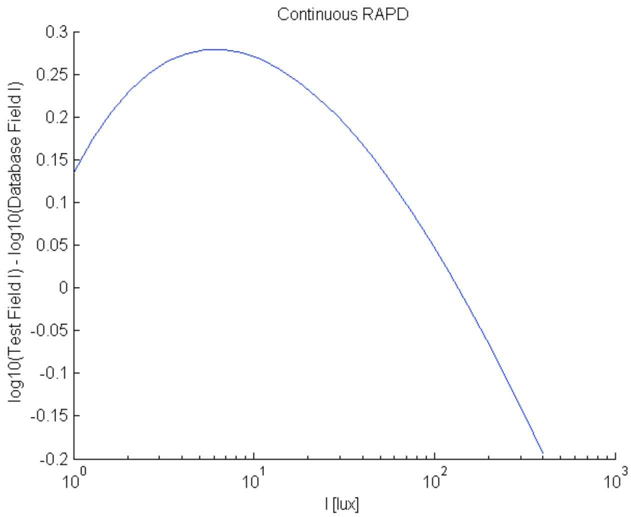

Figure 29. Example of the resultant calculated relative afferent pupil defect (RAPD) derived from the pupil waveforms (see close up of matching waveforms shown in Figure 28), as a function of light intensity used ("Continuous RAPD"). The one response field (in this case the right eye's response to light shined into it was compared against another response field (in this case the left eye's response to light shined into it). The graph for this example was calculated by first replacing the test responses in Figure 28 with a response field and then calculating the matching responses within the database response field in a continuous fashion. In other words, the derived pupil tracings from stimulus in the right eye were compared to the pupil tracings from stimulus to the left eye. The program finds the intensity of stimulus in one eye that gives the same pupil response at a fixed intensity in the other eye to derive the log unit RAPD. In the example shown there was a small right RAPD (positive numbers on the axis) that peaked at an intensity of around 10 lux (10^1).

During Year 4, we tested additional patients using the 20-second automated log unit RAPD test. The RAPD is an important objective measure of asymmetry of retina or optic nerve input between the two eyes due to disease. Compared to the smaller sample size tested initially in Year 3, we found an even higher correlation (Pearson correlation coefficient r>0.9 vs. r>0.86 before) between the machine automated determination of the RAPD and the clinical log unit RAPD determination made using neutral density filters with an alternating "swinging flashlight" test. Presently, in clinically derived RAPD measurements, one brightness level of light is used to compare the input between the two eyes. We also found a significant correlation between the automated log unit RAPD and the asymmetry of the inner retinal layer thickness (retinal ganglion cell layer), as determined by optical coherence tomography (OCT) imaging in a subset of the same patients who had permanent structural loss of retinal neurons. Furthermore, we found that the automated log unit RAPD also can be affected by how bright the alternating light level is during the test, which may be specific for different types of damage to the retina and optic nerve.

d) <u>Pupil light reflex - Test for detecting optic neuropathy independent of the fellow eye which highly correlates to visual field volume</u>

We have reported that the melanopsin mediated pupil response, derived from the differential sustained pupil response to blue light vs. red light, correlates highly with retinal ganglion cell layer thickness derived from optical coherence tomography (OCT) in eyes with optic neuropathy due to

multiple sclerosis (see Figure 30 and Figure 31). We have also hypothesized that this finding will pave the way for determination of afferent input of each eye independent of the other and will be especially useful in patients with bilateral disorders of visual function, in which there may not be a relative afferent pupil defect. Starting in Year 4, we have evaluated computerized pupillometry as an objective method for detecting retinal and optic nerve dysfunction and to compare it to the clinical gold standard of visual input testing using subjective determination of visual field sensitivity. For this purpose, 39 patients seen in the neuro-ophthalmology clinic and 44 normal subjects were prospectively tested by computerized pupillometry (DP-2000 system, Neuroptics, Inc., Irvine, CA) using a 1 second red or blue light stimulus at 1 lux and 400 lux photopic luminance units. The percent pupil contraction from baseline pre-stimulus size was calculated for the transient, initial response to the light stimulus and the sustained pupil contraction at 6 seconds following offset of light. Visual fields were obtained using standard kinetic Goldmann perimetry and the volume of visual field sensitivity was determined and correlated with pupil responses (see Figure 32). We found that the transient pupil contraction to a 1 second bright blue light gave the highest correlation with visual field sensitivity (correlation coefficient r=0.85) compared to the sustained pupil contraction (correlation coefficient r=0.52). The transient pupil contraction also provided the greatest separation between normal and abnormal eyes compared to the sustained pupil contraction (see Figure 33).

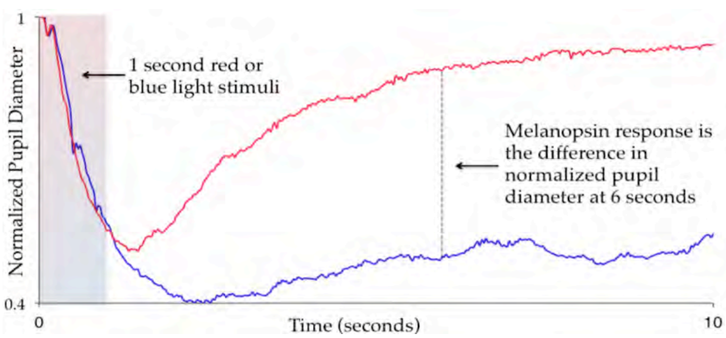

Figure 30. Graph showing the normalized pupil diameter vs. time for a normal eye. The red line represents pupil diameter as a function of time for a unilateral 1-second red stimulus of intensity 2.6 log cd/m². The pupil reaches maximum constriction shortly after the stimulus is removed and returns to baseline over a period of several seconds. The blue line represents the same experimental condition, except this time for a blue light stimulus, matched for photopic intensity. In this instance, the return from maximum constriction to baseline diameter is prolonged from 30-60 seconds. The vertical dashed line drawn at 6 seconds represents the difference in pupil diameter between the red and blue light stimuli and is what is quantified as the melanopsin mediated pupil response.

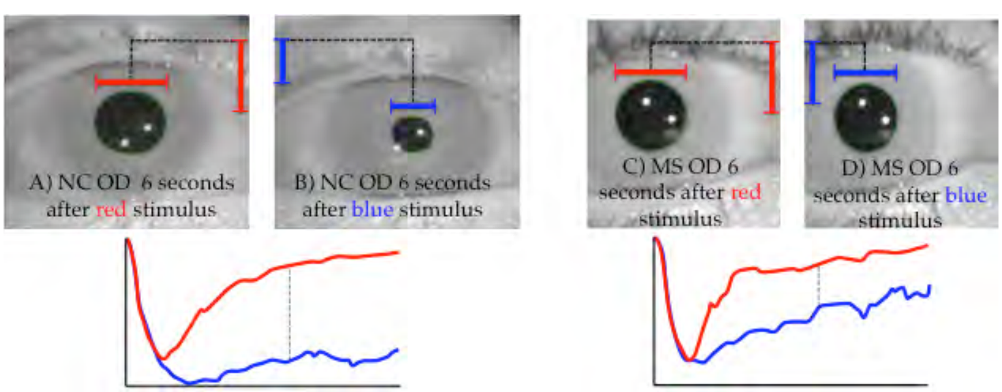

Figure 31. Left panel shows the right pupil diameter at six seconds after photopically matched red and blue light stimuli in a normal control. The captured video frames at the top show the pupil size at 6 seconds after the 1-second light stimulus for the red light (left video frame) and blue light (right video frame). The difference in pupil diameter at 6 seconds in response to the red and blue light stimulus is the melanopsin response (dashed horizontal line). Note how in this normal eye the pupil response for the red light returns to baseline by 6 seconds, but the pupil stays contracted for the blue light stimulus This is in contrast to the right panel, which shows the same experimental testing condition for a patient with multiple sclerosis, who had loss of optic nerve axons. There is a reduced melanopsin response compared to the normal eye resulting in less difference in the sustained pupil contraction at 6 seconds between the red and blue light stimuli (dashed vertical line).

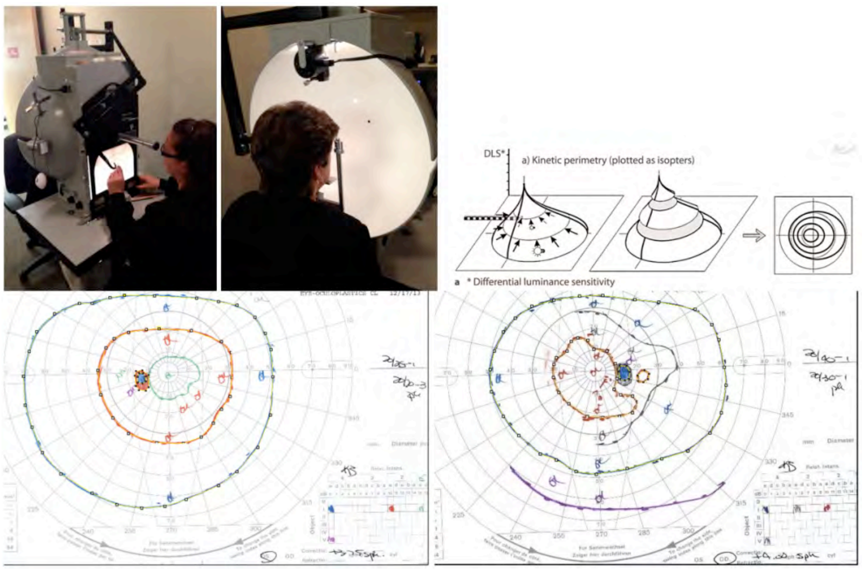

Figure 32. The visual field sensitivity was quantified using a white light spot of varying size and intensity moved across the subject's visual space in a perimetric bowl (Goldmann Perimetry). This produces a map of the visual field extent, with each target forming a concentric isopter (shown as lines coded in different colors). The area map of each isopter was then quantified after being digitized using Image J software. The summed volume was then determined.

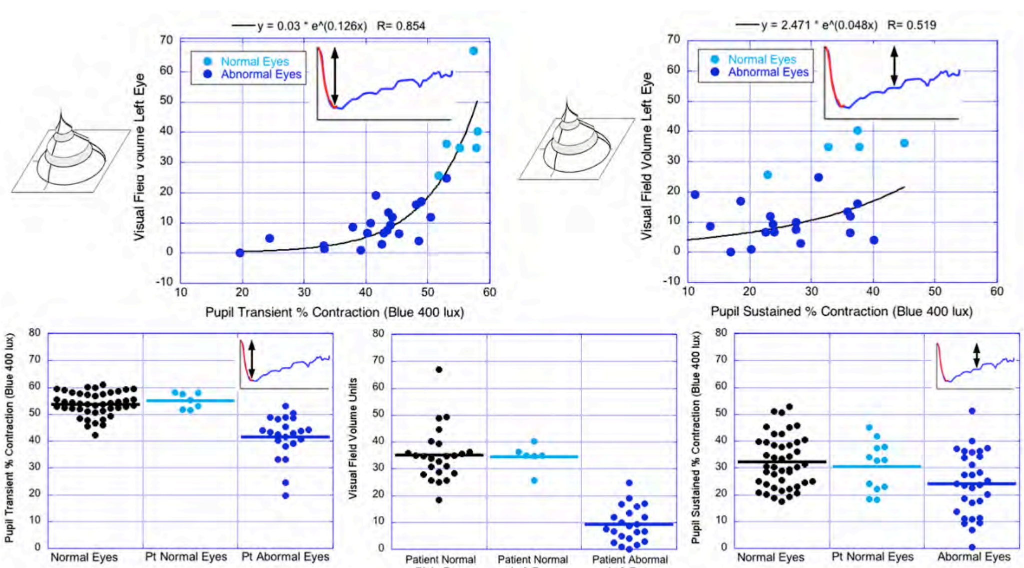

Figure 33. Pupil Response vs. Visual Field Volume: The transient pupil contraction to a 1 second bright blue light gave the highest correlation (upper left) with visual field sensitivity (correlation coefficient *r*=0.85) compared to the sustained pupil contraction (correlation coefficient *r*=0.52), shown in upper right. The transient pupil contraction also provided the greatest separation between normal and abnormal eyes compared to the sustained pupil contraction.

Based on the results, we propose that the transient pupil contraction to bright blue light provides an objective, easily recordable reflex, which correlates well with visual field sensitivity. Under these stimulus conditions, both photoreceptor input and direct activation of photosensitive retinal ganglion cells summate the visual field input to the brain. Furthermore, deficits in the outer retina or inner retina can be differentiated based on the stimulus conditions and the analysis of the transient and sustained reflex pupil contractions. The rapidity of pupil testing also provides a clinical tool for estimating visual dysfunction that has important clinical application for remote diagnosis and monitoring of vision threatening disorders.

e) <u>Pupil light reflex - Neurological Pupil Index (NPi) for acute TBI</u>

During Year 4, we found that the dynamics of the pupil light reflex, distilled into one response parameter, termed the Neurological Pupil Index (NPi) and developed by Neuroptics, Inc., Irvine, CA, appears to correlate with severity of traumatic brain injury (TBI). The NPi may be a very useful, objective indicator of acute TBI. We found that in the setting of the Emergency Room, the NPi, recorded in the trauma bays where the patients were being evaluated, predicted outcome measures. The outcome measures that were significantly related to the NPi were Glascow Coma Scale, need for admission to the hospital and duration of hospitalization, presence of abnormal head CT scan, need for neurosurgical intervention, and discharge status (home vs. care center).

We also completed our first study of the NPi in the University of Iowa Football Team. We measured the NPi in all players at preseason training camp and post-season. During the season, we also re-measured any players that were taken out of play during games for concussion evaluation. During the season, three players were taken out of play and evaluated with cognitive, neurological and balance testing each day until they were deemed fit for play. We measured the NPi in these three players on each day and compared the NPi (scale of 0-5; with 2SD of normal being from 3-5). Remarkably, in all three players, their NPi value dropped from their pre-season baseline value after the concussion and then returned to baseline by the time they returned to play (see Figure 34), further indicating that the NPi may be a valuable biological marker of TBI and would have military applications.

Figure 34. Neurological Pupil Index (NPi) is shown (y-axis) in three (3) different Iowa Football Team players being evaluated daily for concussion. The right eye NPi is shown in red and the left eye in blue. The time scale on the x-axis is in days. Note that in all 3 players the NPi decreased from pre-season baseline value and then returned to baseline at the day when they were considered fit for return to play, based on their neurological exam, balance testing, and neurocognitive testing.

f) Pupil light reflex - Manual artifact detection and removal

During Year 3, a significant effort was spent to “clean” the pupil data of artifacts in the pupil tracings caused by loss of pupil border tracking that occurs in real time during a test. After pouring over data collected from a number of subjects to support the implementation and populating of a database of age matched pupil light reflexes, we have realized that additional pre-processing of the data is required to ensure that the database is populated with data of sufficient quality.

Specifically, we have noticed that the pupil tracking algorithms used in the Neuroptics DP-2000 system (and similarly, for the Smart Eye remote eye tracking system) consistently fail to locate and correctly estimate the size of the pupil after an eye blink, or even in case of a partly covered pupil due to droopy eye lids or squinting. The failure of the tracking algorithms in these cases are mainly a result of the real-time processing requirements placed on these commercial pupil and eye tracking systems, but nonetheless causes a significant number of subpar quality or "bad" data points during the course of a pupil light reflex, which we would like to either correct or delete from a data set before it is committed to the database.

Fortunately, in case of the DP-2000 system, we have access to the raw video data, albeit at a quarter of the initial level of resolution (implemented to minimize storage requirements). Based on this need for clean data, we have spent a considerable amount of time to implement a user interface to allow an expert user to quickly and efficiently perform manual artifact detection and removal based on all available data – that is, both video and pupil tracings. We envision that the outcome of this pre-processing step will be multifold: 1) it will yield clean data for populating the database immediately; and 2) provide many instances of paired artifact and cleaned data segments that can be used to train future automated artifact detection/removal algorithms to minimize manual operations, etc.

In future, we propose to automate processing of a new patient's data before comparison against the database as much as possible, for say use in a clinical setting, and we recognize the fact that we might be able to lower the level of rigorous artifact detection/removal in case one wants to simply compare a patient's data against the database, but does not intend to add the patient's data to the database per se. Below we show several screenshots of various aspects of the pupil cleaning software interface. This allowed us to post-process the pupil data after experiments to further improve the pupil measurements even when tracking fails or when excessive blinking occurs during a test.

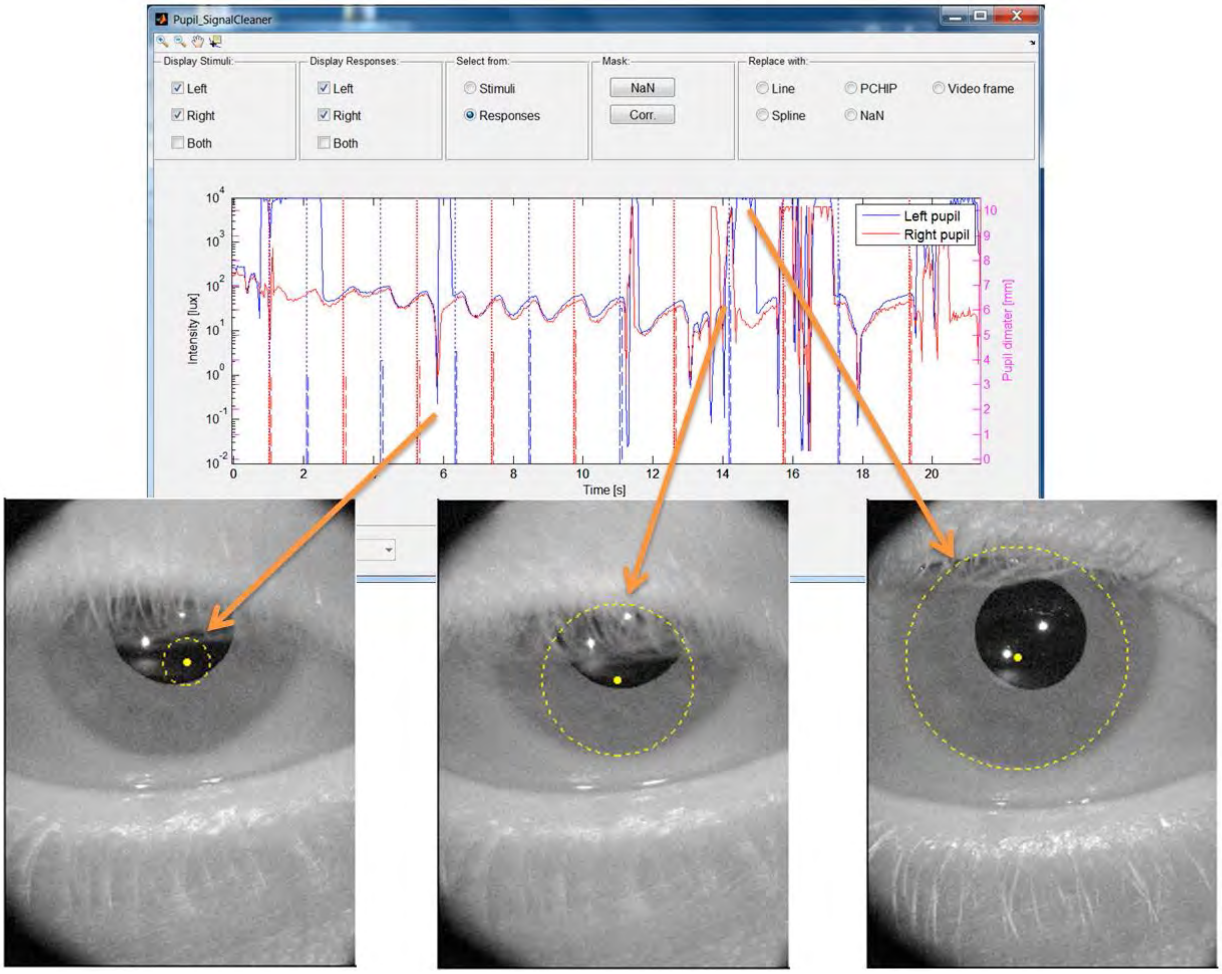

Figure 35. Three examples demonstrating the failure of the pupil tracking algorithm to locate and estimate the correct size of a pupil. It is important to note that without a video data record that is synchronized to the estimated pupil size values (as provided by the pupil/eye tracker), one would not be able to tell whether obviously "bad" pupil size data points could be salvaged (examples on the left and right), or whether a seemingly "clean" pupil size data point is correct by chance (example in the middle). If these points are not removed or corrected, subsequent data analysis steps might suffer, while the data quality of surrounding data points can be negatively impacted, such as would be the case if a digitally filter is applied to the tracing, etc. The top figure is the right(red) and left (blue) pupil waveforms (pupil diameter on the y-axis and time in seconds on the x-axis in response to a rapid repeating light stimulus varying in intensity. The video captures are shown below at different portions of the tracing, indicated by the arrows where the pupil tracking failed. Note that the camera sensor is oriented 180 degrees, so that the eye and eyelids appear "upside down". The dashed yellow circle in each captured frame of the video indicates where the Neuroptics software indicated the x-y position of the pupil and its size based on the real-time tracking algorithm that is used, which is stored in data for us to recover and superimpose on the captured video frames during the test.

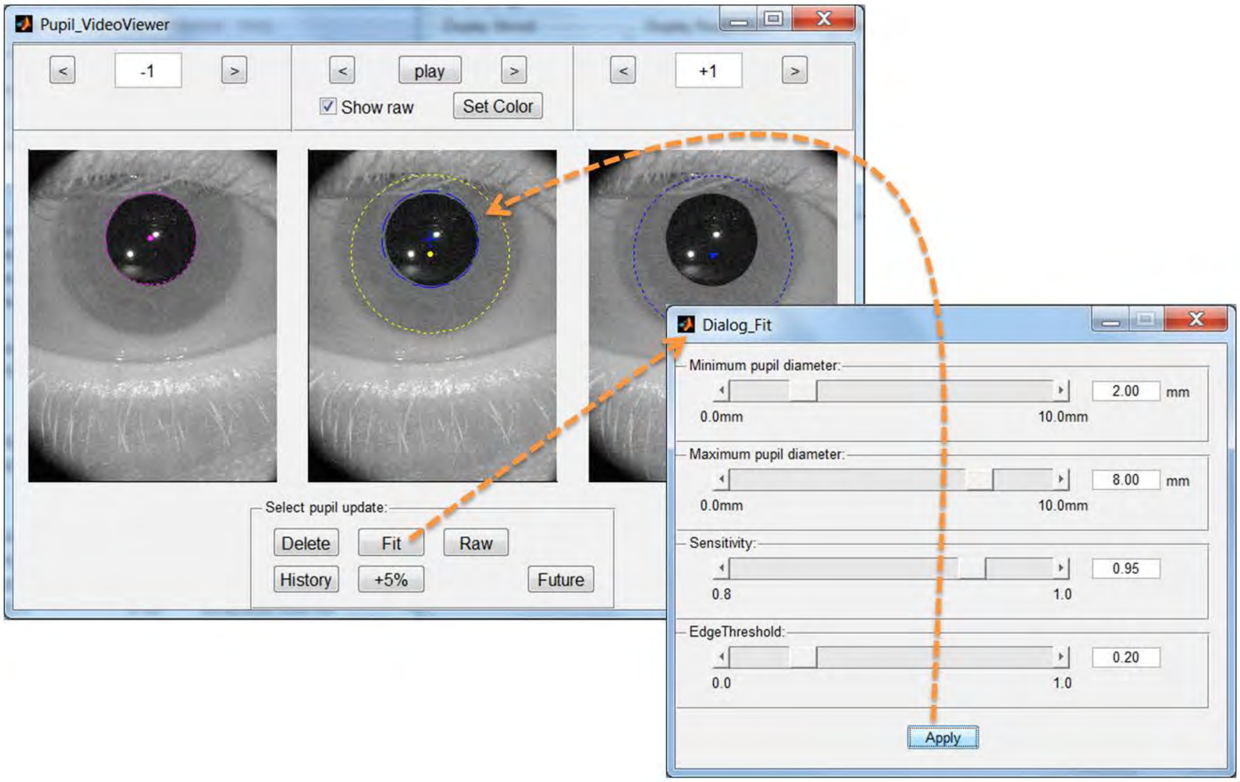

Figure 36. In case a synchronized video record is available, the expert user can launch a video editing interface to process any point on the pupil size tracing as selected from within the main interface (shown in Figure 35). Various widgets are currently implemented to change the size of the fitted pupil circle, or to drag the center of the pupil circle to a new location. For this example, the user has selected the "Fit" widget, which allows for adjusting several parameters before the Hough transformation – for finding circles in an image – is invoked by hitting "Apply". Any changes in the size of the fitted pupil circle is immediately reflected in the pupil tracing on the main user interface. In this case, the "Fit" button calls the standard "imfindcircles" function from Matlab's image processing toolbox, but we can replace it with any other functional algorithm if the need arises, or add additional buttons to the interface to activate new image analysis functions. After the new fit is applied, the resulting pupil size and location is also shown (blue circle in the middle video frame displayed), which is much more accurate than the algorithm determination that was made in real time (yellow dashed circle; obviously not accurate).

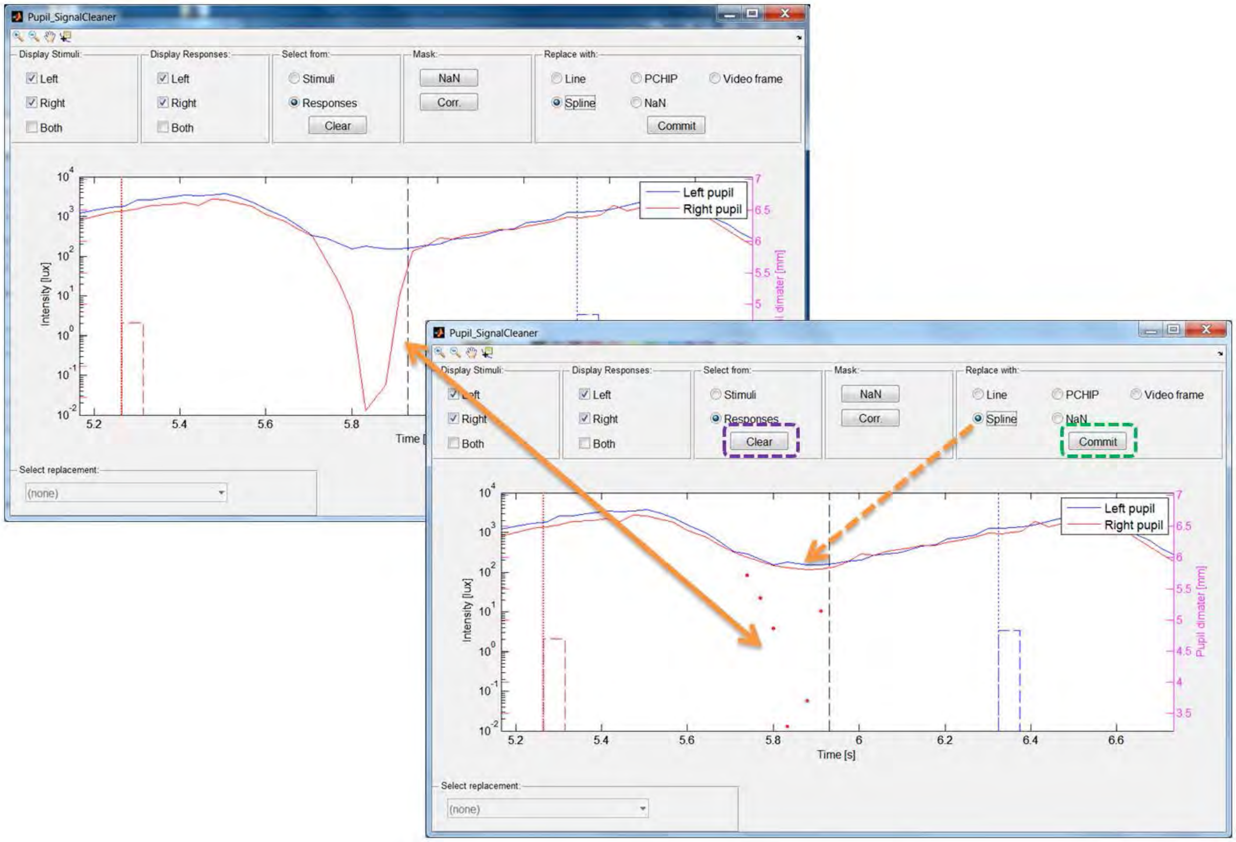

Figure 37. In case no synchronized video record is available, the expert user can use the main interface to select one or many points (shift + mouse click to select a region, or control + mouse click to toggle whether a single data point is to be included), and then apply different artifact removal algorithms, or mark the data to be completely ignored, i.e., replacing the selected pupil size data points with NaNs (not-a-number). In this example, the user has selected six (6) data points from the Right pupil tracing, and replaced it with a cubic spline interpolated values. The user can toggle through the radio buttons and inspect the quality of the different artifact removal procedures, and then has the option to either clear the selection (and select new points) by pressing the button marked with a purple box, or to commit the cleaned data points for further use by pressing the button marked with a green box.

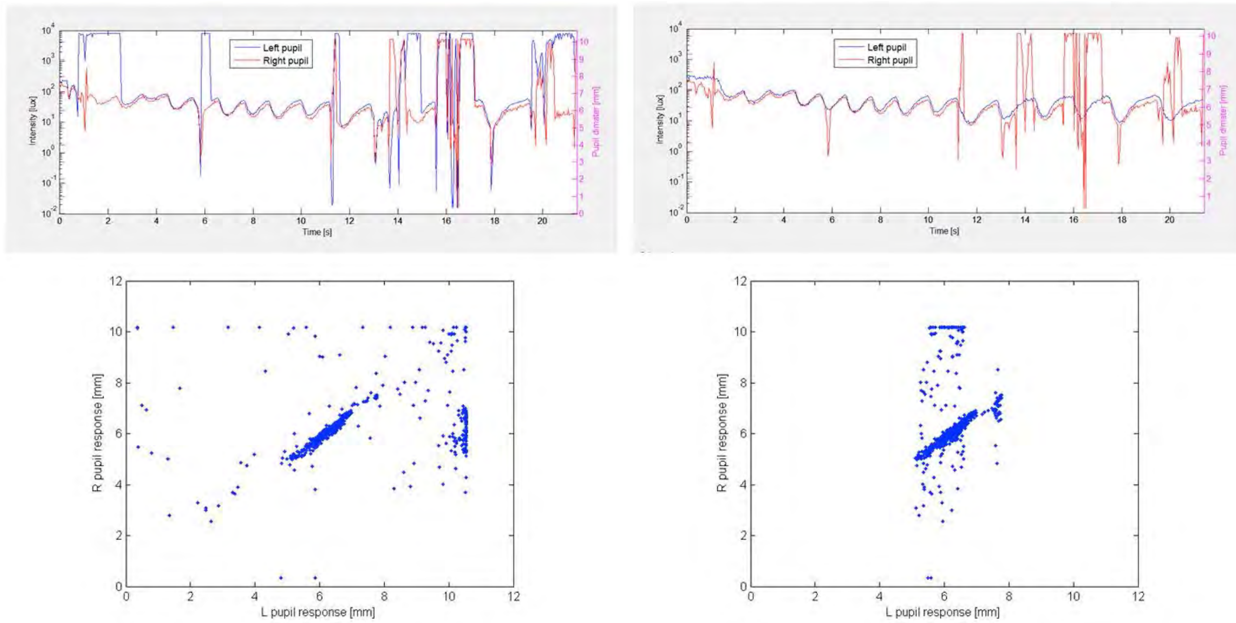

Figure 38. Correlation analysis can offer another potential approach to identify "bad" pupil size data points as part of automated data processing that we are in the process of implementing in the near future. In this example, the left hand scatter plot of Left versus Right pupil size data contains many outlier points, while the scatter plot on the right demonstrates the remaining spread of outliers due to "bad" Right pupil size data after the Left pupil tracing has been corrected through use of the video editing tool. Data points from normal bilateral pupil behavior are expected to cluster together in a tight band alongside a 1:1 straight line, with an intercept offset in case of anisocoria.

g) Pupil light reflex - Automated eyelid and artifact detection

Given the significant amount of time spent on data cleaning efforts of pupil data collected with our Neuroptics DP-2000 system due to eye blink artifacts, we have acquired a landmarking and tracking system from Componica in Year 5 to enhance and automate detection of eye features, such as eyelids, limbus, pupil shape, and artifact removal of Neuroptics data sets. We started to mark eyelid, limbus, and pupil features needed to train the tracking algorithm needed for automatic feature tracking (see Figure 39). The Componica tracking solution will allow us in future to analyze videos of the eye/pupil, recorded with different brands of pupillometers, and extract additional information, such as segmental pupil dynamics and eyelid movements, from the recorded video frames for clinical use.

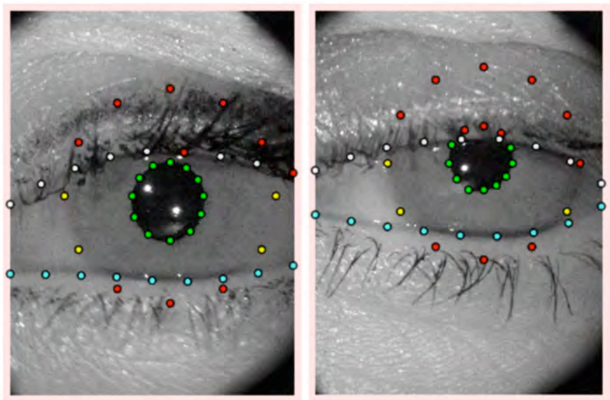

Figure 39. Examples of Neuroptics video frames with different eye features marked using the Componica EyeClipMarkerTM system. Eye features include the pupil (green dots), limbus (yellow dots), upper eyelid (white dots), and lower eyelid (cyan dots). Occluded feature points are marked in red, and are excluded when training the tracking algorithms.

h) <u>Novel clinical eye fixation/movement test during routine OCT tests</u>

In Year 4 we found that a patient suffering from unilateral anterior ischemic optic neuropathy (AION) had greater difficulty to stay fixated on a target during testing of the diseased eye compared to the fixation accuracy measured when either the normal eye or both eyes were used to fixate (see Figure 40). The measurements were made with our custom DynaScan-Smart Eye system. Building upon this finding, we developed a novel clinical tool in Year 5 that characterizes minute movements of the retina that can be used during routine ocular imaging as a means of diagnosing and monitoring treatment of various retinal and optic neuropathies. The pattern and magnitude of these micro-movements recorded during 30 seconds of routine ocular imaging turned out to be a sensitive and functional measure of neural networks controlling eye movements. Recording small movements of the retina is the most sensitive method available for characterizing micro-saccadic movements of the eye that cannot be captured by any other method. Utilizing this new method, the neural control of gaze stability could be assessed when a patient attempts the simple task of visually fixating on an internal target during routine optical coherence tomography (OCT) imaging of their retina.

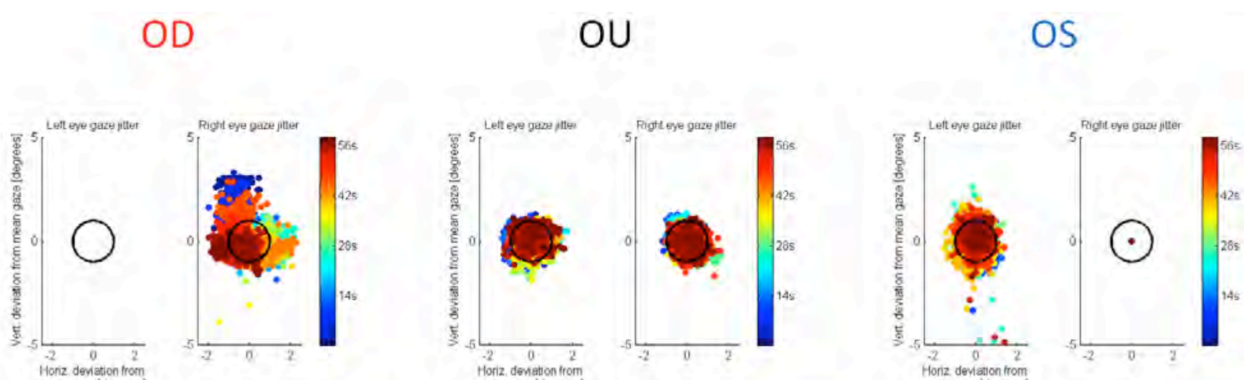

Figure 40. Abnormal distribution of eye fixation pattern in a patient suffering from unilateral anterior ischemic optic neuropathy (AION). The patient was instructed to gaze at a visual target for 60 seconds while the eye positions were tracked by a video eye tracking system. Three (3) testing conditions are shown, colored coded according to the time (seconds) from the onset of the start of the test. For example, the blue points are at the beginning of the 60 second test, the green points are at the middle and the red points are towards the end of the 60 seconds. Three (3) conditions are shown: 1) the right eye (OD) with AION and visual field loss is fixating on a

target during the test (left scatter plot), 2) both eyes are fixating (OU) on a visual target under binocular viewing conditions (center scatter plot), and 3) in the last condition, the normally sighted left eye (OS) is fixating on a visual target (right scatter plot). The black circle on each gaze scatter plot represents 1° offset with respect to the mean gaze vector during the test. Note that the patient has greater difficulty to stay fixated on the fixation target when viewing with the (diseased) right eye (OD condition). Based on the clustering of the gaze pattern of the right eye (i.e., patchy, but uniformly colored blobs of gaze points), it appears that the patient might have several preferred retinal fixation locations.

We propose that the inability of the eye to maintain constant fixation on a target is an important objective diagnostic sign that correlates with structural and functional changes, such as neurodegeneration, in the retina, optic nerve, and central nervous system (CNS) in patients. Structural and functional assessment of the visual pathways can serve as a global marker of disease burden. Structural changes in the retina and optic nerve are evident as thinning of the retinal ganglion cell and retinal nerve fiber layers on OCT. Reduction in contrast sensitivity is a functional indicator of vision that correlates with OCT findings. These changes in the retina may be asymptomatic in patients and may initially be evident as instability of gaze on a target. Furthermore, neurodegeneration may cause a subclinical derangement of nerve pathways in the brain that coordinate visual input with cognitive function. These central brain pathways are critical for maintaining stability of gaze and may provide an important biomarker for diagnosis and monitoring. The focus of this assessment of OCT-based retina movement is to assess structural and functional measures of visual pathway injury through a simple and elegant analysis of retinal movements during routine eye imaging. This will provide clinicians with a more powerful metric for early diagnosis, and for validating successful responses to disease-modifying or neuro-protective therapies.

Our premise is that quantifying the extent and distribution of micro-movements of the retina during attempted fixation on a target offers a novel, functional measure of the status of neural networks controlling eye movement that reflects disease activity. Fixation eye movements are controlled by a complex interplay between the afferent visual system (retina, optic nerve, optic radiations, and visual cortices) and efferent visual system (motor pathways controlling eye movements including prefrontal cortex, parietal lobe, cerebellum, and portions of the brainstem), which receive input from visual cortex. A simple and sensitive eye fixation test that can be affected by injury to any number of these networks provides a novel marker of disease activity.

The study of fixation eye movements has thus far been primarily limited to retinal disorders such as age-related macular degeneration or inherited retinal degenerations, where patients have a small hole in the central area of their vision. In such patients, it has been demonstrated that precise quantification of eye position during fixation on a target may reveal an underlying problem. Only a few studies have described derangement in fixation from central visual field loss from either optic nerve or CNS disease, and few studies have investigated fixation eye movements in patients with Alzheimer's Disease (AD) who lack visual symptoms. Other groups have showed an increase in the number of intrusion saccades during fixation over 18 months of follow up in AD patients that did not increase in age-matched controls. The worsening of fixation stability correlated with change in cognitive and memory testing over time, indicating that fixation stability may be useful in monitoring progression of AD in individual patients. A recent publication showed that oblique microsaccades were more common in AD and other forms of dementia (Kapoula et al., 2014).

Since fixational eye movements, including microsaccades, are by definition very small (less than 2 degrees) and are involuntary, they are best detected using retinal imaging devices that precisely track retinal landmarks, such as the confocal scanning laser ophthalmoscope (cSLO). OCT platforms utilize cSLO based eye tracking of retinal landmarks for scan stabilization and patients fixate on an internal target during image acquisition, so the proposed retina tracking is a simple by-product of the test. It be easily implemented at vision and neurology centers using a standard OCT device, while retinal structural damage is assessed simultaneously. However, the slow sampling rate (<10Hz) of cSLO-based eye tracking hampers its utility to adequately monitor microsaccadic eye movements, which requires significantly higher sampling rates (>200Hz).

In Year 5, we implemented computational methods to determine fixation stability from eye tracking data obtained with the Spectralis OCT and developed software for extraction of high-resolution eye position data from cSLO video recordings of the retina. Fixation data was collected and analyzed in patients with central vision loss due to optic neuropathy and in patients with MS to demonstrate that normal fixation is altered by both optic nerve and CNS disease. We also measured the fixation eye movements of one patient with optic neuritis through the course of recovery to illustrate that improvement in fixation eye movements can parallel improvement in visual function, as described below.

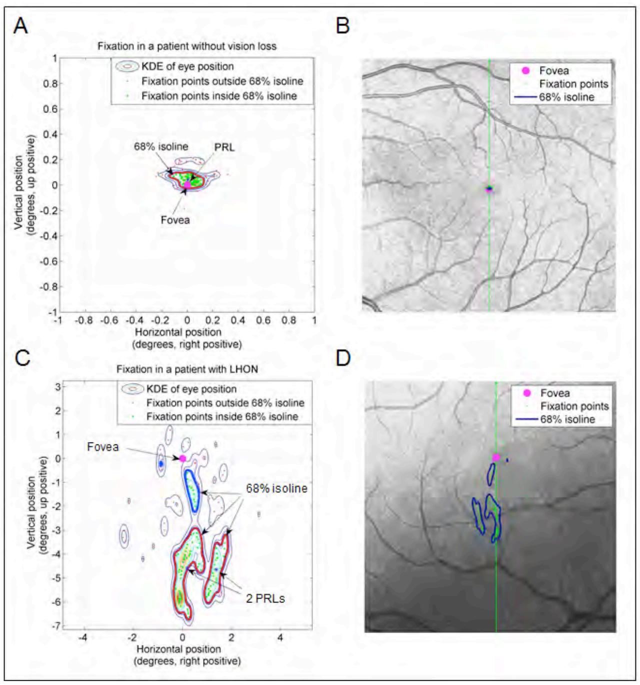

Figure 41. Comparison of fixation stability in a patient with normal vision (top plot) and a patient with Leber hereditary optic neuropathy (LHON) – bottom plot. A) KDE of left eye position in a patient with normal vision shows stable fixation within a small area (0.023 deg2) enclosed by the 68% isoline (red contour). B) Overlay of the fixation data on the retina shows a single PRL located at the fovea (magenta dot in SLO image, top right). C) Fixation of a patient with LHON is unstable. The area enclosed by the 68% isoline measures 4.1 deg^2, and the patient has 2 eccentric PRLs (outlined by the red contours). D) Overlay of fixation data onto the retina demonstrates fixation eccentric from the fovea (magenta dot in SLO image, bottom right). Note the difference in the scales on the x-axis between A) and C).

Preliminary testing of fixation in patients with optic neuropathy suggested that optic neuropathy causes derangements in fixation stability and also can result in eccentric fixation away from the fovea when a hole in the center of vision (scotoma) exists. Subsequently, 29 patients with central visual field loss from optic neuropathy (20 unilateral, 9 bilateral) and 11 normal subjects underwent OCT scanning with eye tracking (Spectralis, Heidelberg Engineering). Subjects fixated on an internal central blue target, and eye position was recorded for 30 seconds before acquisition of each OCT volume scan. The probability density function of fixation points on the retina with respect to the anatomic fovea was quantified using Kernel Density Estimation (KDE). Fixation stability was calculated as the total area enclosed by the 68% isoline of the KDE of retina position, and preferred retinal loci of fixation were judged as distinct retinal areas enclosed by the 68% isoline and including at least 10% of the fixation points. Each patient underwent ETDRS visual acuity testing and perimetry (Goldmann or Humphrey 24-2 SITA-standard) to confirm central visual field loss. Results indicate that fixation instability and eccentricity are increased in eyes with optic neuropathy (see Figure 42), and that fixation instability and eccentricity are increased in affected eyes compared with their paired, unaffected eye (see Figure 43). Based on operator receiver curve (ROC) analysis, we have found that fixation stability and eccentricity are moderately sensitive and specific for distinguishing optic neuropathy eyes from unaffected eyes (see Figure 44), and that fixation stability and eccentricity are highly specific and highly sensitive for diagnosing a central scotoma (see Figure 45).

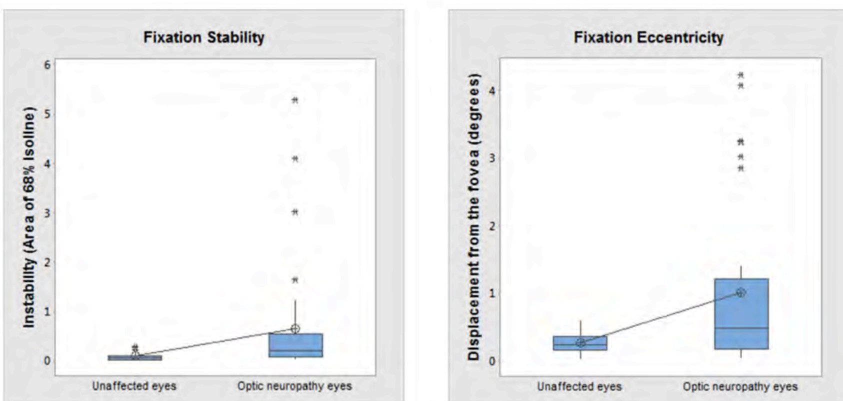

Figure 42. Fixation instability and eccentricity are increased in eyes with optic neuropathy.

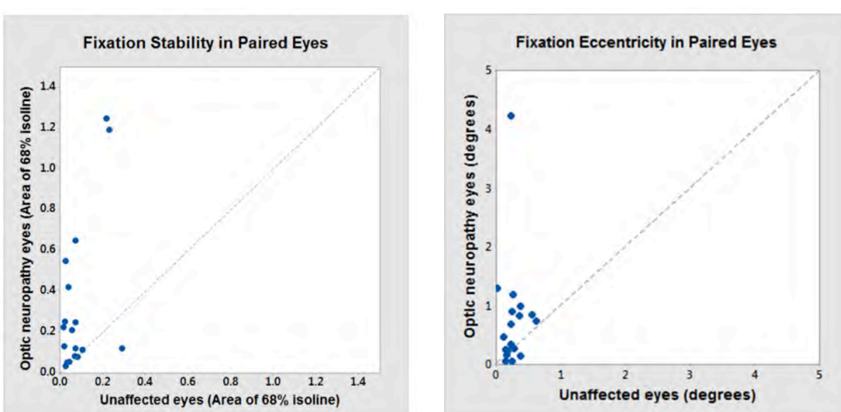

Figure 43. Fixation instability and eccentricity are increased in affected eyes compared with their paired, unaffected eye.

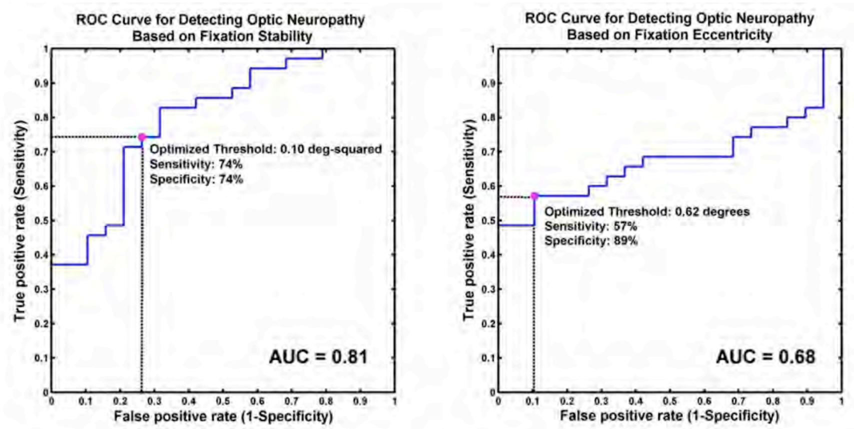

Figure 44. Fixation stability and eccentricity are moderately sensitive and specific for distinguishing optic neuropathy eyes from unaffected eyes.

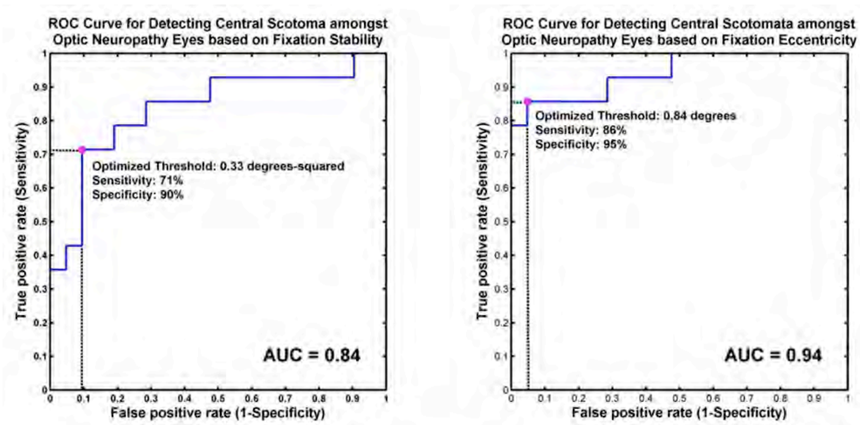

Figure 45. Fixation stability and eccentricity are highly specific and highly sensitive for diagnosing a central scotoma.

The effect of multiple sclerosis (MS) on fixation stability was also further assessed by studying the fixation pattern of patients with MS without optic neuropathy. Twenty six (26) patients with MS were tested, as well as 20 normal subjects. MS patients without prior optic neuritis showed a significant instability of fixation compared to age-matched normal eyes (Mann-Whitney U test, p=0.043) (see Figure 46). This result indicates that CNS disease (in this case multiple sclerosis), in the absence of optic neuropathy, may be associated with abnormal patterns of fixation. There was no correlation of fixation stability with average ganglion cell layer (GCL) thickness.

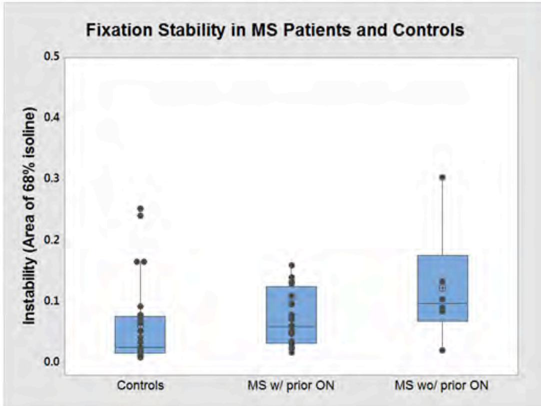

Mann-Whitney	N	Median
Controls	20	0.026 deg^2
MS wo/ prior ON	26	0.061 deg^2
P-value = 0.043		

Figure 46. Results showing an increase in fixation instability in patients with MS and no prior history of optic neuritis (right box plot), compared to normal control eyes (left box plot). Fixation data from 7 MS patients with prior optic neuritis that recovered suggested a trend toward further increase in fixation instability (center box plot).

In an effort to overcome the low sampling rate of cSLO-based eye tracking, we also developed an image analysis approach in Year 5 to extract high-resolution eye position data from raw cSLO video recordings of the retina. Given that each SLO video frame is obtained by scanning the retina horizontally line by line, from top to bottom, we were able to take advantage of the SLO's rolling shutter operation to increase the effective sampling rate of the resultant eye tracking data many fold. As part of our image analysis approach, we have implemented both rigid (see Figure 47) and non-rigid (see Figure 48) models for teasing apart eye movements during each interval taken by the SLO to produce each video frame. The ability of a non-rigid model to estimate movement effects during horizontal line scans constitutes a significant advantage over a rigid model. We are now able to track microsaccades and nystagmus at sampling rates (see Figure 49), allowing us to quantify microsaccadic eye movement and nystagmus parameters accurately.

Figure 47. Our rigid image registration method derives eye position by correlating equally-spaced horizontal strips from each cSLO video frame with the reference image to derive x and y shift of the retina.

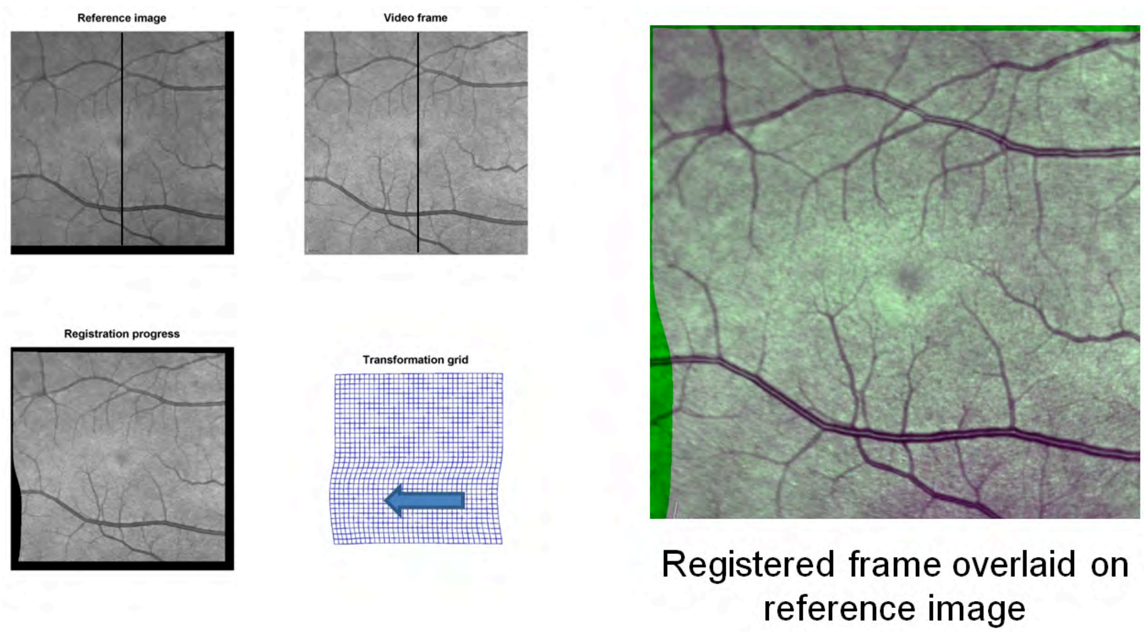

Figure 48. Our non-rigid registration of SLO video uses the local shift in the transformation grid calculated for each video frame and the reference image to derive eye position changes due to saccades, microsaccades, nystagmus, etc. at arbitrary high frame rates.

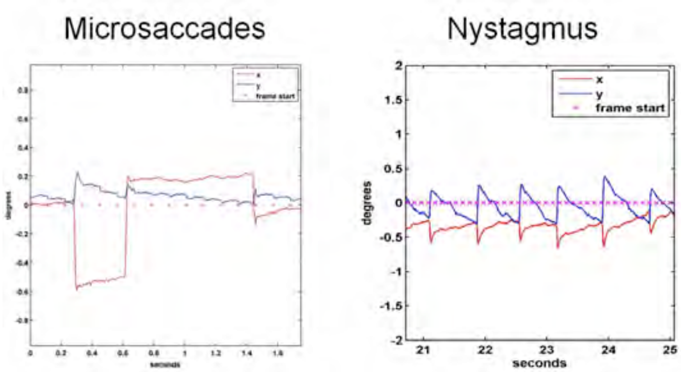

Figure 49. Different eye movement types recorded using SLO video and non-rigid image registration at an effective frame rate of 344Hz.

i) <u>Fast, segmental checkerboard test for recording evoked potentials</u>

In order to design the temporal characteristics of the VEP stimulus sequence to ensure successful extraction of responses from simultaneous multi-focal and overlapping stimuli, we have considered the assumptions and implications of numerous methodologies referenced in literature. One of the most well-known methods for functional testing of sensory and other neural pathways is the evoked response potential (ERP) or transient response (TR) methodology. ERPs (or TRs) require the use of time-domain conventional averaging to improve poor signal-to-noise ratio, commonly due to artifact contamination, which results in longer acquisition periods to record additional responses. In spite of its advantages, conventional averaging has a severe limitation: If the response to each stimulus is not complete prior to the presentation of the next stimulus, it results in overlapping responses and the difficulty to separate responses into their corresponding components. As a consequence of this limitation, the stimulation rate for EP (or TR) paradigms is limited by the duration of the recorded physiological response. In an effort to circumvent this time

duration limitation, faster stimulation rates can be achieved through the use of steady-state responses (SSRs). SSR acquisition uses the same averaging techniques with a constant stimulus rate and no jitter. Under these conditions the responses overlap each other, resulting in a complex waveform that is instead analyzed in the frequency domain by measuring spectral peaks. In a steady-state condition, the characteristics of the overlapping responses depend on the sensitivity of the responses at the stimulation rate. Also, critical information provided by the waveform morphology and components are lost due to the overlapping responses and the periodic nature of the stimulus sequence. Note that our frequency modulated checkerboard stimulus paradigm is an example of the SSR technique.

A second technique to circumvent the limitations imposed by conventional averaging is the use of specially designed stimulus sequences called maximum length sequences (MLS), which allows one to separate an individual response from overlapping responses. Other researchers have proofed the validity and reliability of the MLS method and the existence of other similar sequences such as the Legendre sequences. These studies also showed that the response generation was likely to be the same as in conventional averaging. However, a major limitation of the MLS method is rooted in its limited choice of sequences. These sequences cover a wide range of rates with a high degree of jitter. Since ERP or TR adaptation effects differ widely in different neurosensory systems, the interpretation of MLS generated responses could be difficult.

To summarize the findings from literature, the ERP (or TR) method cannot be used for fast stimulus rates due to overlap of responses, and the SSR method cannot be used for analyzing the characteristics of the individual responses due to overlap. The MLS and other similar methods solve the problem of component decomposition only for a few special stimulus sequences. These special sequences have a wide range of jitter, which limits the usefulness of the method in different applications. The temporal design of our VEP stimulus sequence, as well as the analysis method needed to extract the responses from simultaneous multi-focal and overlapping stimuli, draw heavily on principles used in the field of functional magnetic resonance imaging (fMRI). Given the long duration of the hemodynamic response function (HRF) – blood oxygenation changes occur up to 15s following a stimulus – and significant costs associated with operating MR equipment, fMRI researchers have adapted the generalized least squares (GLS) method to deconvolve overlapping stimulus responses, which allows them to design shortened stimulus sequences which are not boring, while minimizing anticipation and habituation. The latter benefit is also a result of the need to use a wideband, noise-like stimulus onset sequence for estimation of the HRF wave shape. The main assumption of the GLS model implies that the individual response to each stimulus is independent of other stimuli and responses, and that the measured overall response is a superposition or arithmetic sum of the individual overlapping responses.

Similar to the fMRI analytic model, our VEP model is based on assembling a design matrix that is populated based on the exact onset times of the different multi-focal stimuli. We incorporate jitter to the interval between each stimulus to produce a semi-random onset sequence. The model also allows us to set a range of temporal frequencies to be used when the GLS is solved by incorporating a set of basis functions. Based on the spectral decomposition of the ISCEV VEP response templates, we have a priori knowledge to constrain the model to be only sensitive to frequencies in the 0–

30Hz range and not to be confused by significant 60Hz line noise components or a substantial portion of EMG artifacts in the measured EEG. If a set of basis functions is not used, one could potentially obtain a similar effect by applying a digital filter (band pass or low pass, etc.) to the raw EEG measurements for removing 60Hz line noise, etc. before solving the model. Furthermore, it is crucial to use exact onset times, which are calculated based on the timestamps of codes broadcasted via the parallel port of the stimulus presentation computer, as well as the measurement of the time offset between sending these codes and the analog output of a photodiode facing the TV or monitor being used to present the stimuli. We have extensively validated the solution of the GLS model in Matlab through the use of synthetic data, and optimized the solution of the GLS model through the use of sparse matrix computations, as well as employing the graphics card (GPU) for analytical computations. In some cases, the speedup is almost 100x compared to solving the linear system of equations on the central processing unit (CPU) of the computer. This capability enables us to continuously compute the VEP responses during data acquisition, which makes it possible to terminate a stimulus sequence early if the VEP responses are of sufficient quality. In future, gaze and eyelid opening measurements acquired simultaneously from the Smart Eye head and eye tracker can be used to prune data points from the raw EEG in order to exclude time intervals during which the subject has not been looking at the fixation target (red circle) or blinked/closed his/her eyes (see Figure 50).

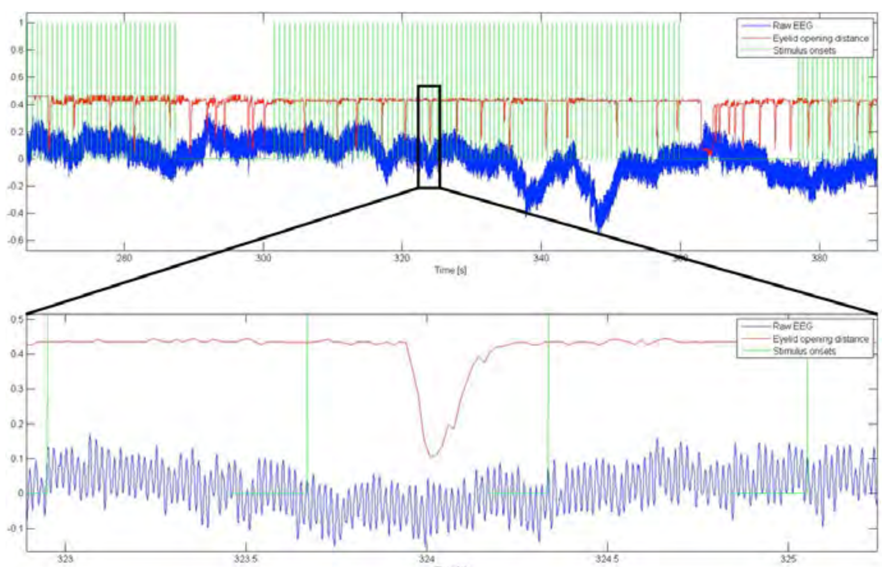

Figure 50. Example of a raw EEG signal from an occipital scalp location (blue time series) during a 60s pattern onset/offset stimulus sequence (from t=300s to t=360s in the top figure, and zoomed in at t~324s in the bottom figure), consisting of about 84 stimulus presentations. The red time series represents the size of the subject's left and right combined eyelid opening (i.e., maximum distance between the upper and lower eyelids), while each vertical portion of the green time series represents the exact time of each stimulus onset, based on the analog output from the photo diode facing the TV.

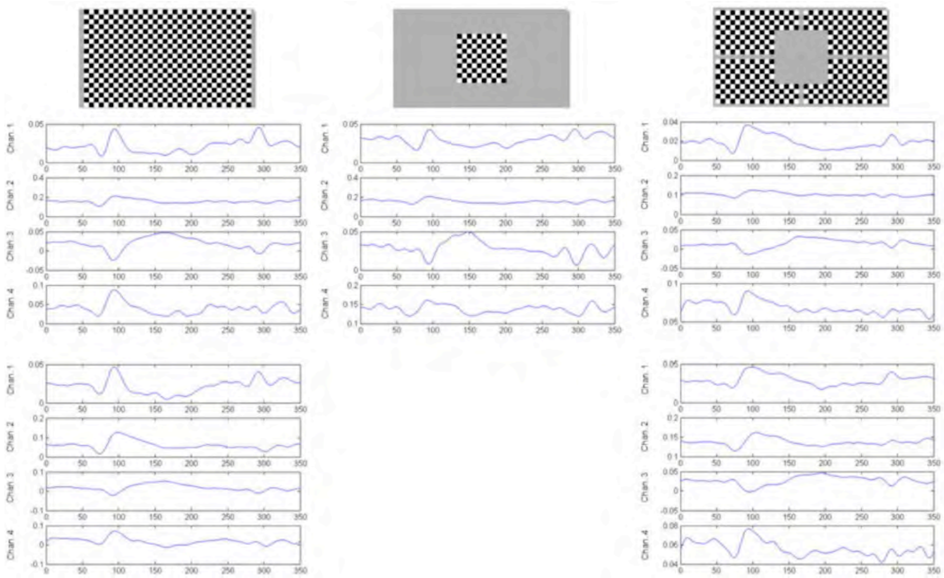

Figure 51. 350ms duration length VEP responses extracted for four (4) EEG channels for full-field (left column), center-only (middle column), and peripheral-only (right column) stimulus sequences consisting of ~84 stimulus presentations (over 60s) to test the reproducibility of the extracted VEP responses with our GLS-based analysis method. The full field and peripheral-only sequences were presented twice in two different stimulus runs (top vs. bottom half), and the wave forms are qualitatively highly correlated when comparing the two runs within each stimulus sequence type.

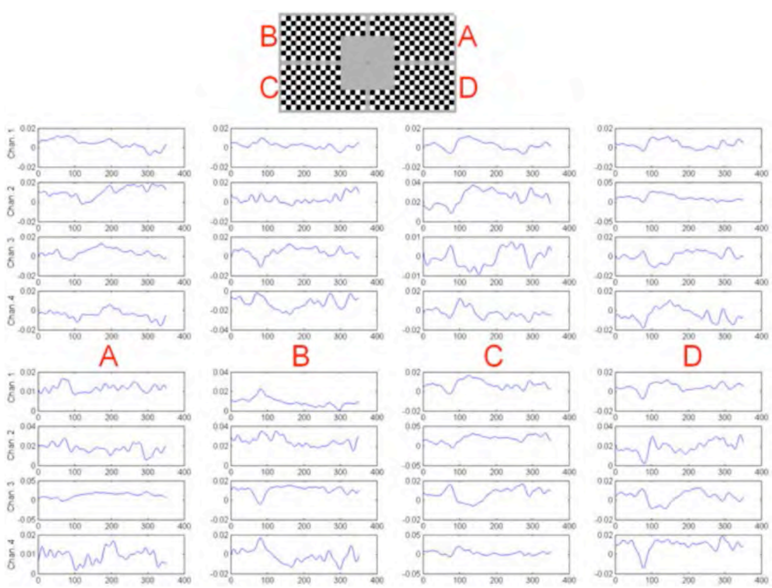

Figure 52. 350ms duration length VEP responses extracted for four (4) EEG channels for the peripheral-only stimulus sequence consisting of ~84 simultaneous and overlapping presentations at each of the four (4) peripheral locations/quadrants (over 60s) to test the reproducibility of the extracted VEP responses with our GLS-based analysis method. The sequence was presented twice on two separate test runs (top vs. bottom half), and the wave forms are qualitatively highly correlated when comparing the two runs within each stimulus location (i.e., column-wise).

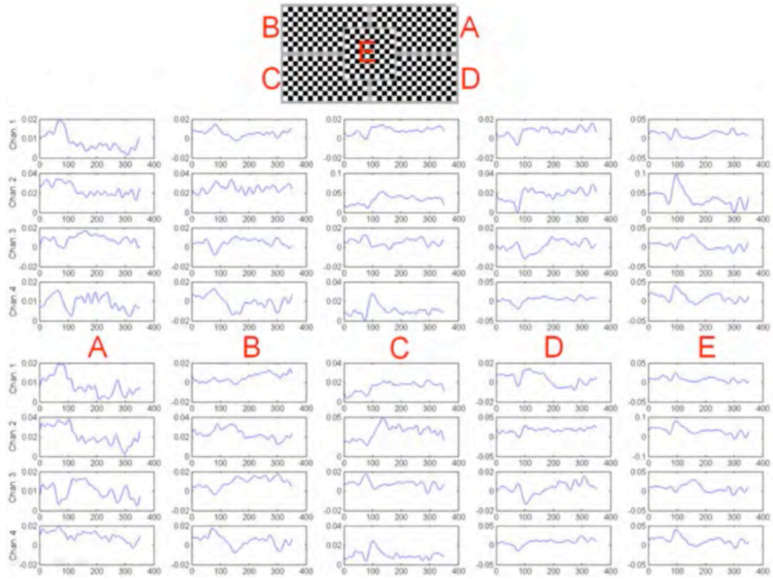

Figure 53. 350ms duration length VEP responses extracted for four (4) EEG channels for the central-peripheral stimulus sequence consisting of ~84 simultaneous and overlapping presentations at each of the five (5) stimulus locations (over 60s) to test the reproducibility of the extracted VEP responses with our GLS-based analysis method. The sequence was presented twice on two separate test runs (top vs. bottom half), and the wave forms are qualitatively highly correlated when comparing the two runs within each stimulus location (i.e., column-wise). The responses for the center stimulus location (column E) are qualitatively similar to the responses for the center-only stimulus sequence shown in an earlier figure.

In Year 3, we compared the m-sequence model to our proposed design matrix-based model in terms of statistical metrics in order to shed more light on the strengths and weaknesses of both models in terms of our scenarios of use. Although m-sequences are not part of the ISCEV standard for multi-focal VEP studies, it forms the basis of the ISCEV multi-focal ERG standard, and therefore compelled us to investigate the use of the MLS method in more detail. It is in fact possible to use a design matrix to model (capture) the stimulus sequences used in an MLS experiment (i.e., m-sequences), which allows for a direct comparison of the analysis results between the MLS method and the least squares solution of the design matrix-based method on the same recorded or simulated data set.

As mentioned earlier, a major limitation of the MLS method is rooted in its limited choice of sequences. Each sequence out of an MLS set is constrained to be approximately orthogonal with respect to the other sequences from the same set, imposing a wide range of stimulation rates with a high degree of stimulus onset jitter on each sequence. On the other hand, a design matrix offers flexibility in terms of the stimulation rate, semi-random onset jitter, and other stimulation sequence parameters that can be set for each individual stimulus location. It is also important to note that the occurrence of missing or corrupted data segments poses a significant problem for the MLS method, while it is trivial to remove time points which are deemed corrupted due to noise, subject inattention, etc. from a design matrix.

In general, a broad-band stimulation rate (e.g., an m-sequence) favors efficient waveform morphology estimation, while a narrow-band stimulation rate allows for a more accurate estimate of the overall response amplitude, and therefore greater detection power. For the case of semi-random onset sequences, waveform estimation and detection power are balanced more evenly. A

significant strength of using a design matrix revolves around the ability to alter the balance of the model to focus on efficient estimation of the unknown waveform morphology versus focusing the model on the accurate detection of responses in the presence of noise. This trade-off can be adjusted for each response by adding additional constraints to the model in the form of a set of basis functions to describe each response waveform in terms of smoothness, frequency spectrum, etc. For example, it is possible to use a set of sinusoids at relatively low frequency if the expected response waveform is smooth and lack higher frequency components.

From our literature study, we have found a few model evaluation guidelines, which include both statistical and graphical techniques (e.g., Moriasi et al., 2007). Quantitative statistics include standard regression, dimensionless, and error index metrics. Standard regression statistics determine the strength of the linear relationship between simulated and measured data, and include Pearson's correlation coefficient (r) and the coefficient of determination (R^2). The correlation coefficient r, ranging from −1.0 to 1.0, indicates the degree of linear relationship between observed and simulated data. If $r = 0.0$, no linear relationship exists, while for $r = 1.0$ or −1.0, a perfect positive or negative linear relationship exists. Similarly, R^2 describes the proportion of the variance in the data explained by the model and ranges from 0.0 to1.0. However, although widely used for model evaluation, these statistics are oversensitive to high extreme values (outliers) and insensitive to additive and proportional differences between model predictions and measured data.

Dimensionless techniques constitute a second class of quantitative statistics, and provide for relative model evaluation assessment. The Nash-Sutcliffe efficiency (NSE) is a normalized statistic that determines the relative magnitude of the residual variance ("noise") compared to the observed data variance ("information") (Nash and Sutcliffe, 1970). The NSE metric indicates how well the plot of observed (i.e., underlying "ground truth") data *versus* modeled data fits the 1:1 line, and is computed as:

$$NSE = 1 - \left[\frac{\sum_n \left(Y_i^{obs} - Y_i^{model}\right)^2}{\sum_n \left(Y_i^{obs} - \overline{Y}\right)^2} \right]$$

where $\overline{Y}$ is the mean of the observed ("ground truth") data, and n is the total number of observations. The NSE metric ranges from $-\infty$ to 1.0, with $NSE = 1.0$ being the optimal value. Values between 0.0 and 1.0 are generally viewed as acceptable levels of performance, whereas values below 0.0 indicate that the mean observed value is a better predictor than the modeled values, and signify unacceptable performance of the model.

A third class of quantitative statistics consists of error indices to quantify the deviation between the modeled and observed underlying data in the units of the data of interest. The trade-off between bias and residual variance has to be considered, as recommended by Boyle et al. (2000). Bias measures the average tendency of the modeled data to be larger or smaller than their observed counterparts (Gupta et al., 1999). Residual variance is the difference between the measured and

simulated values, often estimated by the residual mean square error (*MSE*) or root mean square error (*RMSE*). Optimizing *RMSE* during model calibration may give small error variance but at the expense of significant model bias.

Percent bias ($PBIAS$) is computed as:

$$PBIAS = \frac{\sum_n \left(Y_i^{obs} - Y_i^{model}\right) * 100}{\sum_n Y_i^{obs}}$$

The optimal value of $PBIAS$ is 0.0, with low-magnitude values indicating accurate model simulation. Positive values indicate model underestimation bias, and negative values indicate model overestimation bias.

RMSE-observations standard deviation ratio (RSR) is one of the commonly used error index statistics in hydrologic modeling (e.g., Singh et al., 2004). The RSR metric standardizes *RMSE* values using the observations standard deviation, and is calculated as the ratio of the *RMSE* and standard deviation of the observed data:

$$RSR = \frac{RMSE}{STDEV_{obs}} = \frac{\sqrt{\sum_n \left(Y_i^{obs} - Y_i^{model}\right)^2}}{\sqrt{\sum_n \left(Y_i^{obs} - \overline{Y}\right)^2}}$$

The range of RSR extends from the optimal value of 0.0, which indicates zero RMSE or residual variation and therefore perfect model fit, to a large positive value. The lower the *RMSE* value, the lower the RSR value, and the better the model performance.

We have implemented a software-based test bed to evaluate the impact of various parameters on the efficiency of different models for extracting the waveform morphology and activation level of multiple responses. The test bed allows us to specify the number of response areas, individual response waveforms, individual stimulus sequences, experiment duration, the nature of basis functions to be used with the design matrix method, as well as additive noise profiles. Based on these parameters, simulated data sets were created and analyzed with the MLS method and the design matrix method afterwards. Model evaluation statistics can then be computed to compare the efficiency of each model to extract the underlying "ground truth" responses in the presence of noise, as well as the effect of other model assumptions on the overall outcome. The test bed can be used to fine tune the stimulus sequences for the VEP sequences in order to further optimize the bias *versus* error variance trade-off, while trying to make each test protocol as short as possible and maximize the robustness of the methodology against the impact of corrupted data and subject inattention, etc.

For the figures following (see Figure 54, Figure 55, and Figure 56), we have set up our test bed to evaluate the effect of different levels of noise, as well as different basis function sets on the MLS and design matrix methods for 61 individual stimulation locations (and therefore 61 different responses). The "ground truth" response waveforms were chosen as a windowed sinusoid with a

central frequency proportional to the index number of the response (i.e., response #1 had the lowest frequency and response #61 had the highest frequency), while the amplitude of the waveform hills were increased by 2.5x with respect to the valleys to create a non-zero mean value. The sampling rate was set at 1,000Hz, and the minimum inter stimulus interval (ISI, or base period in terms of the MLS method) was 50ms. Two stimulus onset sequence protocols were used: the first set was based on standard m-sequences, and the second set was created by allowing the ISI to vary randomly in a constrained interval of 50 to 150ms. The parameter selection of the latter ensured that both protocols were similar in terms of the mean number of stimulus presentations for each stimulation location. Additive noise values were modeled as normally-distributed with zero mean.

Based on our simulation results, the design matrix method offers us a more efficient way to analyze multi-response data compared to the MLS method, while the m-sequence stimulus onset protocol tends to produce lower bias at the expense of higher error variance when compared to the constrained (pseudo-) random stimulus onset protocol in case of the design matrix analysis method.

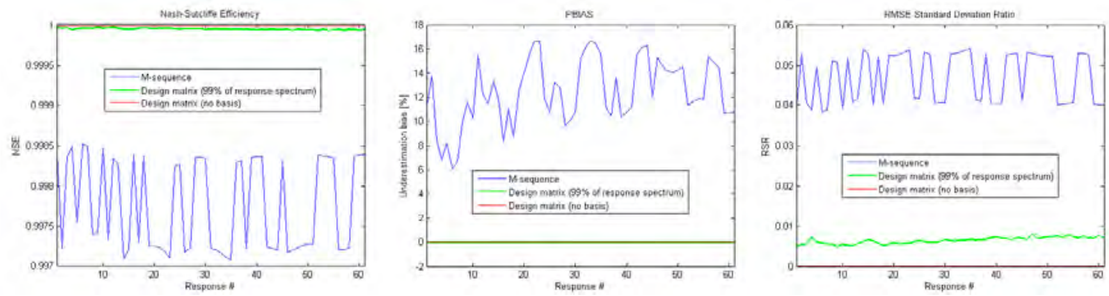

Figure 54. Noiseless case: With no additive noise, the design matrix analysis method outperforms the MLS analysis method in terms of bias (*PBIAS* metric), as well as error variance (*NSE* and *RSR* metrics). As expected, the use of a constrained basis for the design matrix method leads to increased bias and error variance. The same m-sequence stimulus onset protocol was used for both MLS and design matrix analysis methods.

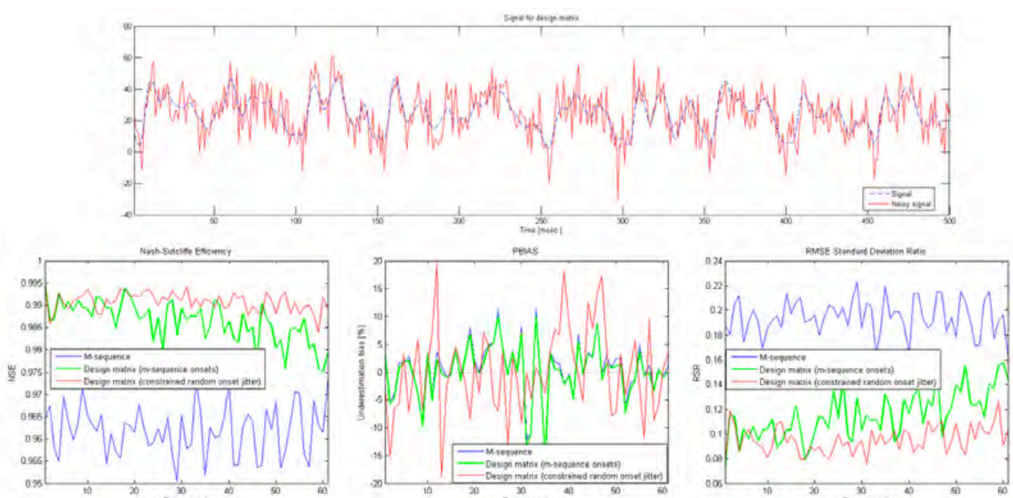

Figure 55. Simulation results with the standard deviation of the additive noise set to 10 units. The top graph shows the combined waveform of 61 responses, activated by the constrained (pseudo-) random stimulus onset protocol, with and without noise over a representative 0.5s interval. The 3 bottom graphs demonstrate the improved analysis efficiency of the design matrix method (green line) in comparison with the MLS method (blue line) for the case of the m-sequence stimulus onset protocol. The m-sequence stimulus onset protocol (red line)

tends to produce lower bias at the expense of higher error variance when compared to the constrained (pseudo-) random stimulus onset protocol in case of the design matrix analysis method.

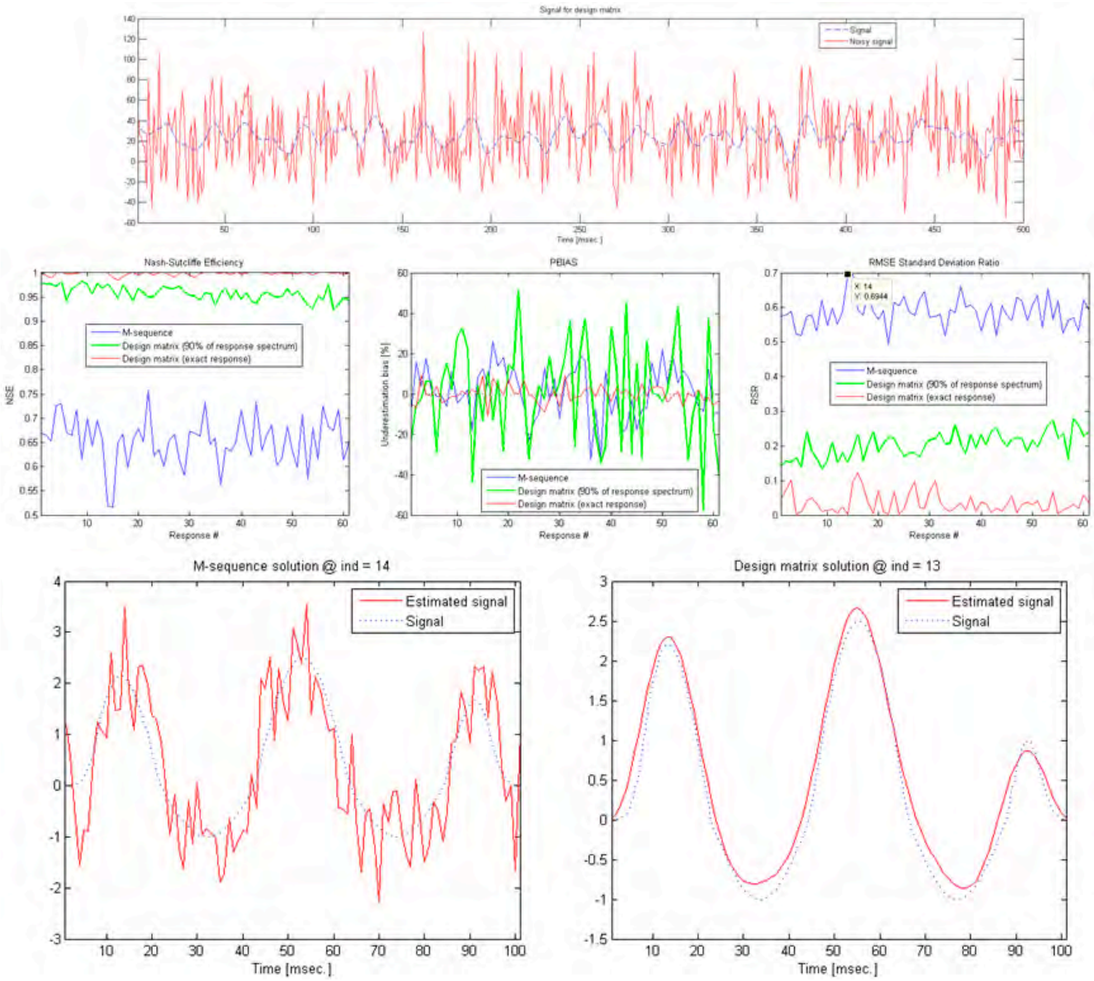

Figure 56. Simulation results with the standard deviation of the additive noise set to 30 units. The top graph shows the combined waveform of 61 responses, activated by the constrained (pseudo-) random stimulus onset protocol, with and without noise over a representative 0.5s interval. The 3 graphs in the middle demonstrate the lower error variance but higher bias tendencies of the design matrix method (green line) with the constrained (pseudo-) random stimulus onset protocol in comparison with the MLS method (blue line). Also shown is the special case for which accurate waveform morphology information is available, in which case the design matrix method (red line) can efficiently extract the activation amplitude of the responses in the presence of overwhelming noise. The 2 bottom graphs show the "ground truth" *versus* modeled response waveforms for the MLS analysis method (left) and the design matrix analysis method (right) for representative responses with larger deviations from the "ground truth" data.

KEY RESEARCH ACCOMPLISHMENTS

Year 1

- Evaluation of hand held pupillometer and facilitation of new chromatic pupil testing platform to be delivered by Neuroptics in Year 2
- Prototype of dry electrode system evaluated and delivery expected in first part of Year 2
- Implementation and evaluation of Smart Eye head and ocular tracking system
- Software architecture development completed for stimulus presentation, data synchronization, and analysis
- Integration of an entire ocular testing echo---system completed that integrates visual stimulation, evoked potential recording (VEP, PERG, EMG and skin conductance), head tracking, eye tracking, and pupil responses with a unified data analysis system
- Key literature reviewed and continues as an ongoing updated process

Year 2

- Evaluation of and implementation of new desktop, binocular pupillometer with new chromatic pupil testing platform and anticipated delivery of fully portable binocular head worn unit by Neuroptics in Year 3
- Prototype dry electrode wireless system delivered in Year 2 and is currently being implemented with software interface
- Visual stimulus presentation hardware system and software platform developed for delivery of stimuli and on---line analysis of visual evoked responses from visual cortex (regional visual field stimulation and analysis), eye movement following of vanishing optotypes, and simultaneous pupil responses.

Year 3

- Development of a completely objective test protocol and associated data analysis routines to derive metrics that correlate with clinical diagnoses of afferent and efferent pathway pathologies based on the pupil light reflex. This test protocol consists of 8 white light impulses presented sequentially to each eye across a range 29 of intensities (1-400 lux), and is less than 22 seconds in duration. The Pearson correlation coefficient (*r*) between the continuous RAPD metric derived from this test protocol and clinical measurements taken from the same subjects is 0.86.
- Implementation and testing of a multi-functional user interface to allow an expert user to quickly and efficiently perform manual artifact detection and removal, using both video and pupil tracings, in cleaning pupil light reflex (PLR) data. Clean data are needed to populate our PLR database, and to provide a sufficient number of instances of paired artifact and cleaned data segments to train future automated artifact detection/removal algorithms to minimize manual operations.

- Comparison of our in-house design matrix method for visually-evoked potential (VEP) stimuli with the well-known maximum length sequences (MLS or m-sequences) method based on simulations and various statistical methods. We have shown that the design matrix method offers us a more efficient way to analyze multi-response data compared to the MLS method, while the m-sequence stimulus onset protocol tends to produce lower bias at the expense of higher error variance when compared to the constrained (pseudo-) random stimulus onset protocol used as part of the design matrix analysis method.

Year 4

- In terms of the red-blue pupil light reflex test, we have shown that the resulting responses measured with our custom DynaScan-Smart Eye system correlate well with results obtained with the Neuroptics DP-2000 system. Specifically, for both test platforms, the % pupil contraction value sustained at 6s after a bright blue stimulus is reduced for the diseased eyes in comparison to the healthy eyes, while the pupil response to the bright red stimulus has dissipated by 6s.
- By comparing the pupil light reflex before and after radiation treatment of a patient suffering nerve sheath meningioma compressing the optic nerve, we were able to show the utility of the pupil responses to red and blue light for monitoring treatment. The recovery of the pupil light reflex in the diseased eye following treatment correlated with improvement in visual acuity, as measured with a standard clinical test.
- In terms of evoked responses, we have shown that VEP amplitudes in response to our design matrix stimulation method presented on our custom DynaScan-Smart Eye system are significantly attenuated when a diseased eye is stimulated when compared against the VEP responses from stimulation of the healthy eye or of both eyes simultaneously.
- We have found that a patient has greater difficulty to stay fixated on a fixation target during stimulation of a diseased eye.

Year 5

- We developed a pupil light reflex test for detecting optic neuropathy independent of the fellow eye as a method for detecting retinal and optic nerve dysfunction and compared it to the clinical gold standard of visual input testing using subjective determination of visual field sensitivity. We found that the transient pupil contraction to a 1 second bright blue light gave the highest correlation with visual field sensitivity (correlation coefficient r=0.85) compared to the sustained pupil contraction (correlation coefficient r=0.52). The transient pupil contraction also provided the greatest separation between normal and abnormal eyes compared to the sustained pupil contraction
- We developed a novel clinical tool that characterizes minute movements of the retina that can be used during routine ocular OCT imaging as a means of diagnosing and monitoring treatment of various retinal and optic neuropathies. The pattern and magnitude of these micro-movements recorded during 30 seconds of routine ocular imaging are used to evaluate the fixation stability. Testing of fixation in patients with optic neuropathy suggest that optic neuropathy causes derangements in fixation stability and also can result in eccentric fixation

away from the fovea when a hole in the center of vision (scotoma) exists. Results indicate that fixation instability and eccentricity are increased in eyes with optic neuropathy, and that fixation instability and eccentricity are increased in affected eyes compared with their paired, unaffected eye. Based on operator receiver curve (ROC) analysis, we have found that fixation stability and eccentricity are moderately sensitive and specific for distinguishing optic neuropathy eyes from unaffected eyes, and that fixation stability and eccentricity are highly specific and highly sensitive for diagnosing a central scotoma.

- The effect of multiple sclerosis (MS) on fixation stability was assessed by studying the fixation pattern of patients with MS without optic neuropathy. MS patients without prior optic neuritis showed a significant instability of fixation compared to age-matched normal eyes (Mann-Whitney U test, p=0.043). This result indicates that CNS disease (in this case multiple sclerosis), in the absence of optic neuropathy, may be associated with abnormal patterns of fixation. There was no correlation of fixation stability with average ganglion cell layer (GCL) thickness.
- To overcome the low sampling rate of cSLO-based eye tracking, we developed an image analysis approach to extract high-resolution eye position data from raw cSLO video recordings of the retina. We are now able to track microsaccades and nystagmus at sampling rates, allowing us to quantify microsaccadic eye movement and nystagmus parameters accurately.

REPORTABLE OUTCOMES

Year 1

- Presentation of research project to Congressional Briefing in Washington D.C. Feb 2011
- Presentation and discussion of TBI related research planned to Smith Kettlewell symposium on TBI March 2011
- Received DOD TATRC 3-year grant on investigation of photosensitivity in TBI
- Since the first year of this research was restricted to implementation of a hardware and software testing and analysis platform, we have not tested human subjects. Therefore, we did not yet have results of testing to report in the literature. However, the following two manuscripts were published on relevant work to this project:
    - Kardon R, Anderson SC, Damarjian TG, Grace EM, Stone E, Kawasaki A. Chromatic pupillometry in patients with retinitis pigmentosa. Ophthalmology 2011;118(2): 376-81.
    - Park JC, Moura AL, Raza AS, Rhee DW, Kardon RH, Hood DC. Toward a clinical protocol for assessing rod, cone, and melanopsin contributions to the human pupil response. Invest Ophthalmol Vis Sci. 2011 Aug 22;52(9):6624-35.

Year 2 & 3

- IRB approval for testing human subjects took longer than expected. The process was concluded by the end of Year 2 with approval from our local IRB3 Human Use Committee and final approval by Brigit Ciccarello after second-level review and approval by ORP HRPO. By the end of Year 3 we secured a clinical testing suite in the Ophthalmology Department at the University of Iowa. Therefore, we did not have results of testing to report in the literature. However, the following two manuscripts were published on relevant work to this project:
    - Kawasaki A, Crippa SV, Kardon R, Leon L, Hamel C. Characterization of Pupil Responses to Blue and Red Light Stimuli in Autosomal Dominant Retinitis Pigmentosa due to NR2E3 Mutation. Invest Ophthalmol Vis Sci. 2012 Aug 15;53(9):5562-9.
    - Kawasaki A, Munier FL, Leon L, Kardon RH. Pupillometric quantification of residual rod and cone activity in leber congenital amaurosis. Arch Ophthalmol. 2012 Jun;130(6):798-800.

Year 4

- Based on the encouraging results from the continuous RAPD testing and analysis protocol developed as part of this project, we have submitted an Invention Disclosure to the University of Iowa Research Foundation, titled "Objective Methods of Testing Visual Function Using the Pupil Light Reflex", with an eye on submitting a provisional patent on the concept. Such a testing system would be highly useful in objectively screening patients for disorders affecting the retina, optic nerve or the efferent nerve pathways supplying the iris muscles as well as disorders affecting the iris muscles directly. Besides ophthalmology, neurology and neurosurgery, the application would also benefit primary and emergency care where a physician or physician extender may not have the skills or knowledge to be able to assess the visual system. Another important application would be its use in home care devices that could

measure the aforementioned functions over time to understand if there is a worsening or improvement and response to treatment.

- Based on our preliminary findings that the melanopsin mediated pupil response, derived from the differential sustained pupil response to blue light vs. red light, correlates highly with retinal ganglion cell layer thickness derived from optical coherence tomography (OCT) in eyes with optic neuropathy due to multiple sclerosis, we have submitted an Invention Disclosure to the University of Iowa Research Foundation, titled "Use of the Pupil Light Reflex to Chromatic Stimuli to Track Optic Neuropathy", with an eye on submitting a provisional patent on the concept. Such a testing system would make it possible to use each eye as its own control, and minimizes the impact of central nervous system influences on measurements of visual function and pupil response that are unrelated to the condition affecting vision. Such central nervous system influences having to do with state of excitement or sleepiness can cause fluctuations in the response of the pupil unrelated to the eye's function and can confound the diagnosis of ocular disorders, which is a deficiency of existing approaches to use the pupil light reflex as a measure of ocular visual function independent of the other eye.
- Kardon RH, Poolman P, Pienta JN, Full JM, Anderson SC. A New Automated 20 Second Pupillographic Test to Quantify the Log Unit Relative Afferent Pupillary Defect and its Relationship to Retinal Ganglion Cell Thickness. Invest. Ophthalmol. Vis. Sci.. 2014; 55(13):3539.
- Poolman P, Pienta JN, Full JM, Anderson SC, Kardon RH. The Influence of Eyelid Position and the Photic Blink Reflex Upon the Pupil Light Reflex. Invest. Ophthalmol. Vis. Sci.. 2014; 55(13):4098.

Year 5

- Based on our invention disclosures to the University of Iowa Research Foundation, we submitted a provisional patent application titled "Systems and Methods For Recording, Tracking, and Interpreting Facial Features", with an eye on submitting a non-provisional patent on the concept within the allowed period of a year.
- Drs. Kardon and Poolman founded MedFace as a start-up business at the end of 2014 to bring to market objective diagnostic metrics of ocular and neurological functions, relating them to corresponding facial features (pupil movements, eye movements, eyelid movements and facial muscle movements), in order to characterize disorders of vision and associated central nervous (CNS) system disorders and monitor their change over time. MedFace was awarded first place for "The Most Promising New Business" by the 2014 University of Iowa Venture School through the John Pappajohn Entrepreneurial Center. At the conclusion of the Venture School program, several high profile investors and pharmaceutical companies indicated their interest in investing in MedFace's business proposition of utilizing mobile devices to perform at-home diagnosis and treatment monitoring of vision-related diseases and neurological disorders, such as papilledema, glaucoma, age-related macular degeneration, diabetic retinopathy and neuropathy, as well as photosensitivity and its role in diagnosing and monitoring treatment of debilitating CNS disorders such as migraine, acute and chronic pain, and Parkinson's disease.
- Poolman P, Anderson SC, Grimm J, Full JM, Thurtell M, Wall M, Kardon RH. A New Pupil Light Reflex Test for Detecting Optic Neuropathy Independent of the Fellow Eye Which Highly

Correlates to Visual Field Volume. Association for Research in Vision and Ophthalmology (ARVO); 2015.

- Kardon RH, Anderson S, Grimm J, Thurtell M, Wall M, Poolman P. A New Pupil Light Reflex Test Detects Optic Neuropathy Independent of the Fellow Eye and Correlates with Visual Field Volume. 41st Annual North American Neuro-Ophthalmology Society (NANOS) Meeting; 2015; San Diego, CA.
- Mallery RM, Thurtell MJ, Poolman P, Full JM, Ledolter J, Rivera EJ, Kardon RH. How is Eye Fixation Affected by Optic Neuropathy? Diagnostic Value of Precise Recording of Retina Movement During an OCT Scan. 41st Annual North American Neuro-Ophthalmology Society (NANOS) Meeting; 2015; San Diego, CA.
- The Pattern of Visual Fixation Eccentricity and Instability in Optic Neuropathy and Its Spatial Relationship to Retinal Ganglion Cell Layer Thickness. Robert M. Mallery, MD, Pieter Poolman, PhD, Matthew J. Thurtell, MBBS, MSc, Jui-Kai Wang, MS, Mona K. Garvin, Ph, Johannes Ledolter, PhD, and Randy H. Kardon, MD, PhD. Investigative Ophthalmology and Visual Sciences (under review).

CONCLUSION

The research work that we carried out has important implications for the greater public good, in addition to its military relevance. Visual impairment from traumatic brain injury can occur in military personnel exposed to direct trauma to the brain or indirectly from blast injury. Similar damage to the visual system can also occur in the civilian population from TBI resulting from motor vehicle accidents and also from head injury due to contact sports at both the school and professional level. Traumatic causes of visual damage can also be additive after repeated episodes of head injury. Patients with visual pathway damage are often unaware of the problem and their associated cognitive impairment may mask the underlying vision impairment and also prevent detection with standard tests of visual function, which require good cognitive performance and focused attention during the test. In addition, other forms of cognitive impairment in the general population such as attention deficit disorder, depression, and dementia prevent the accurate assessment of visual function. Patients with undiagnosed visual dysfunction and superimposed cognitive impairment may pose a danger to themselves and to others when tasks such as driving and other tasks, which demand good visual performance, cannot be safely carried out.

For this research, our main goal was to use objective reflexes of the visual system to diagnose vision deficits and ensure effective monitoring of their treatment, when indicated. Such tests will allow accurate testing of the visual system with almost no demands on cognitive function during testing. This will be possible because the constriction of the pupils in response to light, the electrical recording of light evoked potentials (voltage) from the skin overlying the vision centers of the brain and the monitoring of purposeful eye movements to track moving targets are all objective, natural reflexes of the visual system. During the project, we took advantage of these reflexes by implementing an integrated system to quantify them using a specially designed suite of rapidly performed tests requiring little patient cooperation. These tests can now be further validated and used in cognitively intact or cognitively impaired individuals to assess visual function, leading to rehabilitation and treatment when appropriate.

The availability of the objective tests of vision will greatly improve eye care by providing faster, lower cost testing that can be performed in remote settings. This will provide easier access of the public to accurate assessment of their visual function and will also reduce the cost associated with current testing and transportation to sites of testing. Such tests will also provide a new tool for assessing innovative treatments being developed to save or restore vision.

FUTURE DIRECTIONS

Our next direction is to start implementing the optimized testing paradigm into more portable devices and platforms that could have a large presence in remote testing environments, including battlefield testing, triaging medical units and referral medical centers. This approach will also provide a means of monitoring conditions that affect vision within a patient over time and can be used to objectively monitor treatments. In addition, a portable platform will allow testing of a much larger number of subjects, which will create a large database of normal responses and abnormal responses due to different disorders. This "Big Data" approach will be conducive to testing outcomes and linking phenotypic responses of the visual system to risk factors and genetic determinants. We are poised to go forward with this ambitious initiative with the continued support of the DOD, NIH and VA for this important and timely research.

REFERENCES

Boyle DP, Gupta HV, Sorooshian S. Toward improved calibration of hydrologic models: Combining the strengths of manual and automatic methods. Water Resources Res. 2000;36(12):3663–3674.

Gupta HV, Sorooshian S, Yapo PO. Status of automatic calibration for hydrologic models: Comparison with multilevel expert calibration. J. Hydrologic Eng. 1999;4(2):135–143.

Hood DC, Bach M, Brigell M, Keating D, Kondo M, Lyons JS, Marmor MF, McCulloch DL, Palmowski-Wolfe AM. ISCEV standard for clinical multifocal electroretinography (mfERG) (2011 edition). Doc Ophthalmol. 2012 Feb;124(1):1–13.

Kalaboukhova L, Fridhammar V, Lindblom B. Relative afferent pupillary defect in glaucoma: a pupillometric study. Acta Ophthalmol Scand. 2007;85(5):519–25.

Kapoula Z, Yang Q, Otero-Millan J, Xiao S, Macknik SL, Lang A, Verny M, Martinez-Conde S. Distinctive features of microsaccades in Alzheimer's disease and in mild cognitive impairment. Age (Dordr). 2014;36(2):535–43.

Kardon R, Anderson SC, Damarjian TG, Grace EM, Stone E, Kawasaki A. Chromatic pupillometry in patients with retinitis pigmentosa. Ophthalmology. 2011;118(2):376–81.

Kawasaki A, Kardon RH. Intrinsically photosensitive retinal ganglion cells. J Neuroophthalmol. 2007;27(3):195–204.

Moriasi DN, Arnold JG, Van Liew MW, Binger RL, Harmel RD, Veith TL. Model evaluation guidelines for systematic quantification of accuracy in watershed simulations. Transactions of the ASABE. 2007;50(3):885–900.

Nash JE, Sutcliffe JV. River flow forecasting through conceptual models part I — A discussion of principles. Journal of Hydrology. 1970;10(3):282–290.

Odom JV, Bach M, Brigell M, Holder GE, McCulloch DL, Tormene AP, Vaegan. ISCEV standard for clinical visual evoked potentials (2009 update). Doc Ophthalmol. 2010;120(1):111–9.

Park JC, Moura AL, Raza AS, Rhee DW, Kardon RH, Hood DC. Toward a clinical protocol for assessing rod, cone, and melanopsin contributions to the human pupil response. Invest Ophthalmol Vis Sci. 2011;52(9):6624–35.

Schindler EI, Nylen EL, Ko AC, Affatigato LM, Heggen AC, Wang K, Sheffield VC, Stone EM. Deducing the pathogenic contribution of recessive ABCA4 alleles in an outbred population. Hum Mol Genet. 2010;19(19):3693–701.

Singh J, Knapp HV, Demissie M. Hydrologic modeling of the Iroquois River watershed using HSPF and SWAT. ISWS CR 2004-08. Champaign, Ill.: Illinois State Water Survey. 2004.

APPENDIX

The Pattern of Visual Fixation Eccentricity and Instability in Optic Neuropathy and Its Spatial Relationship to Retinal Ganglion Cell Layer Thickness

Robert M. Mallery, MD[1-3], Pieter Poolman, PhD[4], Matthew J. Thurtell, MBBS, MSc[3,4], Jui-Kai Wang, MS[4,5], Mona K. Garvin, PhD[4,5], Johannes Ledolter, PhD[4], and Randy H. Kardon, MD, PhD[3,4].

1. Department of Neurology, Brigham and Women's Hospital, Boston, MA
2 Department of Ophthalmology, Massachusetts Eye and Ear Infirmary, Boston, MA
3 Department of Ophthalmology and Visual Sciences, University of Iowa Hospitals and Clinics, Iowa City, IA
4 Iowa City VA Center for Prevention and Treatment of Visual Loss
5 Departments of Electrical and Computer Engineering, University of Iowa, Iowa City, IA

Word Count: 3,304

Grant Information:

C9251-C, Rehabilitation Research & Development (RR&D), VA-ORD; Iowa City VA Center for the Prevention and Treatment of Visual Loss

W81XWH-10-1-0736, DOD; Objective Methods to Test Visual Dysfunction in the Presence of Cognitive Impairment

Viragh Foundation through the collaboration with Elliot Frohman, MD, PhD, and Teresa Frohman, PA, Department of Neurology and Neurotherapeutics, University of Texas Southwestern Medical Center

Structured Abstract:

Purpose: To assess whether clinically useful measures of fixation instability and eccentricity can be derived from retinal tracking data obtained during optical coherence tomography (OCT) in patients with optic neuropathy (ON) and develop a method for relating fixation to the retinal ganglion cell layer (GCL) thickness.

Methods: 29 patients with ON underwent macular volume OCT with 30 seconds of confocal scanning laser ophthalmoscope (cSLO)-based eye tracking during fixation. Kernel density estimation (KDE) quantified fixation instability and fixation eccentricity from the distribution of fixation points on the retina. Preferred ganglion cell layer loci (PGCL) and their relationship to the GCC thickness map were derived, accounting for radial displacement of retinal ganglion cell (RGC) soma from their corresponding cones.

Results: Fixation instability was increased in ON eyes (0.21 deg^2) compared with normal eyes (0.069 deg^2, $p<0.001$), and fixation eccentricity was increased in ON eyes (0.48 deg) compared with normal eyes (0.24 deg, $p=0.03$). Increased fixation instability and eccentricity were each highly predictive of central visual field loss. 26/35 ON eyes had PGCL skewed toward local maxima of the GCC thickness map. Patients with bilateral dense central scotomas had PGCL in homonymous retinal locations with respect to the fovea.

Conclusions: Fixation instability and eccentricity measures obtained during cSLO-OCT assess the function of perifoveal retinal elements and predict central visual field loss in patients with ON. A model relating fixation to the GCC thickness map offers a method to assess the structure-function relationship between fixation and areas of preserved GCL in patients with ON.

Introduction

Eye movements occurring during a target fixation task function to stabilize images on the retina and are a major target for rehabilitation strategies for visual loss due to macular scotomas. Abnormalities of fixation are well described in patients with macular scotomas due to retinal disease and geographic atrophy, for which the precise retinal loci of fixation can be related to the region of geographic atrophy using confocal scanning laser ophthalmoscope (cSLO) based technology. When macular disease affects the fovea, patients frequently adopt an alternate preferred retinal locus (PRL) of fixation eccentric to the fovea.[1–3] The PRL and the stability of fixation influence visual acuity obtained and performance on visually demanding tasks such as reading.[4,5] Improvement in visual acuity has been shown to mirror improvement in fixation stability in patients with age-related macular degeneration (AMD) treated with intravitreal anti-vascular endothelial growth factor (VEGF) therapy,[6] and rehabilitative strategies of modify fixation and improve reading speed have been proposed as a major form of therapy in patients with low vision.

Less in known about how fixation is altered by optic neuropathies that involve central vision. Fixation abnormalities in patients with optic neuropathy are becoming increasingly recognized, and similar diagnostic and rehabilitative strategies may be applicable for patients with central vision loss related to optic neuropathy.[7–10] In optic neuropathy, the spatial pattern of neuron loss across the macula may influence the PRL, but a method to compare fixation loci with the thickness of the inner retina layers has been lacking. In contrast to macular degeneration, cSLO images of the retina may

appear normal in optic neuropathy. Spatial correlation of the distribution of fixation loci on the retina with the corresponding retinal ganglion cell layer thickness may provide new insights into the fixation pattern of a patient with optic neuropathy.

cSLO-optical coherence tomography (cSLO-OCT) offers a promising means for assessing fixation abnormalities in patients with optic neuropathy. For example, during a Spectralis OCT examination (Heidelberg Engineering, Heidelberg, Germany), a patient is asked to fixate on a target while a cSLO tracks retinal position during the acquisition of the OCT scan. By saving the retina position during eye tracking, high-resolution fixation data can be made accessible from the device. Following segmentation of the OCT volume scans, the fixation data from the cSLO can be related to the structural integrity of individual retinal layers. Here we introduce a method that utilizes the eye tracking coordinates recorded during OCT acquisition to localize fixation points on the retina, derive measures of fixation, and relate fixation to the thickness of the ganglion cell complex (GCC), which is a combination of the ganglion cell layer (GCL) and inner plexiform layer (IPL). We assessed whether measures of fixation can identify eyes with optic neuropathy and central scotomas and characterized the topographical relationship between the fixation pattern on the retina and the GCL in eyes with unilateral and bilateral optic neuropathy.

Methods

Subjects:

Twenty-nine patients with optic neuropathy (20 unilateral and 9 bilateral) were recruited prospectively from the neuro-ophthalmology clinic at the University of Iowa Department of Ophthalmology and Visual Sciences. After exclusion of eyes with concurrent retinal abnormalities, the two study groups consisted of 35 eyes with optic neuropathy and 19 unaffected eyes. Mean subject age was 51 years, and etiologies of optic neuropathy varied among patients, including non-arteritic ischemic optic neuropathy (NAION)(n=7), arteritic ION (n=3), non-arteritic posterior ION (n=2), compressive optic neuropathy (n=7), demyelinating optic neuritis (n=6), Leber hereditary optic neuropathy (n=2), optic disc drusen (n=1), and optic nerve hypoplasia (n=1). Of the patients with optic neuritis, 3 (2 with central scotomata) were evaluated within 6 weeks of developing vision loss, and 3 (2 with persistent central scotomata) were evaluated after more than 1 year. EDTRS visual acuity and perimetry were performed on all patients. Visual fields were assessed using either Goldmann kinetic perimetry (26 patients) or automated perimetry (3 patients) with a Humphrey Field Analyzer II (Carl Zeiss Meditec, Inc., Jena, Germany) and 24-2 SITA Standard algorithm.

The research adhered to the tenets of the Declaration of Helsinki, and the research was approved by the institutional review board (IRB) at the University of Iowa. Written, informed consent was obtained from the subjects after explanation of the nature and possible consequences of the study.

Optical Coherence Tomography with Retinal Tracking:

Each patient underwent a macular volume cSLO-OCT using the Spectralis platform (Heidelberg Engineering, Heidelberg, Germany). Each macular volume scan consisted of 49 vertically-oriented B-scans spanning a 20 x 20 degree area. The SLO images and OCT B-scans were obtained at the high-resolution (HR) setting; the SLO resolution measured 1536 x 1536 pixels, and each B-scan measured 1024 x 496 pixels and consisted of a mean of 9 individual B-scans registered by Heidelberg's Automatic Real-time Tracking (ART) system.

A program installed by Heidelberg Engineering logged the retinal position acquired during eye tracking at a frequency of 4.8 Hz, the frame rate for HR video on the Spectralis. This frame rate is based on the line scan speed of the SLO (8000 lines/second) and the time-equivalent required to reset the scanning laser for the next frame (125 lines). Each row of the tracking log contained values representing an affine transformation of the reference SLO image of the OCT to the active SLO video frame, providing horizontal, vertical, and rotational values for eye position recording at the 4.8 Hz frame rate. With the contralateral eye occluded, each patient was instructed to fixate on the central internal blue fixation target while eye tracking was logged for 30 seconds before acquisition of the OCT B-scans.

Localization of the Fovea and Retinal Fixation Points

Three-dimensional (3-D) segmentation (Iowa Reference Algorithm) was applied to each macular volume scan to segment 10 retinal layers. The Iowa Reference Algorithm (http://www.biomed-imaging.uiowa.edu/downloads), is a fully three-dimensional, automated algorithm,[11–14] which can accurately measure the macular GCL-IPL complex in the presence of optic disc edema. The incorporation of three-dimensional information allows the Iowa reference algorithm to decrease segmentation error.[11–13] The boundaries of the macular GCL-IPL were defined by the junction between the retinal nerve fiber and ganglion cell layers and the junction between the inner plexiform and inner nuclear layers. The automated segmented layers were inspected for errors and manually corrected if present. The position of the fovea in the SLO reference image was identified as the thinnest portion of the retina between the internal limiting membrane and basement membrane (ILM-BM) within the foveola zone and manually corrected if necessary using the vertical B-scans and horizontal B-scan reconstructions (Figure 1, A-C). The initial point of fixation on the retina was the center of the reference image, which corresponds to both the optical center of the SLO and the location of the center fixation LED of the Spectralis. The full set of fixation points on the retina was derived by applying the affine transformation of the tracking log to the location of the initial fixation point (Figure 1, D).

Calculation of Fixation Stability, Preferred Retinal Loci, and Eccentricity

Kernel density estimation (KDE), a non-parametric method, was used to calculate the probability of fixating at each point on the retina with respect to the fovea. By a previously described method,[15] fixation stability for each eye was calculated as the area of the 68% isoline of the KDE (Figure 1, E). PRL were defined as the centroid of distinct retinal areas enclosed by a component of the 68% isoline and containing at least 10% of the total number for fixation points. Fixation eccentricity was defined as the weighted displacement of all PRL from the fovea (Figure 2).

Statistical Analysis

Statistical analysis was performed using STATA Version 14 (College Station, TX, USA). Statistical significance was assumed at $p < 0.05$. Wilcoxan rank sum tests were used to compare median fixation stability and eccentricity for all eyes with optic neuropathy compared with all control eyes. In patients with unilateral optic neuropathy, Wilcoxan signed-rank tests were used to compare fixation stability and eccentricity in affected eyes with their corresponding unaffected eye. 95% confidence intervals (CI) for median values were calculated using a binomial method. ROC analysis determined optimal threshold values for detecting optic neuropathy and central visual field defects (central scotomas), based upon fixation stability and fixation eccentricity. Central visual loss was defined as the inability to detect the I2e stimulus within the central 5 degrees on Goldmann perimetry or a reduction in central sensitivity in the four center-most stimulus locations on Humphrey automated perimetry by more than 5 dB. Optimal

threshold values maximized the sum of sensitivity and specificity for each ROC analysis.

Correlation of Fixation with Retinal Ganglion Cell Layer Thickness

3-D Automated segmentation of the GCC (GCL + IPL) was reviewed for accuracy, and manual correction of the GCL+IPL segmentation was performed if necessary. GCL+IPL thickness maps with voxel size 21 x 21 pixels (0.41x 0.41 degrees) were created from the segmented data and centered on the fovea. The voxel size represented the smallest possible square voxel size without interpolation and was derived from 49 B-scans, which cover 20 degrees (20 degrees / 49 = 0.41 degrees).

In order to determine whether a structural-functional relationships exists between fixation and areas of intact GCL, the coordinates of the fixation points on the retina (corresponding to photoreceptors) were transformed to the coordinates of RGC soma within the GCC thickness map by implementing a two dimensional model to account for displacement of RGC soma from their corresponding photoreceptor inner segments (Figure 3).[16] KDE was applied to the locations of these RGC soma to identify preferred loci overlying the GCC thickness map that correlate with the subject's fixation. We termed this area of the GCC thickness map the preferred ganglion cell locus (PGCL).

The PGCL was compared with the GCC thickness map for all eyes with optic neuropathy and all normal eyes. For unilateral ON eyes where fixation corresponded poorly with remaining GCC thickness, fixation was also compared with the fellow normal

eye, and in patients with bilateral optic neuropathy, fixation was compared to the contralateral affected eye, too.

Computational Methods

Computational analysis including image processing, calculation of fixation stability and eccentricity measures, and modeling of ganglion cell displacement from the cone inner segments was performed using custom written code in MATLAB Version 8.5 (MathWorks, Inc., Natick, MA).

Results

Fixation instability (area of the 68% isoline of the KDE) was increased in ON eyes (0.21 deg^2, CI: 0.12-0.32 deg^2) compared with normal eyes (0.069 deg^2, CI: 0.030-0.090 deg^2, $p<0.001$) as shown in Figure 4, A. A paired comparison of the affected eyes with normal eyes of patients with unilateral optic neuropathy also showed a significant increase in fixation instability in the ON eyes (0.17 deg^2, CI: 0.092-0.37 deg^2) compared with normal eyes (0.063 deg^2, CI 0.029-0.081 deg^2, $p = 0.001$) as shown in Figure 4, B. Similarly, fixation eccentricity was increased in ON eyes (0.48 deg, CI: 0.25-0.88 deg) compared with controls (0.24 deg, CI: 0.17-0.33 deg, $p=0.03$) as shown in Figure 4, C, and a paired comparison of affected and normal eyes in patients with

unilateral optic neuropathy confirmed an increase in the amount of eccentric fixation in ON eyes (0.58 deg, CI: 0.23-0.88 deg) compared with normal eyes (0.24 deg, CI: 0.17-0.34 deg, $p = 0.006$) as shown in Figure 4, D.

Fixation instability and fixation eccentricity were each compared with logMAR using a scatter plot (Figure 5). For any given logMAR there was a wide range of values seen for fixation instability or fixation eccentricity, but larger values of fixation stability or fixation eccentricity were highly suggestive of the presence of optic neuropathy and central visual field loss.

Receiver operating characteristic (ROC) analysis determined the utility of abnormal fixation stability and eccentricity for determining whether a central scotoma was present (Figure 6, A-B). The ROC curve for predicting central visual field loss based upon fixation instability had an AUC of 0.93 (Figure 6, A), and the ROC curve for predicting central visual loss based upon fixation eccentricity had an AUC of 0.90 (Figure 6, B). A threshold value for fixation instability of greater than 0.25 deg^2 had sensitivity of 79% and specificity of 94%, and a threshold value for fixation eccentricity of greater than 0.8 degrees had a sensitivity of 74% and specificity of 100%.

The ROC curve for predicting optic neuropathy (with or without a central scotoma) based upon fixation instability had an area under the curve (AUC) of 0.80, and the ROC curve for predicting optic neuropathy based upon fixation eccentricity had an AUC of 0.68. Optimal sensitivity and specificity values for predicting the presence of optic neuropathy were calculated for each measure of fixation, giving a sensitivity of 83% and specificity of 68% for fixation instability worse than 0.08 deg^2, and a sensitivity of 57% and specificity of 89% for fixation eccentricity greater than 0.40 degrees.

Twelve of 18 eyes with unilateral optic neuropathy had PGCL that were spatially skewed toward the more intact (thicker) areas of the GCC thickness map (Figure 7, row A). In patients with bilateral optic neuropathy (16 eyes), all but 2 eyes had PGCL that were skewed toward the local maxima of GCC thickness (Figure 7, row B). In patients with bilateral, central scotomas with moderate-severely reduced acuities, the PGCL were located in symmetric (homonymous) regions of the GCC with respect to the fovea (Figure 7, row C). In 4 of 6 eyes where PGCL corresponded unexpectedly to local minima of the GCC map, the position of the PGCL relative to the fovea was similar to that of the contralateral unaffected eye (Figure 7, row D). In total, 26 of 35 eyes with optic neuropathy had a pattern of fixation on the retina that correlated spatially with the intact region of the ganglion cell thickness map.

Discussion:

The manner by which patients with central visual loss fixate is fundamental to interpreting clinical tests of visual function and represents an important measure for understanding how patients adapt to visual loss. In patients with retinal disease or optic neuropathy, improvement in visual function measurements are likely due to functional recovery of injured elements of the retina or optic nerve or changes in the receptive field properties of recipient neurons in visual cortex, resulting in adaptive changes in fixation. Disentangling the effects of these distinct processes to better understand the

contribution of each is critical for assessing the efficacy of targeted therapies for retinal disease and optic neuropathies.

We implemented a method to take advantage of the cSLO-based retinal tracking capabilities of newer generation OCT devices to assess fixation abnormalities and derive the pattern of fixation relative to the GCC in patients with optic neuropathies. We found that fixation preferences, as quantified by fixation stability and eccentricity measures, were altered in patients with optic neuropathy. Eyes with optic neuropathy had a 2-3-fold increase in fixation instability and a greater than 2-fold increase in fixation eccentricity compared with normal eyes. As suggested by ROC analysis, fixation stability and eccentricity measures were only moderately predictive of the presence of optic neuropathy. This was most likely influenced by the fact that of the optic neuropathy eyes tested in this study, not all had central visual loss affecting fixation. However, when ROC analysis was performed comparing eyes with central scotoma vs. without central scotoma, fixation stability and eccentricity were highly predictive of the presence of central visual field loss (Figure 6). A large proportion of the affected eyes (16/35), such as those with altitudinal visual field loss, had areas of preserved central visual field and only moderately affected fixation stability or eccentricity. Another interesting pattern was the presence of a “fenestration” within a central scotoma that allowed a person to centrally fixate, even though a dense scotoma was plotted using standard perimetric testing. This highlights another value of precise assessment of retinal fixation points that may contradict visual acuity measurements recorded using a standard logMAR acuity test; small seeing areas within a large, dense central scotoma may not be apparent by standard visual acuity testing, depending on the size letter that a patient is shown.

Measures of fixation are capable of interrogating the function of perifoveal retinal elements in a manner that is beyond the spatial resolution of standard perimetry, and may provide additional information not evident on visual field testing. Normal eyes fixated with a mean eccentricity of 0.26 degrees from the fovea anatomical center; the retinal area of fixation did not always co-localize with the nadir of the foveal pit and was often located over the slope of the foveal pit. ON eyes had a median fixation eccentricity of 0.48 degrees from the fovea anatomic center; the closest stimuli to the fixation target in standard clinical automated perimetry is 3 degrees using a 24-2 test strategy and 1 degree using a 10-2 test strategy and therefore, do not provide the spatial resolution needed to precisely assess fixation. Also, with standard perimetry the location of fixation is not recorded at the time visual threshold is tested, leading to potential errors in the detection and localization of a small scotoma.

The work by Curcio and others to model the displacement of retinal ganglion cell soma from their corresponding cones [16–18] has provided a framework for relating measures of visual function to structural changes of the GCC in patients with optic neuropathies.[19–21] Fixation in normal patients occurs within the foveola zone (mean eccentricity from the fovea center of 0.26 degrees in the normal eyes in our study), and the first retinal ganglion cells from do not appear until 150-200 microns (approximately 0.5 degrees) lateral to the fovea center. In patients with optic neuropathy who fixate eccentrically, there can be an up to a 2 degree difference in the location of the retinal cones with respect to the corresponding RGC soma (Figure 3 A). Correction for RGC displacement is therefore critical for relating the location of fixation on the retina to local areas of the GCC.

Our analysis of fixation based upon GCC thickness provided several important observations. Fixation correlated with thicker regions of GCC thickness in a majority of ON eyes, but in some patients, correlated with a relatively thinned region. Poor correlation occurred in 6 patients with unilateral optic neuropathy, 4 of whom had PGCL that were highly similar to the PGCL of the contralateral normal eye; this may suggest that patients with unilateral optic neuropathies may utilize suboptimal fixation in the affected eye due to the influence from the unaffected, better seeing eye. Alternatively, PGCL in relatively thin areas of the GCC may suggest better visual potential than predicted by the degree of GCC thinning. Finally, the pattern of fixation is likely to be task dependent and may be influenced by whether the target is a simple object such as the one used in our study, an optotype, or even words as part of a more complex reading task.[4,5,22–25] The two patients with symmetrical bilateral visual loss and central scotomas due to LHON adopted eccentric PRGL located in similar locations in each eye (Figure 6, row C). For these patients, the GCC was diffusely thin, and the location of the PRGL may indicate focal areas of better retinal sensitivity or be influenced by optimal placement of the central scotoma to maximize visual function.

In conclusion, retina movement data collected during fixation on an internal target with a cSLO-OCT in patients with optic neuropathy provides an additional measure of visual function that is highly predictive of central visual loss, influenced primarily by the function of foveal and perifoveal retinal elements, and additive to other clinical testing. We established a framework for relating fixation points on the retina to the GCC thickness map, a tool that will allow further study of the role that fixation plays in

improvement of visual function measures after optic neuropathy. The principle of correlating of fixation measured by cSLO-OCT with individual retinal layers is generalizable to patients with other diseases affecting the retina.

Acknowledgments:

The authors thank Jan M. Full, RN, for her technical expertise in acquiring OCT data.

References:

1. Fletcher DC, Schuchard RA. Preferred retinal loci relationship to macular scotomas in a low-vision population. *Ophthalmology*. 1997;104(4):632-638.

2. Reinhard J, Messias A, Dietz K, et al. Quantifying fixation in patients with Stargardt disease. *Vision Res*. 2007;47(15):2076-2085.

3. Kumar G, Chung STL. Characteristics of fixational eye movements in people with macular disease. *Invest Ophthalmol Vis Sci*. 2014;55(8):5125-5133.

4. Sunness JS, Applegate CA, Haselwood D, Rubin GS. Fixation patterns and reading rates in eyes with central scotomas from advanced atrophic age-related macular degeneration and Stargardt disease. *Ophthalmology*. 1996;103(9):1458-1466.

5. Sunness JS, Applegate CA. Long-term follow-up of fixation patterns in eyes with central scotomas from geographic atrophy that is associated with age-related macular degeneration. *Am J Ophthalmol*. 2005;140(6):1085-1093.

6. González EG, Tarita-Nistor L, Mandelcorn ED, Mandelcorn M, Steinbach MJ. Fixation control before and after treatment for neovascular age-related macular degeneration. *Invest Ophthalmol Vis Sci*. 2011;52(7):4208-4213.

7. Altpeter EK, Blanke BR, Leo-Kottler B, Nguyen XN, Trauzettel-Klosinski S. Evaluation of fixation pattern and reading ability in patients with Leber hereditary optic neuropathy. *J Neuroophthalmol*. 2013;33(4):344-348.

8. Burton R, Smith ND, Crabb DP. Eye movements and reading in glaucoma: observations on patients with advanced visual field loss. *Graefes Arch Clin Exp*

Ophthalmol. 2014;252(10):1621-1630.

9. Hadavi S, Markowitz SN, Reyes SV. Leber's neuropathy and preferred retinal loci. *Can J Ophthalmol*. 2013;48(1):e8-e9.

10. Smith ND, Glen FC, Crabb DP. Eye movements during visual search in patients with glaucoma. *BMC Ophthalmol*. 2012;12:45.

11. Lee K, Niemeijer M, Garvin MK, Kwon YH, Sonka M, Abramoff MD. Segmentation of the optic disc in 3-D OCT scans of the optic nerve head. *IEEE Trans Med Imaging*. 2010;29(1):159-168.

12. Garvin MK, Abramoff MD, Kardon R, Russell SR, Wu X, Sonka M. Intraretinal layer segmentation of macular optical coherence tomography images using optimal 3-D graph search. *IEEE Trans Med Imaging*. 2008;27(10):1495-1505.

13. Garvin MK, Abràmoff MD, Wu X, Russell SR, Burns TL, Sonka M. Automated 3-D intraretinal layer segmentation of macular spectral-domain optical coherence tomography images. *IEEE Trans Med Imaging*. 2009;28(9):1436-1447.

14. Wang J-K, Kardon RH, Kupersmith MJ, Garvin MK. Automated Quantification of Volumetric Optic Disc Swelling in Papilledema Using Spectral-Domain Optical Coherence Tomography Volumetric Quantification of Optic Disc Swelling. *Invest Ophthalmol Vis Sci*. 2012;53(7):4069-4075.

15. Crossland MD, Sims M, Galbraith RF, Rubin GS. Evaluation of a new quantitative technique to assess the number and extent of preferred retinal loci in macular disease. *Vision Res*. 2004;44(13):1537-1546.

16. Watson AB. A formula for human retinal ganglion cell receptive field density as a function of visual field location. *J Vis*. 2014;14(7). doi:10.1167/14.7.15.

17. Curcio CA, Allen KA. Topography of Ganglion Cells in HumanRetina. *J Comp Neurol*. 1990;300:5-25.

18. Drasdo N, Millican CL, Katholi CR, Curcio CA. The length of Henle fibers in the human retina and a model of ganglion receptive field density in the visual field. *Vision Res*. 2007;47(22):2901-2911.

19. Raza AS, Cho J, de Moraes CGV, et al. Retinal ganglion cell layer thickness and local visual field sensitivity in glaucoma. *Arch Ophthalmol*. 2011;129(12):1529-1536.

20. Moura AL de A, Raza AS, Lazow MA, De Moraes CG, Hood DC. Retinal ganglion cell and inner plexiform layer thickness measurements in regions of severe visual field sensitivity loss in patients with glaucoma. *Eye* . 2012;26(9):1188-1193.

21. Raza AS, Zhang X, De Moraes CGV, et al. Improving glaucoma detection using

spatially correspondent clusters of damage and by combining standard automated perimetry and optical coherence tomography. *Invest Ophthalmol Vis Sci*. 2014;55(1):612-624.

22. Lei H, Schuchard RA. Using two preferred retinal loci for different lighting conditions in patients with central scotomas. *Invest Ophthalmol Vis Sci*. 1997;38(9):1812-1818.

23. Schuchard RA. Preferred retinal loci and macular scotoma characteristics in patients with age-related macular degeneration. *Can J Ophthalmol*. 2005;40(3):303-312.

24. Déruaz A, Whatham AR, Mermoud C, Safran AB. Reading with multiple preferred retinal loci: implications for training a more efficient reading strategy. *Vision Res*. 2002;42(27):2947-2957.

25. Thaler L, Schütz AC, Goodale MA, Gegenfurtner KR. What is the best fixation target? The effect of target shape on stability of fixational eye movements. *Vision Res*. 2013;76:31-42.

Figures:

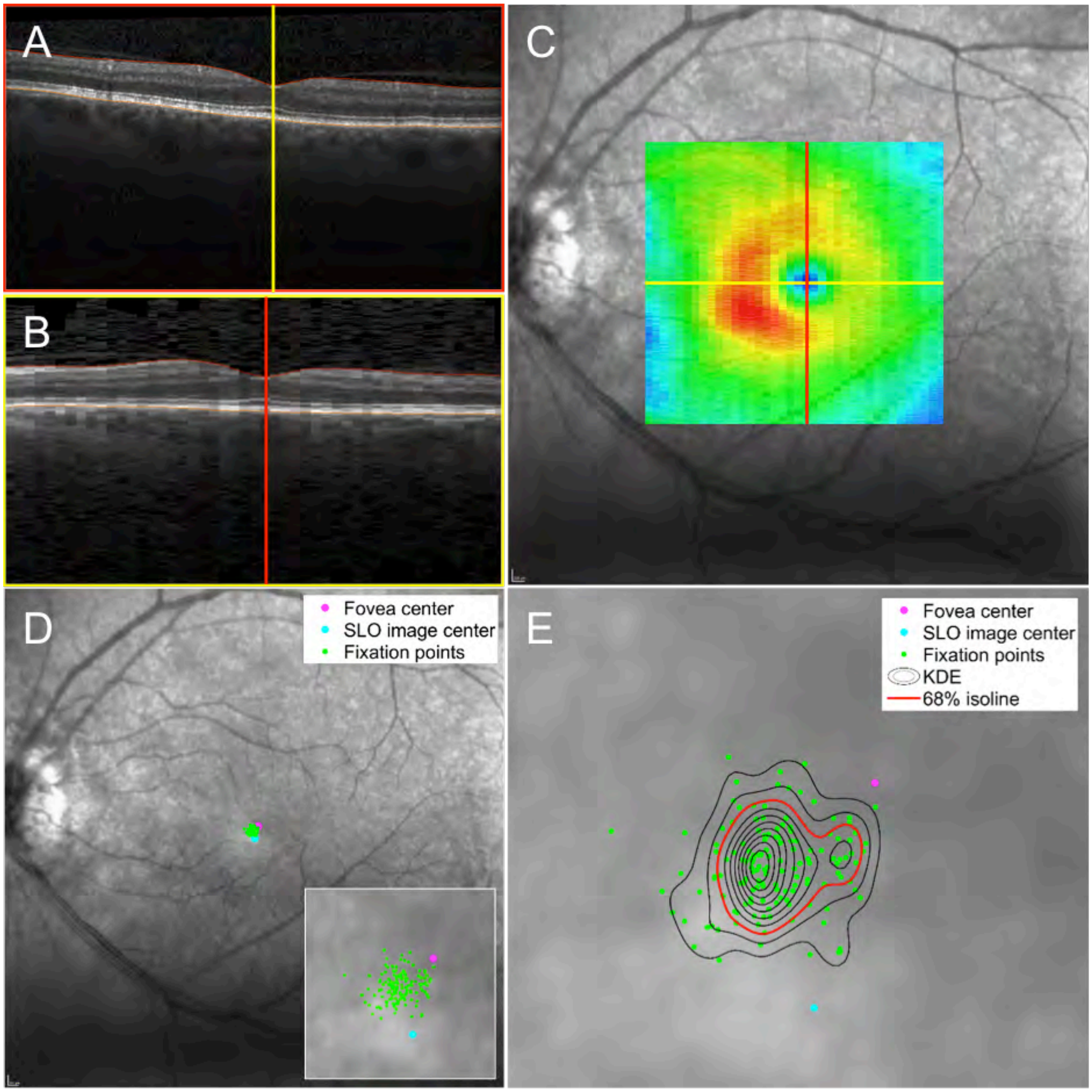

Figure 1. Localization of fixation points on the retina and the use of kernel density estimation (KDE) to calculate the preferred retinal locus (PRL) and fixation stability. A-B) Vertical OCT B-scans and horizontal B-scan reconstructions confirmed the location of the foveal center. C) The retinal thickness map (ILM-BM) is shown overlying the SLO reference image used by the Spectralis ART tracking software. The foveal center is indicated by the intersection of the vertical and horizontal lines and is depicted on the

thickness map as the central blue pixel area. D) Fixation points on the retina are calculated by applying the retinal tracking coordinates (consisting of an affine transformation of the reference image to an active SLO image during eye tracking) recorded by the Spectralis to the initial fixation point at the time the SLO reference image was acquired (SLO image center). Fixation points on the retina are shown as green dots. The anatomical foveal center is shown as the magenta dot and the SLO image center is shown by the light blue dot. A higher magnification of the macula area of fixation is shown in the inset. E) Kernel density estimation calculates the probability that fixation occurs at any given point on the retina. The 68% isoline (depicted as the red line) encloses a single area of retina, identifying that there is a single PRL. Fixation stability is calculated as the area of the 68% isoline. In this case fixation stability measures 0.13 deg^2.

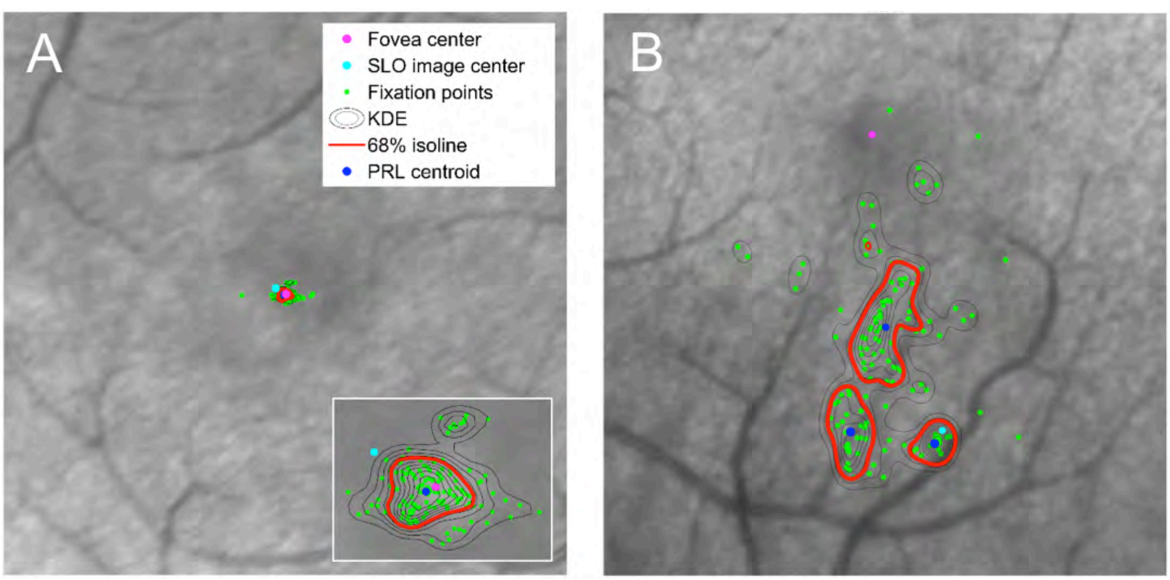

Figure 2. Comparison of fixation in a normal patient and in a patient with optic neuropathy (larger frames are shown at equal scale). A) In a normal patient, fixation

occurs within the foveola. Fixation stability, calculated as the area of the 68% isoline of the KDE, equals 0.022 deg^2. Fixation eccentricity, measured as the distance between the PRL centroid and the fovea center, equals 0.024 deg. B) A patient with LHON and a centrocecal scotoma has eccentric fixation with three distinct PRL and fixation stability measuring 1.62 deg^2. When multiple PRL are identified, a single measure of eccentricity is calculated by taking an average of the distances between the PRL centroids and the fovea center, each weighted according to the number of fixation points within the corresponding PRL. For this patient, fixation eccentricity was 3.26 deg.

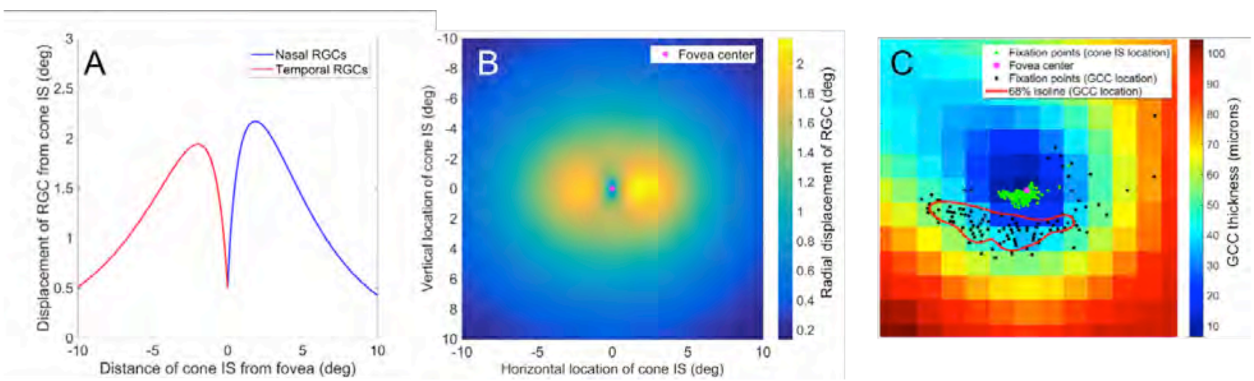

Figure 3. Correlation of retinal ganglion cell complex (GCC) thickness with fixation. A) The model by Watson et al. describes the radial displacement RGC soma from their corresponding cones.[16] The first RGCs are present 150-200 microns from the fovea center, equivalent to approximately 0.5 degrees. Within the central 5 degrees of the fovea center, there is a greater displacement of nasal RGCs compared with temporal RGCs. B) The displacement or RGC soma was generalized to the two dimensional plane assuming that vertical displacement of RGCs is approximately 75% of horizontal displacement[18]. C) Each fixation point on the retina was taken as the location of a cone, and transformed into an RGC location using the transformation map shown in B. Kernel

density estimation identified a preferred ganglion cell locus (PGCL), representing the preferred area of the GCC used for fixation. In this patient, the PGCL is skewed toward the intact GCC suggesting a strong correlation between fixation and remaining GCC.

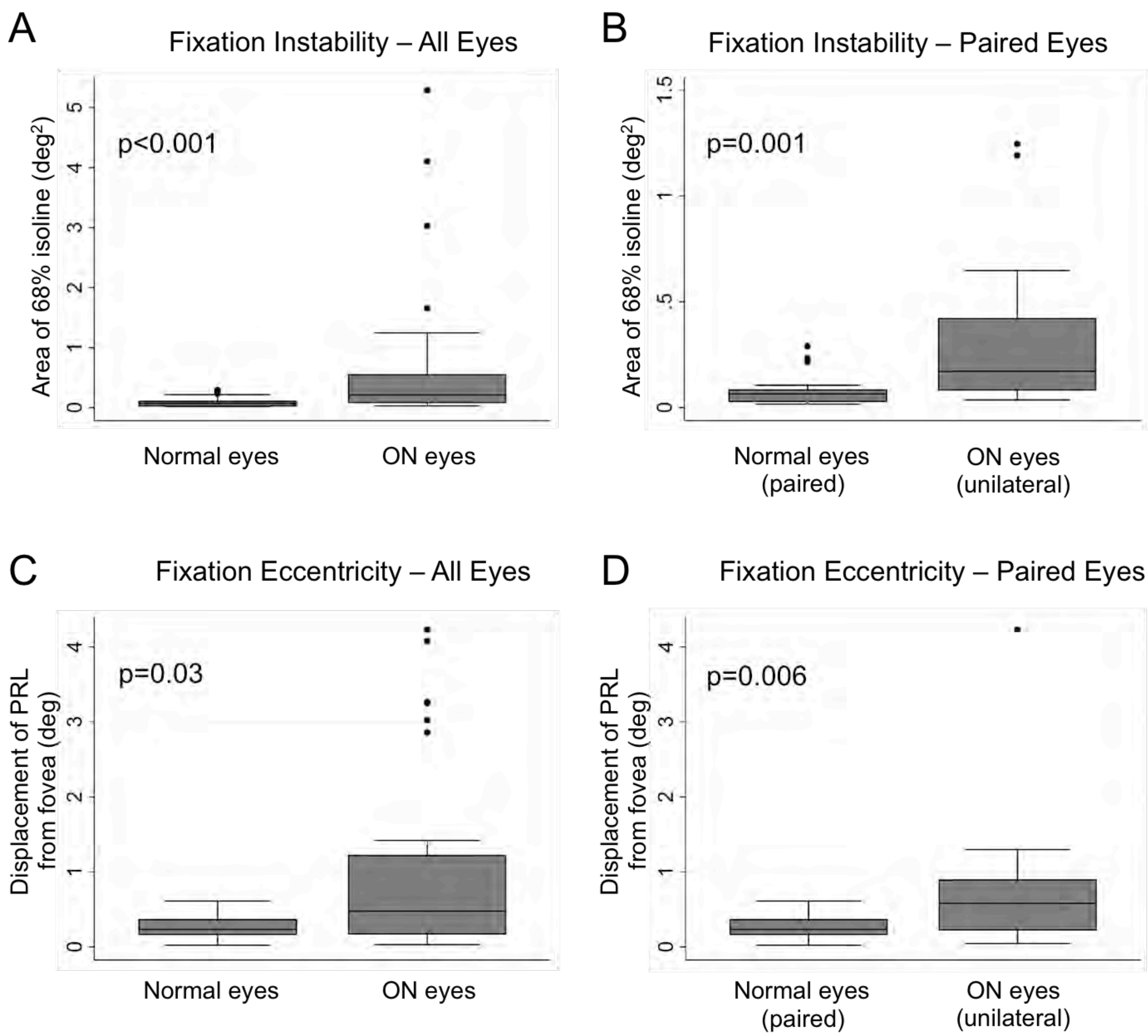

Figure 4. Fixation stability and eccentricity measures for optic neuropathy (ON) eyes and normal eyes. A) Comparison of all eyes with ON and all normal eyes shows that fixation instability is increased in ON eyes ($p<0.001$). B) A significant difference in fixation instability is still present when performing a paired comparison of affected and

unaffected eyes of patients with unilateral ON (p=0.001). C) Fixation eccentricity is increased in all ON eyes compared with all normal eyes (p=0.03), and D) a significant difference remains when affected and unaffected eyes with unilateral optic neuropathy (p=0.006).

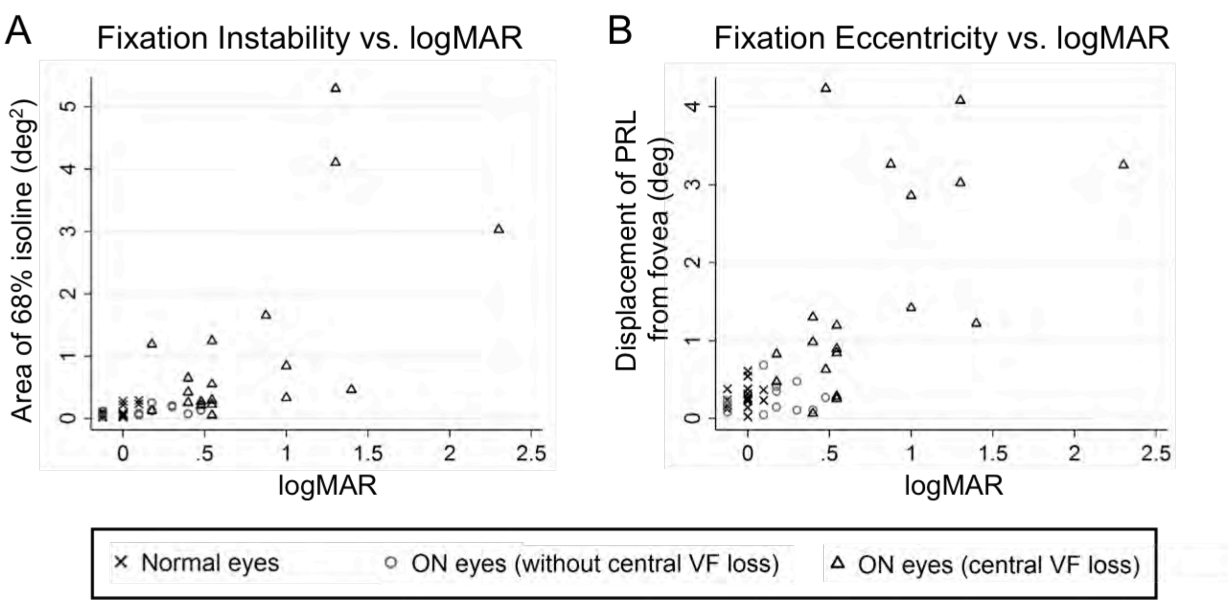

Figure 5. Scatter plot comparing fixation instability and fixation eccentricity with logMAR.

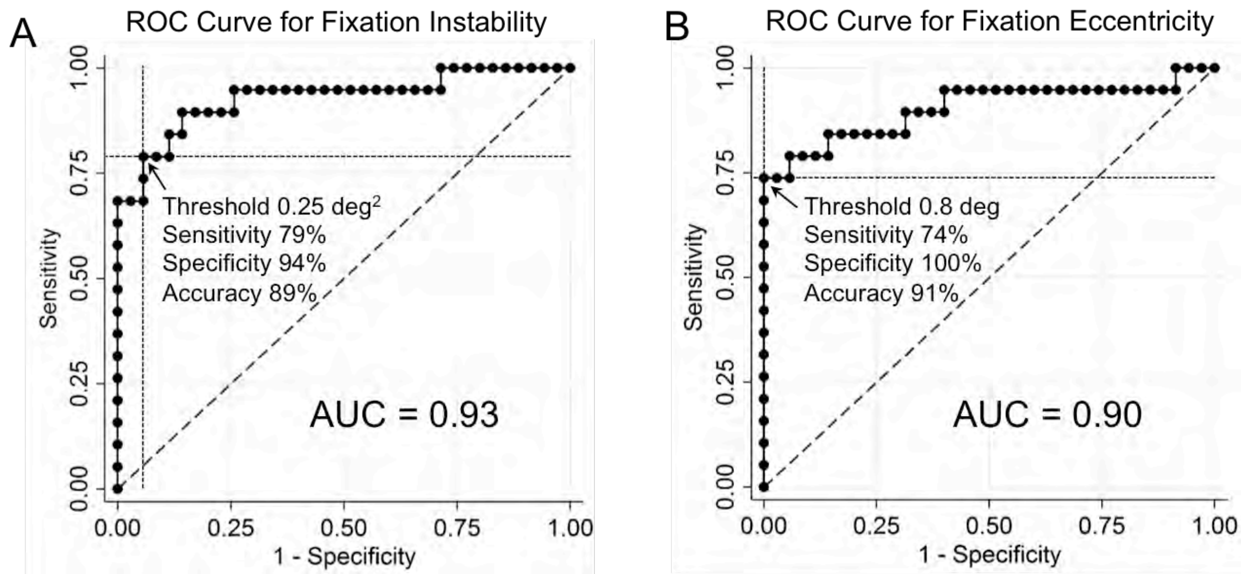

Figure 6. ROC analysis for fixation instability and eccentricity predicting the presence of a central scotoma.

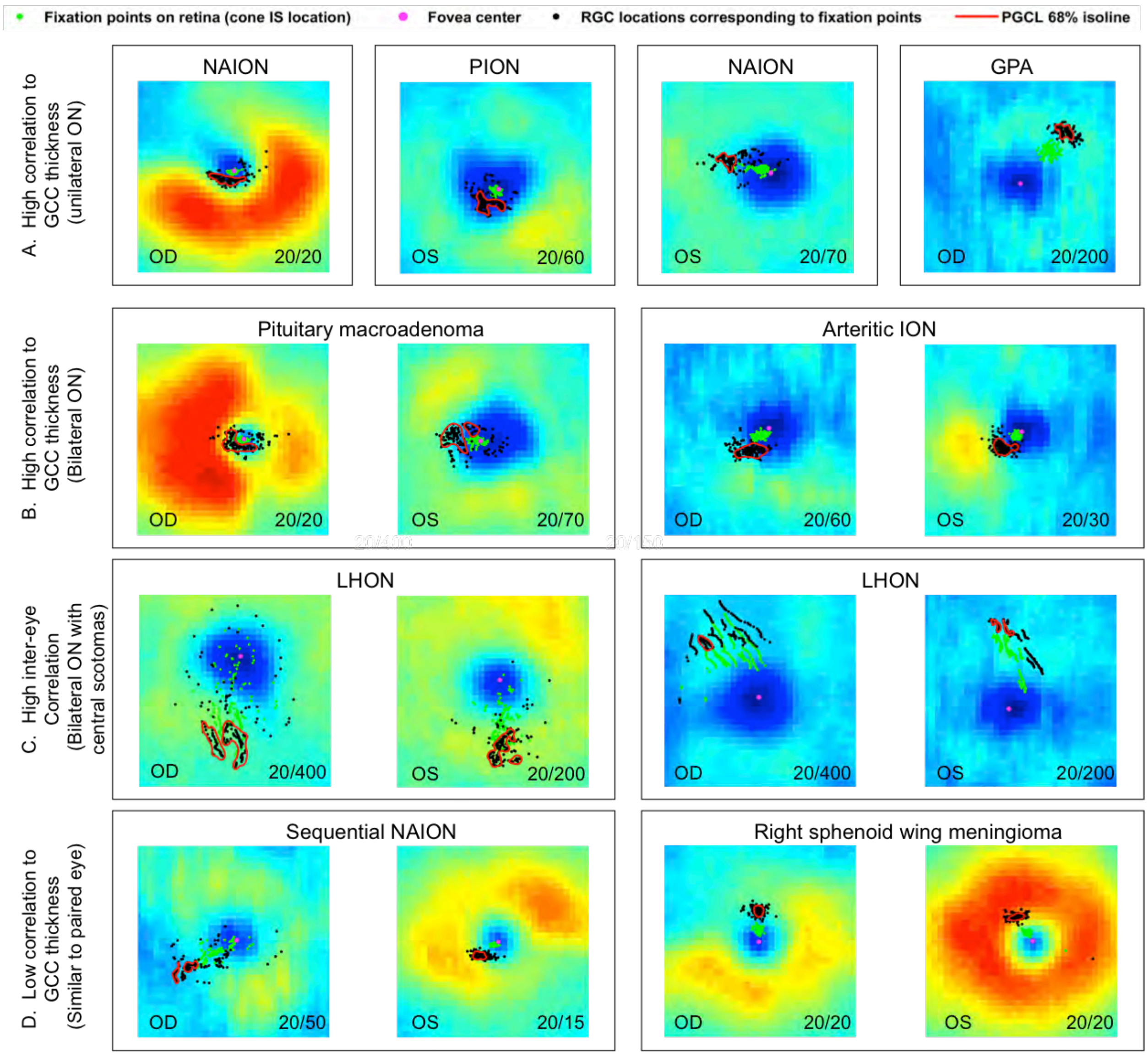

Figure 7. Examples of fixation patterns relative to the GCC thickness map. Row A) Four ON eyes with PGCL shifted favorably toward the thickest region of the GCC. Row B) Two patients with bilateral ON and PGCL that correlate highly with the more intact, thicker locations of GCC. Row C) Two patients with bilateral dense central scotomas and eccentric fixation with PGCL displaced in the same general location from the fovea in the right and left eye of the same patient. D) Two patients with fixation correlating poorly to the GCC in the eye with greater visual field and structural loss.